Aix-Marseille Université
ED352 Physique et Sciences de la Matière

Laboratoire LISA

Thèse présentée pour obtenir le grade universitaire de docteur

Mention : Instrumentation

Achouak CHALKHA

Glow discharge electron impact ionisation and improvements of linear ion trap operating mode for in-the-field detection of illegal substances

Confidential

Soutenue le 17/02/2015 devant le jury :

Steven TAYLOR	Pr., University of Liverpool (UK)	Rapporteur
Jean-Claude TABET	Pr. émérite, Université Pierre et Marie Curie	Rapporteur
Jean-François GAL	Pr. émérite, Université Nice Sophia Antipolis	Examinateur
Jacques ANDRE	Pr. émérite, Aix-Marseille Université	Examinateur
Aurika JANULYTE	MdC, Aix-Marseille Université	Co-directrice de thèse
Yves ZEREGA	Pr., Aix-Marseille Université	Directeur de thèse

Confidential

Table of Contents

Nomenclature **7**
List of Figures **11**
List of Tables **16**
Introduction **19**

Part I: Glow discharge electron impact ionisation **23**

Chapter 1: Some elements of theory about Glow Discharges **25**
1.1 Discharge . . . 25
1.2 Voltage-Current characteristics et regimes . . . 26
1.2.1 Voltage-Current characteristics . . . 26
1.2.2 Dark Discharge regime . . . 26
1.2.3 Glow Discharge regime . . . 27
1.2.4 Arc Discharge regime . . . 28
1.3 DC Glow Discharge . . . 28
1.3.1 Basic plasma process . . . 28
1.3.2 Discharge regions and potential . . . 29
1.4 DC Glow discharge in mass spectrometry . . . 31

Chapter 2: Experimental characterisation of GDES **33**
2.1 Design . . . 33
2.1.1 GDES cell . . . 33
2.1.2 GDES assembly and vacuum device . . . 33
2.2 Fluidic system . . . 35
2.2.1 Capillary mass-flow . . . 35
2.2.2 Anode orifice conductance . . . 36
2.2.3 Estimation of GDES cell pressure and volumetric-flow . . . 36
2.2.4 Choice of capillary length . . . 37
2.2.5 General throughputs . . . 39
2.3 Electric system . . . 40

Confidential

2.3.1 Power supplies and measurement devices . . . 40
2.3.2 Origin of measured currents . . . 41
2.3.3 Determination of kinetic energy . . . 42
2.4 Characterisation of glow discharge . . . 42
2.4.1 Paschen curve . . . 42
2.4.2 Voltage-Current characteristic . . . 43
2.4.3 Time-dependence of the discharge current . . . 44
2.4.4 Characterization of the deposits . . . 47
2.5 Principle to operate the discharge with stabilisation . . . 50
2.5.1 Principle . . . 50
2.5.2 Temporal evolution of V-I characteristic . . . 51
2.5.3 Temporal stabilisation of discharge current . . . 51
2.6 Characterisation of the electron beam . . . 52
2.6.1 Electron kinetic energy distribution in the discharge . . . 52
2.6.2 Electron kinetic energy distribution in the beam . . . 54
2.6.3 Electron current intensity, power consumption and emission efficiency . . . 57
2.6.4 Stability and reproducibility of measured currents . . . 57
2.7 Conclusion . . . 60

Chapter 3: GDES/EI Coupling 61
3.1 Material and method . . . 61
3.1.1 Device description . . . 61
3.1.2 Electron ionisation at 70 eV . . . 63
3.1.3 Potential applied to anode . . . 63
3.2 Simulation results . . . 65
3.2.1 Charged Particles Optics software . . . 65
3.2.2 Design and simulation conditions . . . 65
3.2.3 Influence of the potential applied to the repeller . . . 65
3.2.4 Repeller potential according to kinetic energy . . . 66
3.2.5 Distribution of electron kinetic energy in the ion cage . . . 67
3.3 Experimental results with filament . . . 73
3.3.1 Experimental device . . . 73
3.3.2 Electron current stability . . . 75
3.3.3 Potential applied to the repeller . . . 75
3.3.4 Ion focussing and transmission . . . 76
3.3.5 Sensitivity and detection low-threshold . . . 76
3.4 GDES/EI Experimental results . . . 78
3.4.1 Experimental device . . . 78
3.4.2 Electron currents and Faraday cup signal . . . 81

Confidential

3.5 Result comparisons . . . 81
3.5.1 Between filament and GDES experimental results . . . 81
3.5.2 Between GDES experimental and simulation results . . . 84
3.6 Conclusion . . . 84

Part II: Ion injection and confinement in a Linear Ion Trap 87

Chapter 4: Theoretical aspects of quadrupole fields 89
4.1 The mass filter . . . 89
4.1.1 2D quadrupole potential and mass filter design . . . 89
4.1.2 The ion motion . . . 91
4.1.3 Motion stability and stability diagram . . . 92
4.1.4 Stability diagrams in (U_0, V_0) plane and mass spectrometry analysis . . . 92
4.2 The Linear Ion Trap . . . 95
4.2.1 Introduction . . . 95
4.2.2 LIT and Mass spectrometry . . . 95
4.2.3 Potential . . . 96

Chapter 5: Operating conditions for simulation 99
5.1 Device design . . . 99
5.2 Potential configurations for the mass filter electrodes . . . 99
5.3 Single Ion Monitoring operating mode sequences . . . 102
5.4 Ion injection stage conditions . . . 103
5.5 Ion confinement stage conditions . . . 103

Chapter 6: Ion injection simulation results 105
6.1 Ion trajectories . . . 105
6.2 Temporal ion distribution . . . 105
6.3 Ion distribution in positions and velocities . . . 107
6.4 Maximal number of injected ions . . . 109
6.5 Conclusion . . . 109

Chapter 7: Simulation studies of LIT confinement 117
7.1 Evolution of the number of confined ions . . . 117
7.2 LIT stability diagram in (a_x, q_x) plane . . . 117
7.3 Axial DC potential at $r = 0$ . . . 119
7.4 Axial and radial motion frequencies . . . 120
7.5 Non-linearity influence on LIT stability diagram in (U_0, V_0) plane . . . 123
7.5.1 Maximal value . . . 124

Confidential

7.5.2 Apex value 124
7.6 Collisional cooling 127
7.7 Further studies and proposals 128
Conclusion **133**

Confidential

Nomenclature

Design

GDES

- GDES Glow Discharge Electron Source
- l_1 length of capillary (m) (between $7\text{x}10^{-2}$ to $50\text{x}10^{-2}$ m)
- d_1 internal diameter of capillary equal to $6.3\text{x}10^{-5}$ m
- d_A diameter of anode orifice equal to $3.3\text{x}10^{-4}$ m
- d_{AC} distance between anode and cathode equal to $6.6\text{x}10^{-2}$ m
- OD outside diameter
- ID inner diameter

EI/lenses/LIT

- EI Electron Ionization
- L_{De} ion decelerating lens
- L_{EI} ion extraction lens
- L_{En} entrance endcap lens
- L_{Ex} exit endcap lens
- L_{Fo} electron blocking/focussing lens
- LIT Linear Ion Trap

Confidential

Fluid

- Q_1 capillary throughput or mass-flow$(\mathrm{Pa} \times \mathrm{m}^3/\mathrm{s})$ (W)
- Q_A anode orifice throughput or mass-flow $(\mathrm{Pa} \times \mathrm{m}^3/\mathrm{s})$ (W)
- Q_T turbo-molecular pump throughput $(\mathrm{Pa} \times \mathrm{m}^3/\mathrm{s})$ (W)
- Q_L residual leak and degassing throughput $(\mathrm{Pa} \times \mathrm{m}^3/\mathrm{s})$ (W)
- C_1 conductance of capillary $(\mathrm{m}^3/\mathrm{s})$
- C_A conductance of anode orifice $(\mathrm{m}^3/\mathrm{s})$
- S_T turbo-molecular pump speed $(\mathrm{m}^3/\mathrm{s})$
- S_{ef} effective pumping speed $(\mathrm{m}^3/\mathrm{s})$
- p_a ambient pressure (Pa) or (torr)
- p_{GD} pressure in GDES cell (Pa) (torr)
- p_M pressure in vacuum chamber (Pa) (torr)

Energy and electricity

- v_A electron velocity at anode orifice (m/s)
- v_{IC} electron velocity in ion cage of EI (m/s)
- $E_{k,A}$ electron kinetic energy at anode orifice (J) $\times$ 6.24150974 $\times 10^{18}$ (eV)
- $E_{k,IC}$ electron kinetic energy in ion cage (J)
- $E_{p,A}$ electron potential energy at anode orifice (eV)
- $E_{p,IC}$ electron potential energy in ion cage (eV)
- V_A anode potential (V)
- V_C cathode potential (V)
- V_{AC} potential between anode and cathode (V)
- V_{RE} potential applied to repeller (V)
- V_{IC} potential applied to ion cage or extract lens (V)
- V_{FL} potential applied to ion focussing lens (V)

Confidential

- V_{DL} potential applied to electron blocking/focussing lens (V)
- V_{EL} potential applied to entrance end cap of LIT (V)
- V_{XL} potential applied to exit end cap of LIT (V)
- U_{GD} potential of the discharge sustaining power supply (V)
- U_{PP} potential of the collection plate polarisation power supply applied across the collection plate and anode, for testing GDES cell (V)
- U_{PA} potential of the anode polarisation supply applied across the ion cage and anode, when coupled to the EI source (V)
- U_{IC} potential of the ion cage polarisation supply (V)
- I_C current measured at cathode (A)
- I_A current measured at anode (A)
- I_P current measured at plate (A)
- I_d discharge current (A)
- I_b electron beam current (A) measured at IC and L_{EI} or emission current for filament
- $I_{d'}$ undesired-discharge current (A)
- $f_e(E_{k,A})$ kinetic energy distribution of electrons at anode orifice
- $f_e(E_{k,IC})$ kinetic energy distribution of electrons in ion cage
- I_{Re} repeller current
- I_F filament current
- V_s Faraday cup signal at output of I/V converter (V)
- I_s secondary electron current

Mass analyser

- QMF quadrupole mass filter
- φ initial phase of RF voltage (rad)
- Ω frequency of RF voltage applied to the rods (rad/s)
- V_0 maximum amplitude of RF voltage applied to the rods

Confidential

- U_0 amplitude of DC voltage applied to the rods
- U_e amplitude of DC voltage applied to the entrance and exit lenses of LIT
- L or $2z_0$ LIT/QMF rod length
- r_0 closest distance separating the rods from the centre of QMF/LIT
- l_0 location of the entrance and exit lenses from the centre of QMF/LIT
- ω_x and ω_y radial secular ion frequencies
- ω_z axial ion frequency
- R_{max} maximum resolution
- $\phi_{QMF}(x, y, t)$ quadrupolar potential of mass filter
- $\phi_e(x, y)$ DC potential of LIT induced by potential applied to the end-cap electrodes
- a and q reduced parameters of Mathieu equation
- a_{apex}^{QMF} and q_{apex}^{QMF} values at apex of reduced parameters for QMF
- a_{apex}^{LIT} and q_{apex}^{LIT} values at apex of reduced parameters for LIT
- SIM single ion monitoring
- u unified atomic mass unit

Constants

- e charge of electron = 1.602 $\times 10^{-19}$ (C)
- m_e mass of electron = 9.1093897 $\times 10^{-31}$ (kg)
- η air dynamic viscosity at room temperature = 1.85×10^{-5} $(\mathrm{Pa} \times \mathrm{s})$ or $(\mathrm{kg}/(\mathrm{s} \times \mathrm{m}))$

Confidential

List of Figures

1 The SNIFFLES Linear Ion Trap Mass Spectrometer device concept 21

1.1 Voltage-Current characteristics and regimes of DC low-pressure electrical discharge. From left to right, (1) Dark discharges: Background ionisation, Saturation regime, Townsend regime, Corona discharges, Electrical breakdown; (2) Glow discharges: Normal glow discharge, Abnormal glow discharge; (3) Arc discharges: Glow-to-arc transition, Non-thermal arcs and Thermal arc (From page 163 of [28]). 26

1.2 Principle of DC discharge plasma with behaviour of neutrals in ground state, excited neutrals, electrons and ions for Ar gas[35]. 28

1.3 Schematic diagram of the spatial regions in DC glow discharges: (a) short cathode-anode distance and/or low pressure; (b) longer inter-electrode distance and/or high pressure (CDS = cathode dark space; NG = negative glow; FDS = Faraday dark space; PC = positive column; AZ = anode zone). Potential and electric field distributions. The cathode (left) has a negative potential, whereas the anode (right) is grounded here. The solid line (left axis) represents the potential distribution, the dashed line (right axis) the electric field distribution [35]. 30

2.1 GDES cell in the vacuum chamber, with gas inlet, power supplies and measurement devices. Items shown not actual size. 34

2.2 Photo of the GDES cell. 34

2.3 Flange-mounted GDES cell assembly. 35

2.4 Paschen breakdown curve for air (on the left), from [39] with initially pd (mmHg x cm), and for N_2 (on the right), from [57] with initially pd (mbar x cm x 10^{-1}), with plane parallel electrodes. 39

2.5 (Top) Electron kinetic energy distribution and (bottom) plate current obtained *versus* potential applied between the plate and anode for (a) a uniform distribution, (b) two adjacent uniform distributions with more electrons at higher energies and (c) two separate uniform distributions. 43

Confidential

2.6 Experimental Paschen curve for N10 GDES cell with ambient airflow inlet. From left to right, the capillary lengths are: $l_1 = 0.500$, 0.330, 0.200, 0.165, 0.098 and 0.071 m. The error bar is ± 3 standard deviations around the mean value calculated from 10 measured values. 44

2.7 V-I characteristics of discharge after breakdown. Influence of the inner diameter of the insulator is shown for N10, N15 and N20 GDES cells and capillary lengths: 0.33, 0.2, 0.165, 0.098 and 0.071 m. 45

2.8 Time dependence of the cathode current at a discharge voltage of 420 V with capillary 0.165 m, for different material and diameter insulator: (circle Macor, (square) nylon, (triangle) Teflon, and (black) 10^{-2}, (grey) $1.5\text{x}10^{-2}$ and (white) $2\text{x}10^{-2}$ m. 46

2.9 Picture of deposits for different insulator materials and under different gas flows. From left to right: Cathode; insulator; anode after a run of six hours. 1^{st} raw: Air flow and Nylon; 2^{nd} raw: Air flow and Nylon with silica gel ceramic coating; 3^{rd} raw: Air flow and Teflon; 4^{th} raw: Argon flow and Teflon; 5^{th} raw: Nitrogen flow and Teflon. 48

2.10 Scanning Electron Microscopy picture of the deposit on the anode close to the aperture (Top) . Energy Dispersive Xray spectrum of elements of the thickest deposit on the anode electrode in the vicinity of the aperture for Nylon (Middle) and Teflon (Bottom) insulator. 49

2.11 V-I characteristic of the discharge and main potential and current values used to operate the cell in glow regime with stabilisation. 50

2.12 V-I characteristic of the discharge for a new and aged cell with current limitation of the power supply with N10 GDES cell (each I/V couple is measured 4 times). 51

2.13 Evolution of the voltage and current of the discharge *versus* time with current limitation of the power supply and N10 GDES cell (each I/V couple is measured 4 times). 52

2.14 Evolution of the voltage and current of the discharge *versus* time with current limitation of the power supply with N10 GDES cell. 53

2.15 (Top) Plate current *versus* potential applied between the plate and anode for $V_{AC} =$ 400 (triangle), 420 (bullet), 450 (square), 480 (diamond), 500 (black triangle), 520 (black bullet) and 535 V (black square). The operating conditions are: N10 GDES cell and capillary length = 0.165 m. 55

2.16 Plate current *versus* potential applied between the plate and anode for Macor with inner diameter = 10^{-2} m (grey-square), nylon with inner diameter = 10^{-2} m (square), nylon with inner diameter = $1.5\text{x}10^{-2}$ m (circle) and nylon with inner diameter = $2\text{x}10^{-2}$ m (triangle). The operating conditions are: N10 GDES cell, $V_{AC} = 420$ V, I_C = $7\text{x}10^{-4}$ A and l_1 = 0.165 m. 56

2.17 Beam electron current *versus* power consumption (top) beam efficiency *versus* Beam electron current (bottom) for an aged N10 GDES cell (each I/V couple is measured 4 times). 58

Confidential

2.18 Cathode and anode currents *versus* potential applied between the plate and anode (top); plate current and current conservation *versus* potential applied between the plate and anode (bottom) for an aged N10 GDES cell. 59

3.1 Principle of the mass spectrometer. Coupling between GDES cell, EI source, and mass analyser. Gas (blue arrow), LIT ion (yellow arrow) and electron (black arrow) flows. 62
3.2 (Top) Picture of the open EI source and lenses. (Bottom) Scheme of GDES/EI coupling. 62
3.3 Total electron-impact ionisation cross-section of N_2 from [65]. 63
3.4 CPO 2D design with the electrode segmentation of GDES/EI/Lenses coupling in the plane $z0y$. The number between the electrodes corresponds to the distance in mm. From left to right: GDES: cathode and anode (orange); ion source: electron repeller, ion cage and extraction lens (1) (black); focussing (2), blocking/decelerating (3) and entrance lenses (blue) (4). 66
3.5 Example of electron trajectories from GDES anode orifice to ion cage for: V_{RE} = -30, - 70, -100 and -200 V (from the left to the right, then from the top to the bottom). 67
3.6 Number of electrons hitting the IC, graph a and hitting IC+L_E, graph b at different V_{Re} potentials at E_{kA} = 67 eV for 10 sequences with 100 electrons simulated. 68
3.7 Number of electrons hitting the ion cage *versus* V_{Re} varying between -150 to 0 V, with $E_{k,A} = 17$, 27 and 67 eV. 500 electrons are simulated with sequence #4. 69
3.8 Distributions of kinetic energies of electrons at the ion cage for uniform distribution of kinetic energies at the anode orifice. $V_{Re} = -27$ V. 70
3.9 Distributions of kinetic energies of electrons at the ion cage for a uniform distribution of kinetic energies at the anode orifice. $V_{Re} = -37$ V. 71
3.10 Distributions of kinetic energies of electrons at the ion cage for a uniform distribution of kinetic energies at the anode orifice. $V_{Re} = -80$ V. 72
3.11 Distribution of kinetic energy of electrons at the ion cage for a uniform distribution of kinetic energies at the anode orifice and for $V_A = -17$ V and $V_{Re} = -27$ V. 73
3.12 (Top) Mechanical design to test EI source with Faraday cup. (Bottom) Electrical design to test EI source with Faraday cup. 74
3.13 Evolution of filament current and emitted current according to time at $p_M = 3.99 \times 10^{-5}$ Pa. 76
3.14 Electron currents in the ion source according to the potential applied to the repeller for three values of the potential applied to the filament. The potential applied to the ion cage is 3 V. 77
3.15 Faraday cup detector signal *versus* potentials applied to the lenses. 78
3.16 Faraday cup detector signal *versus* electron current and pressure in the vacuum chamber. (Top) Signal detected by the Faraday cup detector versus I_b. (Middle) Zoom of the top curve for low values of I_b. (Bottom) Signal detected by the Faraday cup detector versus p_M when $I_b = 10^{-5}$ A. 79

Confidential

3.17 GDES-EI source coupling with Faraday cup detector. (Top) Scheme of testing device. (Middle) photo of GDES and EI/lenses/Faraday cup mounted on a flange. (Bottom) Electric testing device. 80
3.18 Electron currents measured at the ion cage (top) and repeller (middle). Faraday cup detector ion signal (bottom) *versus* potential applied to anode for different values of potential applied to repeller. 82
3.19 Electron currents measured at the ion cage (top) and repeller (middle). Faraday cup detector ion signal (bottom) *versus* potential applied to repeller for different values of potential applied to anode. 83
3.20 Simulation: electron currents at the ion cage I_{IC}, at the ion cage and extract lens I_b, and at the repeller I_{Re} versus the potential applied to the anode for different ranges of electron kinetic energy at the anode orifice. 85
3.21 Experimental and simulation data: 86

4.1 (Right) The ideal quadrupole mass filter electrodes having the hyperbolic cross section and with the equipotential lines for a quadrupole field (From [58]). (Left) Mass filter with cylindrical rod and potentials applied to the rods (From [76]). 90
4.2 (From left to right and from top to bottom) Three stability zones of the Mathieu equation. Three stability zones of the Mathieu equation for the directions 0x (a) and 0y (b). First zones of stability of the mass filter. Zoom on the first stability diagram (From [76]). 93
4.3 Principal stability diagrams of a QMF for m/z: 10, 50, 100, 200 and 300 in (U_0, V_0) plane, for $r_0 = 4\text{x}10^{-3}$ m and $\Omega/2\pi = 10^6$ Hz. 94
4.4 Basic design of two-dimensional linear ion traps. On the left, the linear ion trap mass spectrometer was created from a triple quadrupole mass filter [90]. On the right, a quadrupole structure with hyperbolic rod cut into three axial sections [91]. 95

5.1 (Top) General CPO 2D (ZX plane) design with electrode location (in mm), including, from left to right, GDES cathode and anode, repeller (Re), ion cage (IC), (1) extraction lens, (2) focussing lens, (3) decelerating lens, (4) entrance lens, LIT-50 and (5) exit lens. CPO design 3D view including only entrance and exit lenses and LIT. (Bottom) CPO 3D design with LIT, entrance (4) and exit (5) end-caps. 100
5.2 Detail of the "single ion monitoring", SIM. 102

6.1 Some ion trajectories for each Cartesian coordinate versus injection time for configuration #1 and different initial phases of the RF voltage (from left to right, the phase equals 0 and $\pi/2$). 106
6.2 Some ion trajectories for each Cartesian coordinate versus injection time for configuration #3 and different initial phases of the RF voltage (from left to right and from top to bottom, the phase equals 0, $\pi/2$, π and $3\pi/2$). 106

Confidential

6.3 Number of injected ions *versus* injection time for different initial phases of the RF voltage. (**Top**) configuration #1, (**middle**) configuration #3, and (**bottom**) the average value for both configurations. 108
6.4 Injected ion density *versus* position x for two potential configurations and different initial phases of the RF voltage. (**Top**) configuration #1, (**middle**) configuration #3, and (**bottom**) average value for both configurations. 110
6.5 Injected ion density *versus* position y for two potential configurations and different initial phases of the RF voltage. (**Top**) configuration #1, (**middle**) configuration #3, and (**bottom**) average value for both configurations. 111
6.6 Injected ion density *versus* position z for two potential configurations and different initial phases of the RF voltage. (**Top**) configuration #1, (**middle**) configuration #3, and (**bottom**) average value for both configurations. 112
6.7 Injected ion density *versus* velocity v_x for two potential configurations and different initial phases of the RF voltage. (**Top**) configuration #1, (**middle**) configuration #3, and (**bottom**) average value for both configurations. 113
6.8 Injected ion density *versus* velocity v_y for two potential configurations and different initial phases of the RF voltage. (**Top**) configuration #1, (**middle**) configuration #3, and (**bottom**) average value for both configurations. 114
6.9 Injected ion density *versus* velocity v_z for two potential configurations and different initial phases of the RF voltage. (**Top**) configuration #1, (**middle**) configuration #3, and (**bottom**) average value for both configurations. 115

7.1 Number of ions versus confinement time for two potential configurations. (Top) configuration #1, (middle) configuration #3, and (bottom) the average value for both configurations. 118
7.2 QMF and LIT main stability diagram. 119
7.3 Top: $\phi_e(z)$ computed by CPO for LIT-8, LIT-20, LIT-30, LIT-40 and LIT-50 and $r_0 = 4\text{x}10^{-3}$ m. Bottom: $\phi_e(z)$ for LIT-8 for 2^{rd}, 4^{th} and 6^{th} orders of the polynomial approximation. 121
7.4 Axial (top) and radial (bottom) trajectory spectra of LIT-50. The operating conditions are: $x(0) = 0.1$, $y(0) = 0.1$ and $z(0) = 2\text{x}10^{-2}$ m; $v_x(0) = v_y(0) = v_z(0) = 0$ m/s; m/z: 300; $\Omega/2\pi = 1$ MHz and $r_0 = 4\text{x}10^{-3}$ m. 122
7.5 Axial period of LIT-50 *versus* z(0) position: in axial direction with $x(0) = y(0) = 0$ m, and in radial and axial direction with $x(0) = y(0) = 10^{-4}$ m, at different phases. . . . 124
7.6 (Square): $V_{0,max}^{LIT}$ versus $z(0)$ for the LIT-50 at different m/z: 50, 100 and 300. (Line): $V_{0,max}^{QMF}$, the theoretical maximal value for the quadrupole mass filter. 125
7.7 (Square): $U_{0,apex}^{LIT}$ versus $z(0)$ for the LIT-50 at different m/z: 50, 100, 200 and 300. (Line): $U_{0,apex}^{QMF}$, the theoretical maximal value for the quadrupole mass filter. 126

Confidential

7.8 (Top) Potential curve $\phi_e(0,z)$ (●) to axial position z_0 of LIT-50, with according $z_0 = 25\text{x}10^{-3}$m and $r_0 = 4\text{x}10^{-3}$m, $z_{max,inj}$ is the maximal axial extension at injection for an ion source at 3 (×). $z_{max,nkT}$ is the maximal axial extension for an ion thermalised at nkT with $n = 1$, 3 and 10. $z_{max,conf}$ maximal axial extension of the confined ions when $U^{LIT}_{0,apex} = U'_0$ (LIT operated at apex). (Bottom) Expected maximal axial extensions of the ion cloud versus LIT lengths (LIT-8, LIT-20, LIT-30, LIT-40, LIT-50 and LIT-60) with $r_0 = 4\text{x}10^{-3}$m. $z_{max,inj}$ at 3 (×) and 5 (+) eV. $z_{max,nkT}$ at nkT with $n = 1$ (□) , 3 (○) and 10 (△) . (★) $z_{max,conf}$. 129

7.9 Signal intensity variation for Xe ions trapped within Liverpool's LIT without buffer gas (top) and with increase of He buffer gas pressure (bottom). (From unpublished works with courtesy of University of Liverpool). 130

7.10 Adaptation of the Single Ion Monitoring sequence to increase sensitivity and resolution with DC confinement potential switched to zero during injection and ion cooling. 131

Confidential

List of Tables

2.1 GDES cell references according to insulator materials and inner diameters. 34
2.2 Length l_1 and conductance C_1 of capillary inlet according to glow discharge cell and vacuum chamber pressures for $d_1 = 6.3\text{x}10^{-5}$ m and $d_A = 3\text{x}10^{-2}$ m. 38
2.3 Estimated pressure in GDES cell for six values of capillary length around Paschen minimum. 40
2.4 Calculation of C_1 the capillary conductance, Q_1 the mass-flow in the capillary, p_{GD} the GDES cell pressure, C_A the anode orifice conductance, and Q_T the throughput of the turbo molecular pump from the measured pressures in the vacuum chamber, in relation with l_1, the capillary length. 40
2.5 Some operating points on the V-I characteristic of the GDES cell, corresponding emitted-electron current intensity, power consumption and efficiency for $V_{PA} = 40$ V for an aged N10 GDES cell. 57

3.1 Polarisation potential applied to anode V_A according to electron kinetic energy at anode orifice $E_{k,A}$ for three values of the electron kinetic energy inside ion cage, $E_{k,IC}$, with ion cage at $V_{IC} = 3$ V. 64
3.2 Comparison between filament and GDES of currents and detector signal, for V_{Re} = -80 V and V_A = -57 V, corresponding to optimal operating conditions to have electron kinetic energy in the ion cage centred at 70 eV. 81

5.1 Potential applied to the rods during confinement, 2D potential and reduced parameters of Mathieu equations. 101
5.2 Potentials applied to the electrodes during injection stage 104
5.3 Potential applied to the electrodes during confinement stage. 104

6.1 Number of ions reaching the entrance lens after a round trip in the LIT during injection for two single ion monitoring (SIM) sequences, two confinement potential configurations and different phases of the RF potential. 116

7.1 Identification of some measured peaks in figure 7.4 according to their magnitude and frequency. 123

Confidential

Confidential

Introduction

The work described in this thesis dissertation was undertaken during the European FP7 project SNIFFLES (from January 1^{st} 2012 to July 1^{st} 2015) . "The concept of the SNIFFLES project is to develop a state-of-the-art miniature and portable electronic gas sensor capable of detecting hidden persons and illegal substances (drug, explosive), providing a cost effective and scalable technology to complement the work of sniffer dogs", for National security and border control. This project involves a large consortium constituted by two academic and seven industrial partners.

Different techniques can be employed as drug or explosive detectors [1, 2]. The gas sensor used in the project is based on mass analysis by means of a Linear Ion Trap (LIT). Mass spectrometry is one of the most powerful analytical techniques among many others, as it is almost universally applicable, chemically specific, sensitive and fast. More importantly, it is able to analyse samples in complex matrices through tandem MS experiments. Generally these performances are obtained with laboratory-scale instruments. In fact, it is complex to adapt such a device to obtain a portable mass spectrometer for in-the-field applications. Therefore, miniature mass spectrometers are of growing interest due to their potential of realizing *in situ* chemical analysis. The initial construction and application of miniature mass spectrometers can be traced back to the ambitious Viking project of NASA in 1970s [3], in which miniature gas chromatograph mass spectrometers (GC/MS) were built and used to analyse chemical compositions of Martian atmosphere and soil [4]. More applications of miniature mass spectrometers were implemented later in public safety and health, environmental protection, industrial process monitoring and many other areas [5, 6, 7, 8, 9].

The proposed portable mass spectrometer is composed of two ionisation sources addressing two kinds of samples: volatile compounds of ambient air and particles deposed onto solid surfaces (figure 1). For volatile compounds, an electron ionisation (EI) at 70 eV (or less) source is used in the vacuum chamber (internal ion source). Examination of state of art reveals different kinds of external desorption and ionisation techniques easy to implement in portable instruments, as they do not require a sample preparation (for instance, [10] gives a large list of these techniques). In the prototype, the partners (Q-Technologies Ltd and University of Liverpool) in charge of the ex-

Confidential

ternal ionisation have chosen the Desorption Atmospheric Pressure Chemical Ionisation (DAPCI) technique, for direct analysis of compounds without sample preparation. In DAPCI, a corona discharge is generated by applying a high DC voltage (3-6 kV) toward a sharp needle, using a carrier gas. The analyte is desorbed and ionized directly from the surface [11, 12]. APCI produced more effective ionisation for large mass-ranges (few thousands). With tandem mass spectrometry, DAPCI greatly enhances the selectivity and information content of the experiment [13].

Gas samples are introduced by means of a pulsed inlet valve to reduce gas load for the pumping system [14]. The gases are evacuated from the vacuum chamber by the coupling of a getter and sputter ion pumps (SAES Getter Group is responsible for the vacuum system within SNIFFLES). It is a system operated by battery and packaged into a convenient portable case. However, it requires a docking station with a diaphragm pump and a turbo pump for device regeneration, *i.e.* gas removal, getter reactivation and battery recharging.

The mass analyser is a LIT having hyperbolic shaped electrodes in order to increase resolution and sensitivity. Typically, portable devices employ (for easy-fabrication) shaped electrodes, for instance a rectilinear ion trap was proposed by Cooks laboratory [15]. The design of the University of Liverpool describes a device with reduced-size electrodes and the fabrication involves digital light processing (DLP) realised by TWI Ltd. A metal thin film is deposited at the electrodes by ink printing technique (XaarJet AB). The realisation of the LIT is achieved and has been tested in a vacuum chamber without significant desorption [16]. The design and the potentials applied to the coupling of an open EI ion source with the LIT have been improved by numerical modelling of the design and ion trajectories to increase sensitivity (by University of Liverpool, Q-Technologies Ltd and Aix-Marseille Universtité) [17].

The Electronic Control Unit (ECU) schedules the mass analysis sequences while it delivers the potentials to be applied to the electrodes (Q-Technologies Ltd and University of Liverpool are in charge of ECU). TWI Ltd deals with the Graphical User Interface (GUI) that controls ECU. The targeted compound to be analysed is chosen among a list of substances. Identification of the targeted compound is based on the detection of 3-4 ion fragments, for instance with electron impact ionisation, the LIT operated in Single/Selective Ion Monitoring mode (SIM).

Besides analytical work have been performed to define the human chemical signatures for a rapid identification. University of Liverpool and Q-Technologies Ltd have shown significant detection of NH_3, CO_2, water and volatile organic compounds using a portable quadrupole mass spectrometer using a membrane probe [18, 19].

Da Vinci Laboratory Solutions conducts comparative studies of analytes by means of lab-scale mass spectrometer and a SNIFFLES prototype, to perform comparative tests with detection dogs of Wagtail International.

2013 is an important date for the mass spectrometry community as it marks the 100^{th} anniversary of the publication of Sir Joseph John Thomson's monograph "Rays of Positive Electricity

Confidential

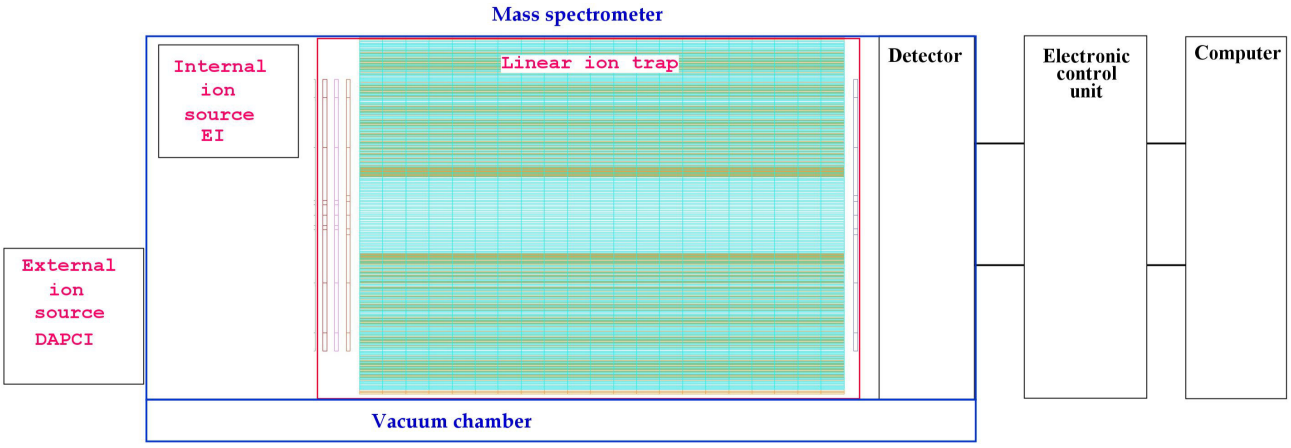

Figure 1: The SNIFFLES Linear Ion Trap Mass Spectrometer device concept

and Their Application to Chemical Analysis". Thomson started his investigation of electrical discharges in gases in 1897, leading to the discovery of the electron (cathode rays) [20]. Later, in 1913, he observed that positive rays (ions) formed from residual gases in cathode was differentially deflected depending on their mass by magnetic and electrostatic fields as they made diverging traces on a photographic plate, providing the first mass spectrometer [21].

In this dissertation, electric discharge in gas and mass spectrometry are also combined. In the first part, an electric discharge in a glow regime is employed to generate low temperature electrons for molecule ionisation in an open electron impact ion source to operate at low vacuum. In the second part, the simulation studies of ion injection and confinement in a LIT allow us to propose solutions in order to improve both sensitivity and mass resolution of the analyser prototype developed by the partners. The proposed devices and improvements must take into account the portability of the instrument. The results of these works are input data for the ECU and the vacuum system of the prototype and its future releases.

Confidential

Confidential

Part I
Glow discharge electron impact ionisation

Confidential

Confidential

Chapter 1

Some elements of theory about Glow Discharges

Confidential

1.1 Discharge

Faraday in the 1830 studied the discharges created in glass tubes filled with gas at a low pressure (≈100 Pa) [22], and later, during the 1870 by Crookes [23]. Their investigations resulted in a better understanding of the working principles and properties of gas discharges.

Paschen in 1889 investigated the minimum potential difference that was needed to create sparks between two electrodes in a glass tube [24]. He found that this voltage depends on the type of gas, the pressure in the tube, p, and the gap between electrodes, d. Moreover, the minimum breakdown voltage was a function of the product between pressure and gap distance, pd. At this moment, the breakdown voltage can be measured experimentally, without understanding of the breakdown processes.

In 1909, Townsend proposed a theory that could explain the breakdown phenomenon, describing the microscopic processes such as ionization of atoms by electron impact, collision, and secondary emission at the cathode by ion impact [25].

Further studies showed that the gas discharges consist of ionized gas, containing neutral and both positively and negatively charged particles. J. J. Thomson in 1913, developed a first ion source for a mass spectrometer [21]. In 1928, Langmuir [26] introduced the word *"plasma"* to describe the ionized gas that is created in a gas discharge.

A gas discharge can be created by applying a direct current (DC), capacitively coupled radio-frequency RF (RIE, PECVD), inductively coupled RF (ICP, TCP, Helicon) and microwaves (ECR, Surfatron). The technological applications of plasmas formed in these sources are numerous and include thin film deposition, semiconductor processing, materials treatments (modification of surface physics and surface chemistry, sterilization), lamps, light sources and displays, waste treatment and materials analysis [27].

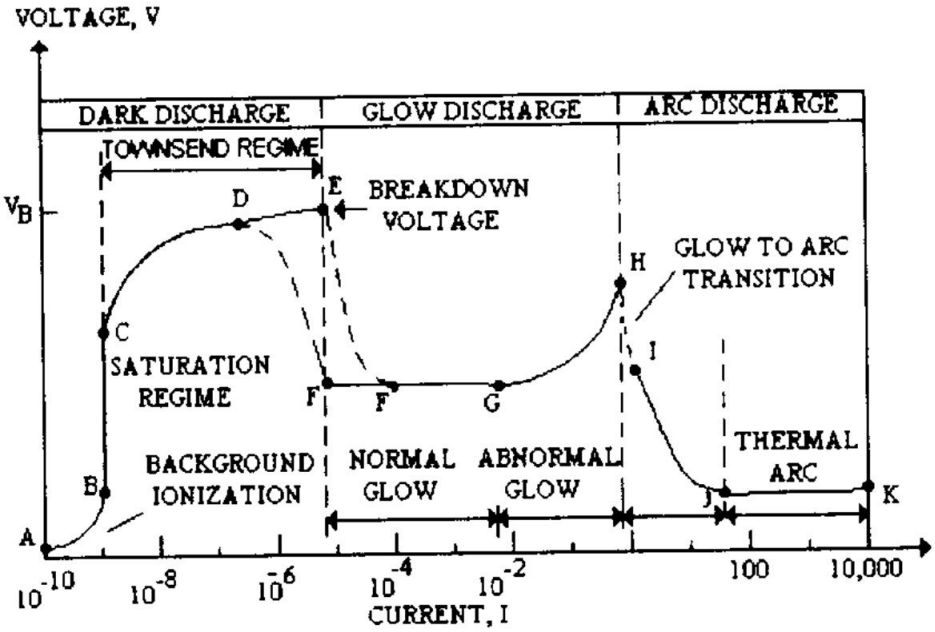

Figure 1.1: Voltage-Current characteristics and regimes of DC low-pressure electrical discharge. From left to right, (1) Dark discharges: Background ionisation, Saturation regime, Townsend regime, Corona discharges, Electrical breakdown; (2) Glow discharges: Normal glow discharge, Abnormal glow discharge; (3) Arc discharges: Glow-to-arc transition, Non-thermal arcs and Thermal arc (From page 163 of [28]).

1.2 Voltage-Current characteristics et regimes

1.2.1 Voltage-Current characteristics

The figure 1.1 is an illustrative plot of the voltage *versus* current (or Voltage-Current characteristics) of a DC electric discharge in a gas. On the curve describing a complex (non-linear) shape, three main regions can be distinguished, which belong different types of discharge, as are many plasma phenomena. The main characteristics of the discharge such as the breakdown voltage, the voltage current characteristic and the structure of the discharge depend on the geometry of the electrodes, the gas used, the pressure and the electrode material. It has to be pointed that all regimes have found applications [28, 29].

1.2.2 Dark Discharge regime

The regime between A and E on the voltage-current characteristic is termed a dark discharge because the discharge remains invisible (except for corona discharges and the breakdown itself).

In the region of lowest voltages (A-C), the current depends on the concentration of charged particles, which are produced by external sources like cosmic rays, radioactive minerals, and/or by illumination of the cathode (photo-emission). There is only a small increase of current with

increasing voltage, that is the background ionization stage (called also *"Geiger regime"*), then the current saturates with increase in voltage.

The region (C-E) is called the *"Townsend discharge"*. In the region (C-D), the current increases exponentially, the voltage is high enough for gas ionization and secondary electron emission leading to an avalanche of electron and ion production. The discharge is still not self-sustaining, *i.e.* it exists only because of an external ionisation source.

In the (D-E) region, the *"Townsend discharge"* is self-sustained, the current increases by several order of magnitude almost at a constant plasma voltage value. An external resistance is necessary to control the current in this regime, called *"Corona discharge"*. If the coronal currents are high enough, corona discharges can be technically 'glow discharges', visible to the eye. For low currents, the entire corona is dark, as appropriate for the dark discharges. Related phenomena include the silent electrical discharge, an inaudible form of filamentary discharge, and the brush discharge, a luminous discharge in a non-uniform electric field where many corona discharges are active at the same time and form streamers through the gas.

Beyond point E, the electrical breakdown occurs with the addition of secondary electrons emitted from the cathode due to ion or photon impact, at the breakdown voltage denoted as V_B. The discharge currrent can be limited by the internal resistance of the power supply connected between the two electrodes. The breakdown voltage, for a given gas and electrode material, depends on the product of the pressure and the distance between the electrodes, as expressed in Paschen's law [24].

The initially homogeneous electric field becomes distorted because of the space charges accumulated in the discharge gap and the *"Townsend discharge"*, changes to the *"normal glow discharge"*.

1.2.3 Glow Discharge regime

In the glow discharge regime the plasma is luminous. The gas glows because the electron energy and density are high enough to generate visible light by excitation collisions.

After a discontinuous transition from E to F, the voltage is almost independent of the current over two orders of magnitude in the normal glow discharge regime (F-G). The current density remains constant with the discharge growing larger in size with increase in current [30]. This means that the plasma is in contact with only a small part of the cathode surface at low currents. As the current is increased from F to G, the fraction of the cathode occupied by the plasma increases, until plasma covers the entire cathode surface at point G. From G, the voltage increases significantly with the increasing current in order to force the cathode current density above its natural value and provide the desired current, called *"abnormal glow"*.

Starting at point G and moving to the left, a hysteresis is observed in the voltage-current characteristic. The discharge maintains itself at considerably lower currents and current densities than at point F and only then makes a transition back to Townsend regime.

The applications of glow discharge include fluorescent lights, DC parallel plate plasma reactors,

Confidential

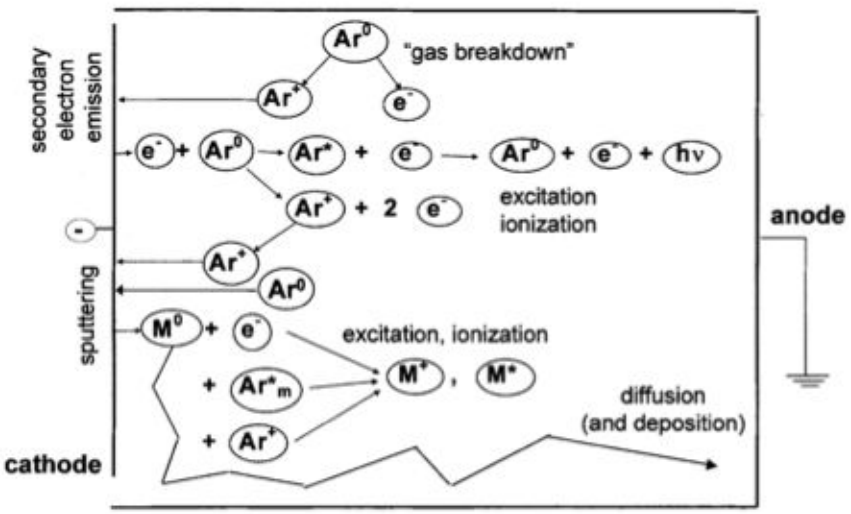

Figure 1.2: Principle of DC discharge plasma with behaviour of neutrals in ground state, excited neutrals, electrons and ions for Ar gas[35].

'magnetron' discharges used for depositing thin films, and electron bombardment plasma sources.

1.2.4 Arc Discharge regime

The current increase from 0.1 to 1 A leads to an important decrease of the discharge voltage and the transition to the arc discharge occurs. At point H, high current will result in the heating of the gas medium and cathode. At increased cathode temperatures, the secondary electrons are liberated by thermionic emission. In addition, the high discharge current induces a growth of the gas temperature. If the DC power supply has a sufficiently low internal resistance, the discharge will undergo a glow-to-arc transition. The voltage necessary to sustain the discharge will decrease and will be up to 10 times smaller. After J, the voltage increases slowly as the current increases.

1.3 DC Glow Discharge

The glow discharge is suitable for most material processing applications. The Townsend discharge regime is too weak and the arc discharge regime is too hot. It characterisation is generally done in a closed glass tube at low pressure (133.32-1333.2 Pa), the simplest way to obtain regularities of ionisation [31, 32, 33, 34].

1.3.1 Basic plasma process

When the DC potential applied across the cathode and anode electrodes of the discharge is sufficiently high, the gas is ionised in electrons and positive ions. A schematic diagram of a DC discharge plasma is presented in figure 1.2.

Confidential

In this example, the gas is argon (Ar). The electrons are accelerated by the electric field in front of the cathode towards the anode and collide with the gas atoms, losing kinetic energy. The collisions are elastic and inelastic. In elastic collisions, the kinetic energy of electrons is low: there is conservation of both momentum and kinetic energy. Only deviation of particles with exchange of momentum and kinetic energy occurs.

In inelastic collisions, a part of the kinetic energy is changed into internal energy of the atom or molecule. The neutrals are excited by the electron collision (excitation), which is often followed by a de-excitation with emission of radiation. That explains the name of the "glow" discharge. Furthermore, neutral ionisation happens by inelastic collisions, creating new electrons and ions. That makes the glow discharge a self-sustaining plasma.

Besides, the electrode plays an essential role to sustain the plasma by secondary electron emission. The argon ions, as well as fast argon atoms, which are carried off by ions, have sufficient kinetic energy to give rise to sputtering on the cathode. Atoms/molecules (denoted as M) are ejected from the cathode, by diffusion they cross the plasma, then a part of them reaches the anode. The sputtered atoms can also become ionized and/or excited in the plasma. The sputtering on the cathode leads to deposit a thin film at anode, which is important for several applications [36], however interfering with the stability of the discharge operating point for our application. Moreover, the use of air (see next Chapter) renders more complex the plasma behaviour due to additional fragmentation and chemical reactions.

Confidential

1.3.2 Discharge regions and potential

The potential difference applied between the two electrodes is not linearly distributed between the cathode and anode 1.3. The potential drops in a few millimetres after the cathode. The first region adjacent to the cathode is the "cathode dark space" (CDS) or "sheath" where the electric field is the strongest. The electrons are violently accelerated. The second region, which occupies the largest part of the discharge, is the "negative glow" (NG). The potential is almost constant and slightly positive: it is denoted as the "plasma potential". In this region, the current is only induced by electrons, which move faster than ions.

For short distances between the cathode and anode, the potential goes back to zero at the anode across a short region called the "anode zone" (AZ). The sheaths fields are such as to repel electrons trying to reach electrode [36].

When the distance between the cathode and anode is relatively long, there are additional regions: the 'Faraday dark space' (FDS) and the 'positive column' (PC). The electric field is slightly negative to conduct the electrons toward the anode.

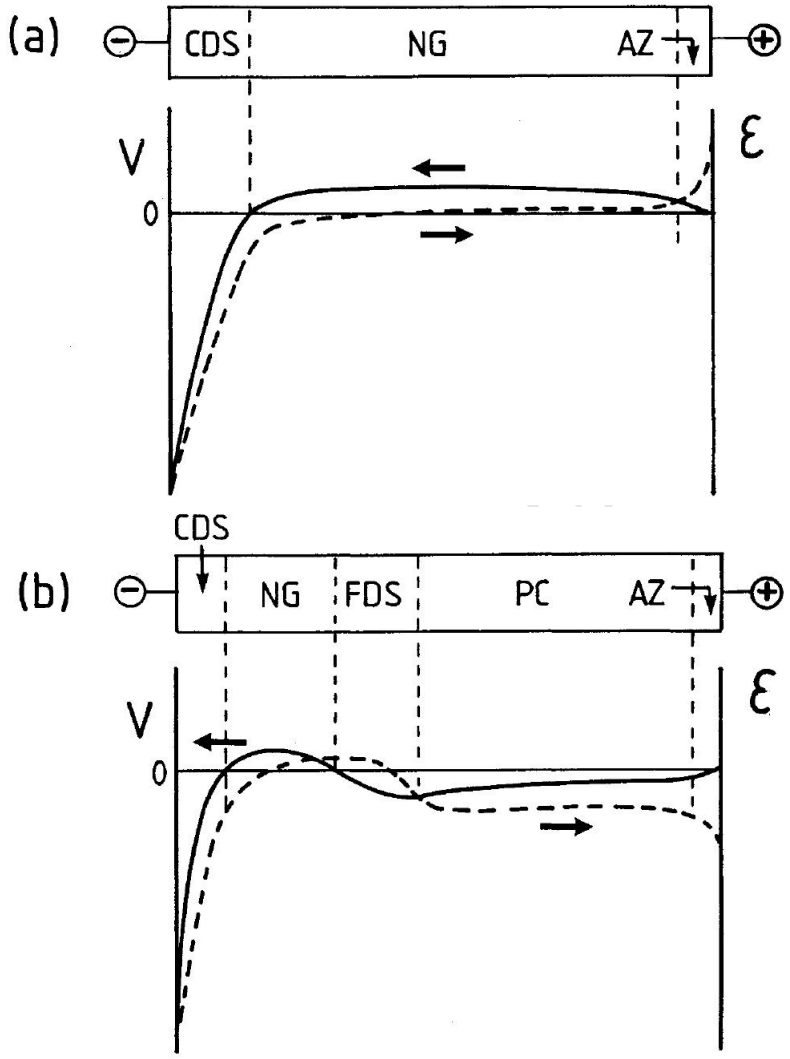

Figure 1.3: Schematic diagram of the spatial regions in DC glow discharges: (a) short cathode-anode distance and/or low pressure; (b) longer inter-electrode distance and/or high pressure (CDS = cathode dark space; NG = negative glow; FDS = Faraday dark space; PC = positive column; AZ = anode zone). Potential and electric field distributions. The cathode (left) has a negative potential, whereas the anode (right) is grounded here. The solid line (left axis) represents the potential distribution, the dashed line (right axis) the electric field distribution [35].

1.4 DC Glow discharge in mass spectrometry

Low-pressure glow discharges operated with a DC supply are one of the most studied non equilibrium plasma discharges of a simple mechanical conception. DC glow discharge operates at room temperature reducing desorption phenomena in the vacuum chamber of a mass spectrometer [37, 29, 38] and can generate either ion or electron beams [39, 40, 41, 42, 43]. So, a DC glow discharge cell with a cold cathode can be used as a low power source of electrons, with reduced out-gassing phenomena compared to a heated filament.

DC glow discharge can occurs with several configurations and shapes of the electrodes (anode and cathode): two simple parallel plane electrodes [35, 27, 39, 44], plane anode-cylindrical hollow cathode, hollow cathode with holes, hollow anodes [45]. Hollow anode have been employed in mass spectrometer as electron source [46].

A simple plate DC glow discharge, denoted as Glow Discharge Electron Impact (GDEI), has been proposed first in 2005 by Handberg (Phd thesis [47]) then by Gao *et al.* in a paper [48]. GDEI is a source of electrons that are admitted into a (2D or 3D) trap where sample is introduced and ionised (internal ionisation mode) by EI. GDEI has been coupled to Cylindrical Ion Trap (CIT) and Rectilinear Ion Trap (RIT) mass analyser [47, 49, 8].

GDEI/CIT coupling has been employed in a Field-Portable Mass Spectrometer System, ChemSense 600 of ICx Technologies [50, 51, 52].

In this work, a DC Glow Discharge cell with planar electrodes generating an electron beam, inspired by Gao *et al.* [48], is tested using different materials and diameters of the cylindrical ring insulator in typical operating conditions, *i.e.* with an inlet flow from atmospheric air. The characterisation of the discharge is deeply investigated and the kinetic energy of the electrons available for ionisation is approached. Contrary to that previous published works, in order to reduce the dispersion of kinetic energy of electrons at impact, this Glow Discharge Electron Source (GDES) is coupled to an open Electron Impact source in substitution of a filament unable to work at low vaccum (getter pump). The positive ions created in the ion cage of the source are then axially admitted in a Linear Ion Trap with hyperbolic-shaped electrodes.

Confidential

Confidential

Chapter 2

Experimental characterisation of GDES

The objective of these experimental works concerns the definition of the operating conditions of the glow discharge, the characterisation of the discharge and the characterisation (intensity and kinetic energy distribution) of the beam of electrons available for further ionisation.

Confidential

2.1 Design

2.1.1 GDES cell

The Glow Discharge Electron Source cell (denoted as GDES cell) is placed in a vacuum chamber (figures 2.1 and 2.2). The cell consists of two disk stainless steel plate cathode and anode, which are separated and fixed by a ring insulator. The cathode and anode electrodes are then separated by a distance of $d_{AC} = 6.6\text{x}10^{-2}$ m. The external face of the cathode is drilled to receive a 1/4" OD gas inlet tubing. The anode aperture has a diameter of $d_A = 3.3\text{x}10^{-4}$ m. Two Viton O-ring seals between the cathode and insulator and between the anode and insulator are used to maintain a higher pressure in the GDES cell than in the vacuum chamber.

This simple mechanical conception permits to employ different ring insulators. Three inner diameters 10^{-2}, $1.5\text{x}10^{-2}$, and $2\text{x}10^{-2}$ m and four different materials Teflon, Nylon, Macor and Pyrex were tested insert (see table 2.1).

A disk stainless steel plate located in front of the anode aperture $2\text{x}10^{-2}$ m away collects electrons emerging from the anode aperture (for characterisation of the electron beam, see later). This plate is also denoted as the electron collection plate.

2.1.2 GDES assembly and vacuum device

The figure 2.3 shows a picture of the GDES cell mounted on flange.

A 1/4" OD stainless steel tube passes through the flange. The tubes are connected with Swagelok fittings. Inside the vacuum chamber, the assembly comprises a 1/4" fitting with a PTFE union to ensure the electric insulation between the cathode, at a higher negative voltage, and the flange,

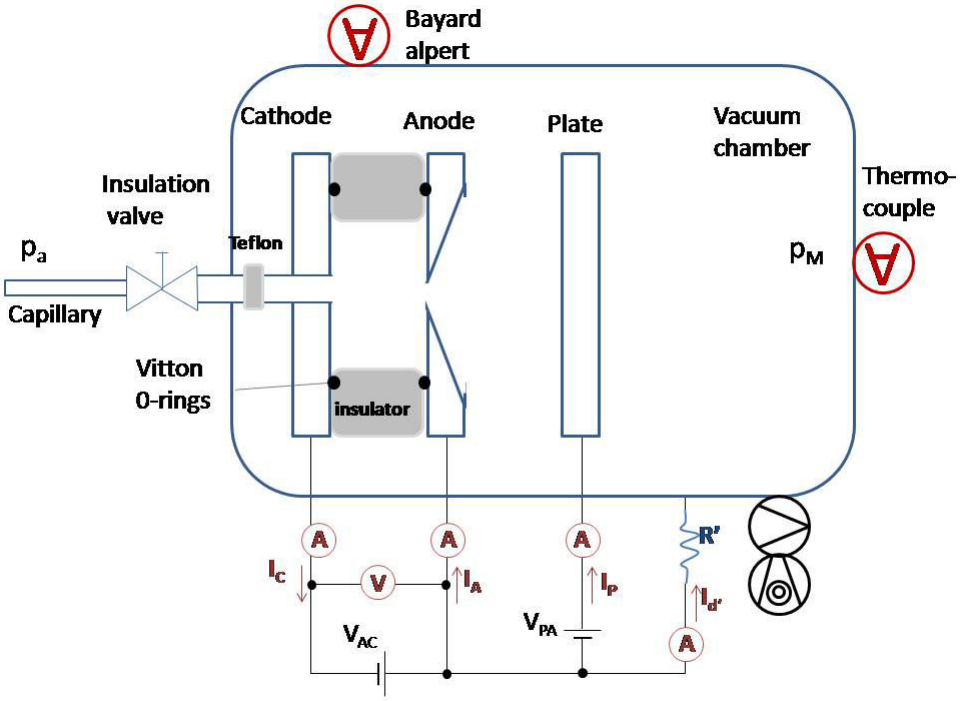

Figure 2.1: GDES cell in the vacuum chamber, with gas inlet, power supplies and measurement devices. Items shown not actual size.

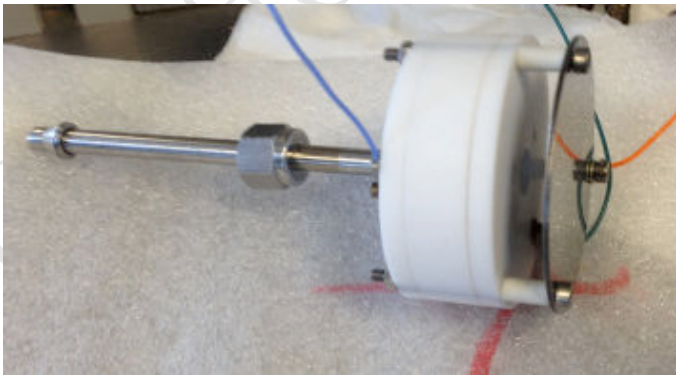

Figure 2.2: Photo of the GDES cell.

	Insulator material			
Inner diameter of GDES cell (m)	Teflon	Nylon	Macor	Pyrex
10^{-2}	T10	N10	M10	/
$1.5x10^{-2}$	T15	N15	M15	P15
$2x10^{-2}$	T20	N20	M20	/

Table 2.1: GDES cell references according to insulator materials and inner diameters.

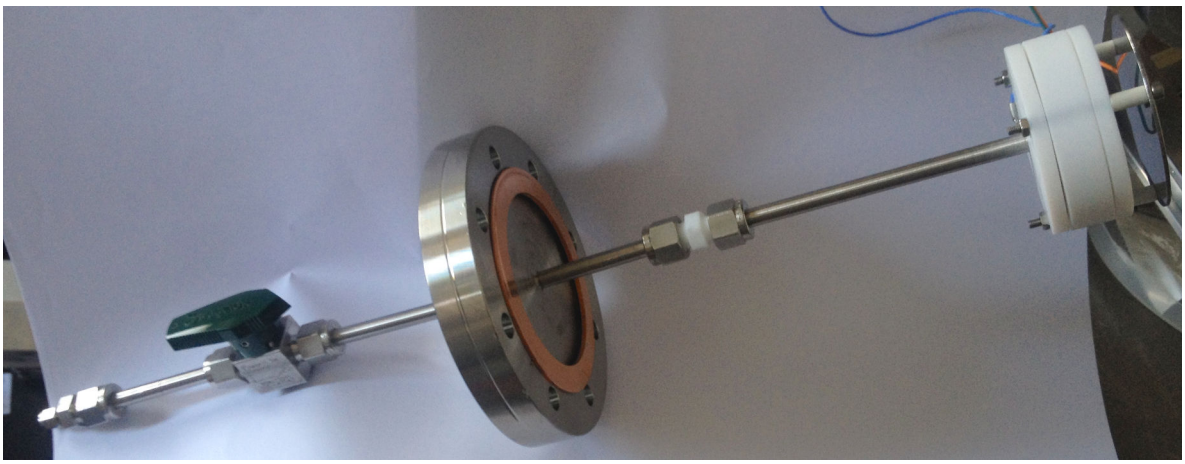

Figure 2.3: Flange-mounted GDES cell assembly.

which is grounded. Outside, the assembly comprises a quarter-turn valves and a reducing union with $7.94\text{x}10^{-4}$ m fitting for the capillary (not mounted in the photo). The capillary inlet is PEEK tubing OD 1/32" and ID $6.3\text{x}10^{-5}$ m. The quarter-turn isolation valve at GDES inlet makes easily to shut off gas flow when changing capillary tubing.

The pumping system is composed of a roughing (TriScrollTM 300 Series Dry Scroll Vacuum Pump; Varian, Inc) and turbo-molecular pumping device (Turbo V250 Macro-torr; Varian, Inc). Two types of vacuum gauge are used: Thermocouple and Bayard-Alpert gauges, to measure the vacuum chamber pressure, p_M, continuously from $1.01325\text{x}10^{5}$ to $1.33322\text{x}10^{-7}$ Pa.

2.2 Fluidic system

There is a gas flow in the GDES cell from ambient to vacuum chamber. Gas inlet flow from ambient room air passes through a capillary and enters in the cell by a centred cathode aperture. Then, the gas effuses from the centred hole ($d_A = 3.3\text{x}10^{-4}$ m in diameter) in the anode toward the vacuum chamber. Both the gas load for the pumping system of the vacuum chamber and the pressure inside the GDES cell must be estimated to locate the operating point of the discharge.

2.2.1 Capillary mass-flow

The capillary inlet induces a pressure drop in GDES cell. The capillary has the lowest conductances, while the other tubing and the orifice placed in series with the capillary have higher conductance. For instance, between the capillary inlet and the enclosed volume of GDES cell there is a constriction. It is a short round tube of diameter $5\text{x}10^{-4}$ m and length 10^{-3} m in cathode. Its effect can be neglected, as its conductance is larger than the capillary one. A laminar viscous gas flow passes through the capillary. The Hagen-Poiseuille equation gives Q_1, the mass-flow in capillary [53, 54, 55]:

Confidential

$$Q_1 = \frac{\pi\, d_1^4}{128\,\eta\, l_1}\frac{p_a + p_{GD}}{2}(p_a - p_{GD})\ (\mathrm{Pa}\times \mathrm{m}^3/\mathrm{s})\ \text{or}\ (\mathrm{W}) \tag{2.1}$$

where p_a the atmospheric pressure, p_{GD} the pressure inside the GDES cell, η the air dynamic viscosity at room temperature; d_1 the internal diameter of capillary and l_1 the length of capillary. The fact that a medium density is introduced (in the above Hagen-Poiseuille equation for gas flows), merely represents a linear approximation of the compressibility effect, which is sufficient for small Mach number flows only [56].

For air at room temperature, Q_1 is then expressed by:

$$Q_1 = \frac{663.3\, d_1^4}{l_1}(p_a + p_{GD})(p_a - p_{GD}) \tag{2.2}$$

Numerical application of Q_1 on table 2.4 according to capillary length l_1, pressure p_{GD} and p_M.

From the relation between the conductance and mass-flow, C_1 can be expressed by:

$$C_1 = \frac{Q_1}{(p_a - p_{GD})} = \frac{663.3\, d_1^4}{l_1}(p_a + p_{GD})\ (\mathrm{m}^3/\mathrm{s}) \tag{2.3}$$

In normal operating conditions, it can be assumed that $p_a \gg p_{GD}$. The conductance is then approximated by equation:

$$C_1 = \frac{663.3\, d_1^4}{l_1}p_a \tag{2.4}$$

Numerical application of C_1 on table 2.2 according to capillary length l_1, pressure p_{GD} and p_M.

2.2.2 Anode orifice conductance

The pressure inside the GDES cell is low enough to have a molecular flow passing through the anode orifice, considered as a thin plate orifice. The conductance is then calculated from [56, 54]:

$$C_A = \frac{v}{4}\frac{\pi\, d_A^2}{4}\ (\mathrm{m}^3/\mathrm{s}) \tag{2.5}$$

where d_A is the diameter of the anode orifice and v the average velocity of particles given by:

$$v = \sqrt{\frac{8\,k\,T}{\pi\, m}}\ (\mathrm{m/s}) \tag{2.6}$$

v is chosen equal to 463 m/s for air at room temperature and $d_A = 3.3\text{x}10^{-4}$ m. Numerical application of C_A on table 2.4 according to capillary length l_1, conductance C_1, pressure p_{GD} and p_M.

2.2.3 Estimation of GDES cell pressure and volumetric-flow

For the GDES cell, the mass-flow conservation at equilibrium gives the following relation:

Confidential

$$Q_1 = Q_A \tag{2.7}$$

leading to:

$$C_1(p_a - p_{GD}) = C_A(p_{GD} - p_M) \tag{2.8}$$

where p_M is the pressure inside the vacuum chamber. The capillary length l_1 is then calculated by:

$$l_1 = \frac{d_1^4}{16\,\eta\,v\,d_A^2}\frac{(p_a + p_{GD})\,(p_a - p_{GD})}{(p_{GD} - p_M)}\ (\mathrm{m}) \tag{2.9}$$

In typical operating conditions, it can be assumed that $p_a \gg p_{GD}$ and $p_{GD} \gg p_M$. The capillary length is then approximated by:

$$l_1 \approx \frac{d_1^4}{16\,\eta\,v\,d_A^2}\frac{p_a^2}{p_{GD}} \tag{2.10}$$

The capillary length l_1 and the capillary conductance C_1 are calculated from equations 2.9 and 2.3, respectively, for the glow discharge cell pressure varying between 40 and 200 Pa and for four values of the vacuum chamber pressure 1.333, $1.333\text{x}10^{-1}$,$1.333\text{x}10^{-2}$ and $1.333\text{x}10^{-3}$ Pa and with $d_1 = 6.3\text{x}10^{-5}$m and $d_A = 3.3\text{x}10^{-4}$ m (table 2.2).

The capillary length and conductance slightly vary according to the vacuum chamber pressure. So, the capillary length can be calculated from the approximated equation 2.10. The conductance of anode orifice C_A, calculated from equation 2.5, is $C_A = 8.18 \times 10^{-6}$ m^3/s.

The length of capillary inlet ranges between $2.6\text{x}10^{-2}$ and $1.3\text{x}10^{-1}$ for GDES cell pressure between 40 and 200 Pa. The continuous inlet flow of ambient air in vacuum chamber is fixed by the lowest conductance, which is the conductance of the capillary inlet C_1, as $1/C_1 + 1/C_A \approx 1/C_1$.

The value of the volumetric-flow entering the vacuum chamber ranges between 3×10^{-9} and 1.8×10^{-8} m^3/s. In order to reduce gas load for the pumping system, capillary inlet flow can be turned off by switching off the valve when mass analysis is stopped.

2.2.4 Choice of capillary length

Taking into account Paschen breakdown curve for air or N_2 (see figure 2.4), six values of capillary length are chosen around Paschen minimum.

The pressure (in Pa) in the GDES cell according to the length of capillary (in m) is estimated (from equation 2.10) by:

$$p_{GD} = \frac{d_1^4\,p_a^2}{16\,\eta\,v\,d_A^2}\frac{1}{l_1} \approx \frac{13.0655}{l_1}\ (\mathrm{Pa}) \tag{2.11}$$

The characterisation of the discharge will be performed for six capillary lengths: $l_1 = 0.500$,

Confidential

p_M (Pa) →	1.333	$1.333\text{x}10^{-1}$	$1.333\text{x}10^{-2}$	$1.333\text{x}10^{-3}$
p_{GD} (Pa) ↓	l_1 (m)			
40.00	0.3391	0.3289	0.3279	32.78
53.33	0.2522	0.2465	0.2459	24.59
66.66	0.2007	0.1971	0.1967	19.67
79.99	0.1667	0.1642	0.1639	16.39
93.33	0.1425	0.1407	0.1405	14.05
106.7	0.1245	0.1231	0.1230	12.29
120.0	0.1105	0.1094	0.1093	10.93
133.3	0.0993	0.09.84	0.09.84	9.84
146.7	0.0902	0.0895	0.0894	8.94
160.0	0.0826	0.0820	0.0820	8.20
173.3	0.0762	0.0757	0.0757	7.57
186.7	0.0708	0.0703	0.0703	7.03
200.0	0.0660	0.0656	0.0656	6.56
p_{GD} (Pa) ↓	C_1 (m^3/s)			
40.00	$3.38\text{x}10^{-9}$	$3.49\text{x}10^{-9}$	$3.50\text{x}10^{-9}$	$3.50\text{x}10^{-9}$
53.33	$4.55\text{x}10^{-9}$	$4.66\text{x}10^{-9}$	$4.67\text{x}10^{-9}$	$4.67\text{x}10^{-9}$
66.66	$5.72\text{x}10^{-9}$	$5.82\text{x}10^{-9}$	$5.83\text{x}10^{-9}$	$5.83\text{x}10^{-9}$
79.99	$6.89\text{x}10^{-9}$	$6.99\text{x}10^{-9}$	$7.00\text{x}10^{-9}$	$7.00\text{x}10^{-9}$
93.33	$8.05\text{x}10^{-9}$	$8.16\text{x}10^{-9}$	$8.17\text{x}10^{-9}$	$8.17\text{x}10^{-9}$
106.7	$9.22\text{x}10^{-9}$	$9.33\text{x}10^{-9}$	$9.34\text{x}10^{-9}$	$9.34\text{x}10^{-9}$
120.0	$1.04\text{x}10^{-8}$	$1.05\text{x}10^{-8}$	$1.05\text{x}10^{-8}$	$1.05\text{x}10^{-8}$
133.3	$1.16\text{x}10^{-8}$	$1.17\text{x}10^{-8}$	$1.17\text{x}10^{-8}$	$1.17\text{x}10^{-8}$
146.7	$1.27\text{x}10^{-8}$	$1.28\text{x}10^{-8}$	$1.28\text{x}10^{-8}$	$1.28\text{x}10^{-8}$
160.0	$1.39\text{x}10^{-8}$	$1.40\text{x}10^{-8}$	$1.40\text{x}10^{-8}$	$1.40\text{x}10^{-8}$
173.3	$1.51\text{x}10^{-8}$	$1.52\text{x}10^{-8}$	$1.52\text{x}10^{-8}$	$1.52\text{x}10^{-8}$
186.7	$1.62\text{x}10^{-8}$	$1.63\text{x}10^{-8}$	$1.64\text{x}10^{-8}$	$1.64\text{x}10^{-8}$
200.0	$1.74\text{x}10^{-8}$	$1.75\text{x}10^{-8}$	$1.75\text{x}10^{-8}$	$1.75\text{x}10^{-8}$

Table 2.2: Length l_1 and conductance C_1 of capillary inlet according to glow discharge cell and vacuum chamber pressures for $d_1 = 6.3\text{x}10^{-5}$ m and $d_A = 3\text{x}10^{-2}$ m.

Confidential

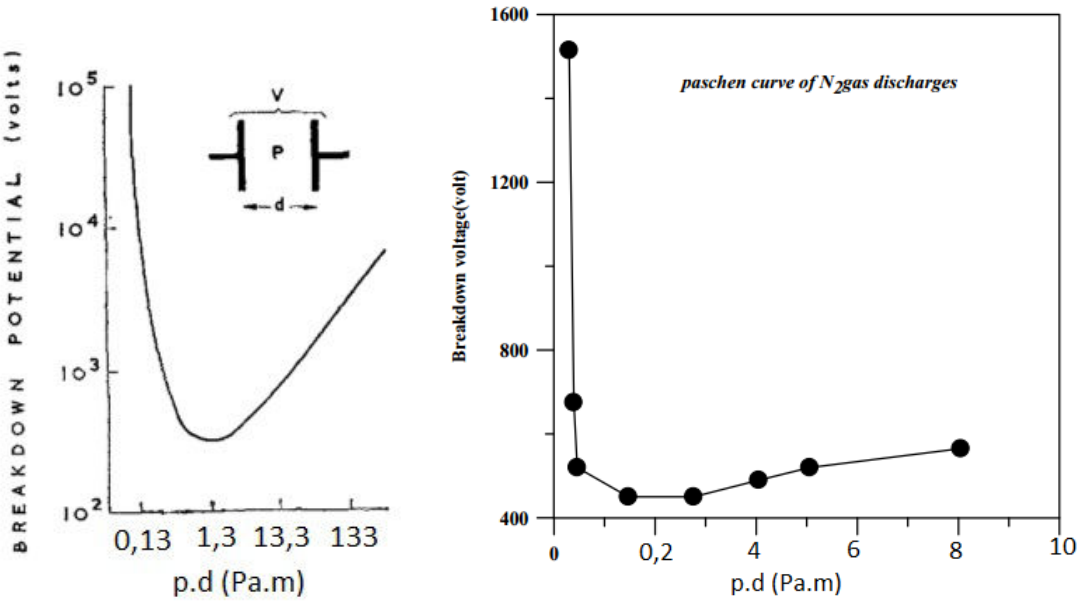

Figure 2.4: Paschen breakdown curve for air (on the left), from [39] with initially pd (mmHg x cm), and for N_2 (on the right), from [57] with initially pd (mbar x cm x 10^{-1}), with plane parallel electrodes.

0.330, 0.200, 0.165, 0.098 and 0.071 m. These lengths lead to values of the product $p_{GD} \times d_{AC}$ located around the Paschen minimum (table 2.3). As we will see, the corresponding (experimental) values are slightly shifted toward lower values.

2.2.5 General throughputs

The mass-flow conservation at equilibrium gives the following relation:

$$Q_1 = Q_A = Q_T = S_{Tef} p_M \qquad (\mathrm{Pa} \times \mathrm{m}^3/\mathrm{s}) \tag{2.12}$$

with Q_1 the capillary mass-flow, Q_A the anode-orifice mass-flow, Q_T and S_{Tef} the throughput and effective pumping speed of the turbo-molecular pump, respectively.

The vacuum chamber pressure is measured according to five lengths of capillary and when the quarter-turn valve is closed. The nominal speed of the turbo molecular pump is equal to 0.25 m^3/s. As the pump is connected to the chamber *via* a 0.25 m^3/s, $S_{T,ef} = 0.125$ m^3/s. The throughput of the turbo molecular pump is calculated from

$$Q_T = S_{T,ef}\, p_M$$

with measured values of p_M (table 2.4). The anode orifice is calculated from: $C_A = C_1\, p_a / p_{GD}$.

Q_T is slightly higher than Q_1 due to a lower value of the effective pumping speed at the anode orifice. When the valve is closed, the value of Q_T represents the throughput of the residual leak

l_1 (m)	p_{GD} (Pa)	$p_{GD} \times d_{AC}$ (Pa x m)
0.071	183.98	12.142
0.098	133.80	8.8308
0.165	79.473	5.2452
0.200	65.555	4.3266
0.330	39.730	2.6221
0.500	26.225	1.7308

Table 2.3: Estimated pressure in GDES cell for six values of capillary length around Paschen minimum.

l_1 (m)	C_1 (m^3/s)	$Q_1 = Q_A$ ($Pa \times m^3/s$)	p_{GD} (Pa)	C_A (m^3/s)	p_M (measured) (Pa)	Q_T ($Pa \times m^3/s$)
0.071	$1.49x10^{-8}$	$2.74x10^{-6}$	183.98	$8.18x10^{-6}$	$1.30x10^{-2}$	$1.63x10^{-3}$
0.098	$1.08x10^{-8}$	$1.45x10^{-6}$	133.802	$8.18x10^{-6}$	$9.59x10^{-3}$	$1.20x10^{-3}$
0.165	$6.42x10^{-9}$	$5.10x10^{-7}$	79.4734	$8.18x10^{-6}$	$5.86x10^{-3}$	$7.33x10^{-3}$
0.200	$5.29x10^{-9}$	$2.64x10^{-7}$	65.5546	$8.18x10^{-6}$	$4.66x10^{-3}$	$5.83x10^{-4}$
0.330	$3.21x10^{-9}$	$9.69x10^{-8}$	39.730	$8.18x10^{-6}$	$2.80x10^{-3}$	$3.50x10^{-4}$
0.500			26.2245	$8.18x10^{-6}$		
closed	0	0	p_M	0	$1.57x10^{-4}$	$1.96x10^{-5}$

Table 2.4: Calculation of C_1 the capillary conductance, Q_1 the mass-flow in the capillary, p_{GD} the GDES cell pressure, C_A the anode orifice conductance, and Q_T the throughput of the turbo molecular pump from the measured pressures in the vacuum chamber, in relation with l_1, the capillary length.

and degassing of the vacuum system.

Confidential

2.3 Electric system

2.3.1 Power supplies and measurement devices

A power DC supply is needed to sustain the plasma discharge in glow regime. Another power DC supply is used to polarize the electron collection plate to attract or repulse the electrons (figure 2.1).

The discharge sustaining power supply is a floating adjustable DC supply with active current limiting capability, which is connected in series between the anode and cathode electrodes. The voltage across the anode and cathode is denoted as V_{AC}. The discharge current at the anode and cathode electrodes, denoted as I_C and I_A respectively, are measured by means of an ammeter.

The DC polarization voltage supply is floating and adjustable. The polarization voltage, denoted as V_{PA}, is applied between the plate and anode. The electron current at the collection plate I_P is

measured by another ammeter, at $\pm 10^{-8}$ A.

The undesired discharge current I'_d passing by vacuum chamber walls is limited by resistance R, when undesired discharges are in an unstable regime. It is then reduced and measurements can be performed in larger ranges of voltages.

2.3.2 Origin of measured currents

An electrical consideration (electron flow) permits decoupling of currents, while the current balance equation is maintained in the system. This balance equation for the measured currents is expressed as:

$$I_C = I_A + I_P + I'_d \tag{2.13}$$

We defined the origin of the measured currents taking into account that the external side of the anode electrode is conductive. The (main) discharge current (between anode and cathode) is denoted as I_d.

Initially it is assumed that the solely source of electrons (without creation of secondary electrons) between the anode and plate is the electrons exiting anode orifice. This electron current is denoted as I_b. A part of these electrons reaches the plate inducing the current $I_{b,P}$, while the other part goes back toward the external side of anode inducing the current $I_{b,A}$, such as $I_b = I_{b,A} + I_{b,P}$ is constant. The values of $I_{b,P}$ and $I_{b,A}$ depend on the potential applied between the plate and anode, and on the kinetic energy of electrons at anode orifice. The cathode current is the total current. The measured currents in the system are expressed from:

$$\begin{aligned} I_C &= I_d + I_{b,A} + I_{b,P} + I'_d \\ I_A &= I_d + I_{b,A} \\ I_P &= I_{b,P} \end{aligned} \tag{2.14}$$

Besides, a possible creation of secondary electrons at the anode aperture source is taken into account. It is an additional current source between the anode and the plate. The secondary electron current is denoted as I_s, with the part of the secondary electrons reaching the plate inducing the current $I_{s,P}$, while the other part reaching the anode inducing the current $I_{s,A}$. The measured currents in the system are then expressed from:

$$\begin{aligned} I_C &= I_d + I_{b,A} + I_{b,P} + I'_d \\ I_A &= I_d + I_{b,A} - I_{s,A} \\ I_P &= I_{b,P} + I_{s,A} \end{aligned} \tag{2.15}$$

Confidential

The undesired discharge current I'_d is induced by a leakage of electron at the insulator fitting, other possible sources have been tested giving zero current. This fitting maintains the 1/4" stainless steal tubes at a distance of $5\text{x}10^{-3}$ m. According to the capillary length, *i.e.* the pressure of the flowing gas in this fitting, and the value of the discharge sustaining power supply, a weak discharge can occurs.

2.3.3 Determination of kinetic energy

If the only source of electrons is the anode orifice, the estimation of the electron current intensity and of the distribution of kinetic energy of electrons at the anode orifice can be deduced from the measure of the plate current *versus* the potential applied between the plate and anode.

A part of electrons can reach the plate according to the principle of the energy conservation between the anode and plate, whatever the trajectory path:

$$E_{k,A} + E_{p,A} = E_{k,P} + E_{p,P} \tag{2.16}$$

where $E_{k,A}$ and $E_{p,A}$ are the electron kinetic energies and potential energies, respectively, at the anode, and $E_{k,P}$ and $E_{p,P}$ are the electron kinetic energies and potential energies, respectively, at the plate.

Without secondary electrons, the distribution of electron kinetic energy at the anode orifice is denoted as $f_e(E_{k,A})$. The current I_P is in proportion to the integral value of the kinetic energy distribution for values of $E_{k,A}$ ranging between qV_{PA} and $E_{k,A,max}$ according to:

$$I_P(V_{PA}) \propto \int_{qV_{PA}}^{E_{k,A,max}} f_e(E_{k,A}) dE_{k,A} \tag{2.17}$$

where $q = -1$ is the charge of electron so that qV_{PA} have dimension of energy in eV and $E_{k,A,max}$ is the maximum value of the kinetic energy distribution.

If it is assumed that the distribution $f_e(E_{k,A})$ is uniform, the current is zero for negative values of V_{PA} then it increases from $V_{PA} = E_{k,A,max}/q$ until 0. For the positive values, I_P is constant (see curve (a) of figure 2.5). Two adjacent uniform distributions with more electrons at low or at high energies give a dual-slope increase (see curve (b) of figure 2.5). Two separated uniform distributions lead to a plateau between two linear increases (curve (c) of figure 2.5). The figures 2.15 and 2.16 show experimental results of electron kinetic energy distributions at the anode orifice.

2.4 Characterisation of glow discharge

2.4.1 Paschen curve

The breakdown occurs when the voltage across the electrodes suddenly drops, followed by an increase in the discharge current. The experimental points of the Paschen curve are obtained by

Confidential

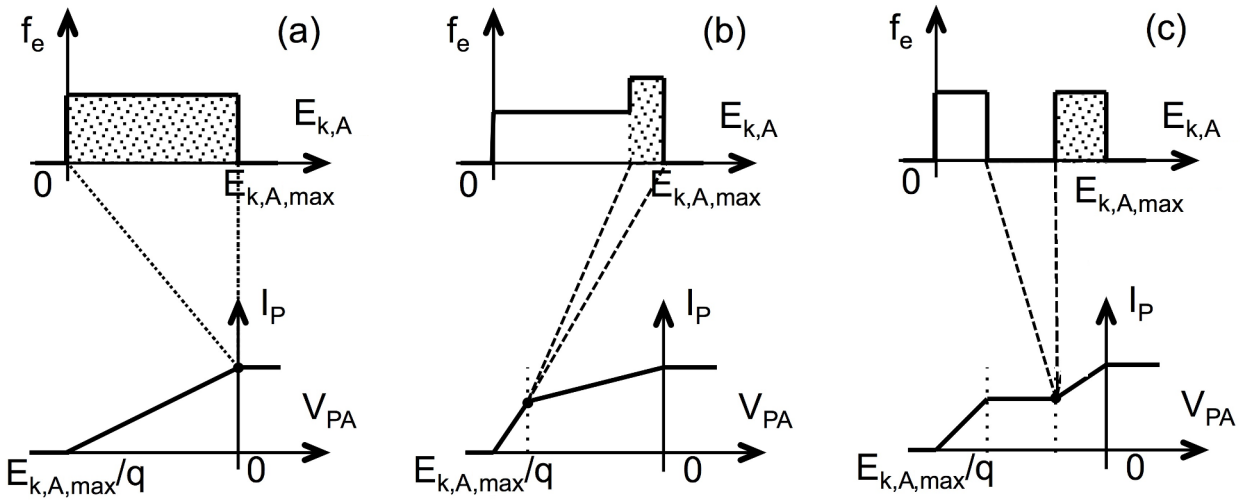

Figure 2.5: (Top) Electron kinetic energy distribution and (bottom) plate current obtained *versus* potential applied between the plate and anode for (a) a uniform distribution, (b) two adjacent uniform distributions with more electrons at higher energies and (c) two separate uniform distributions.

plotting the breakdown voltage V_b *versus* pressure-distance product $p_{GD} \times d_{AC}$ for different values of the pressure in the GDES by means of six capillary lengths $l_1 = 0.50$, 0.33, 0.20, 0.165, 0.098 and 0.071 m (figure 2.6). $p_{GD} \times d_{AC}$ is estimated from equation 2.11. Each point of the curve is the mean value of 10 successive measurements. And the error bar is ± 3 standard deviations.

The experimental curve shape fits a Paschen's curve (see figure 2.4). The experimental curve is slightly shifted on the left. The pressure estimation from the above equation leads to 1.5 times lower pressure values and the discharge occurs at higher values of potential. That could be due to the fact that the gas flow in the GDES cell and the pressure could be higher in the centre of the cell.

The other insulator materials and inner diameters lead to similar breakdown voltage values.

In order to have the lowest voltage values (for a lighter Electronic Control Unit), we chose to operate at the Paschen minimum, *i.e.* for capillary length equal to 0.165 m.

2.4.2 Voltage-Current characteristic

Three main parameters characterise the discharge: voltage, current and pressure [58]. Additional parameters can influence the discharge: an existing gas-flow [59], the temperature of the source and the nature of the gas and electrodes. Also wall losses for constricted discharge can change the voltage-current characteristic [60]. The voltage-current characteristic is established to check the regimes of the discharge due to the use of inlet gas flow of air, a multi-compound gas having different discharge characteristics if they are used separately.

The experimental protocol is as follows: gas flow enters into the GDES cell by means of different capillary lengths to have different pressures. The experimental data was taken starting from breakdown voltage to the glow discharge region until 10^{-2} A.

Confidential

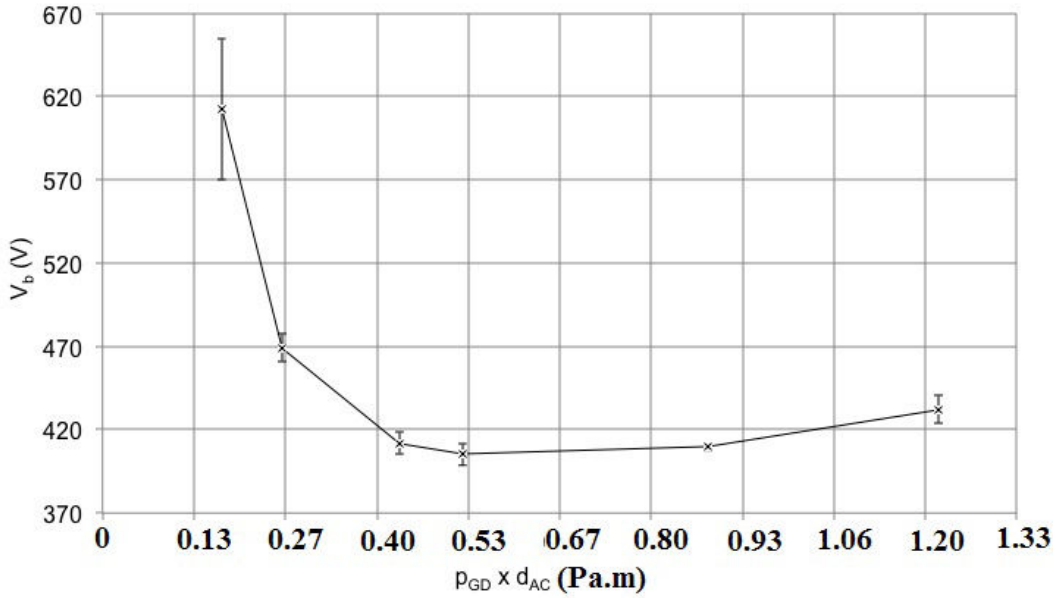

Figure 2.6: Experimental Paschen curve for N10 GDES cell with ambient airflow inlet. From left to right, the capillary lengths are: $l_1 = 0.500$, 0.330, 0.200, 0.165, 0.098 and 0.071 m. The error bar is $\pm$ 3 standard deviations around the mean value calculated from 10 measured values.

After breakdown, in glow discharge regime, one can observe that both the discharge current and discharge potential linearly increase (figure 2.7). Voltage slightly increases with current for the highest pressures (l_1 = 0.071 and 0.098 m). For the lowest values of the pressure, the potential increases with current as in an abnormal glow discharge regime. Reducing the inner diameter of the discharge increases the slope of the characteristics.

Several papers describe this behaviour for a normal glow discharge regime [35, 57, 58, 61]. The V-I characteristics established (not horizontal lines), show that the GDES cell operates in the abnormal regime. Different plasma electrical resistances can explain the different slopes of each approximately linear curve.

There are benefits to having greater slopes for discharge stability, as a small variation of the voltage will induce a small variation of the current. The capillary length l_1 = 0.165 m and a reduced inner diameter of the GDES cell is suitable to attain a stationary current with lower values to reduce the electrical consumption.

2.4.3 Time-dependence of the discharge current

The time dependence of the discharge current was investigated to choose the material and inner diameter of the insulator. The evolution of the cathode current is measured over a period of 240-300 min for the three inner diameters and the four insulator materials in figure 2.8.

Similar cathode current value evolutions were observed for the Macor and Nylon for the three

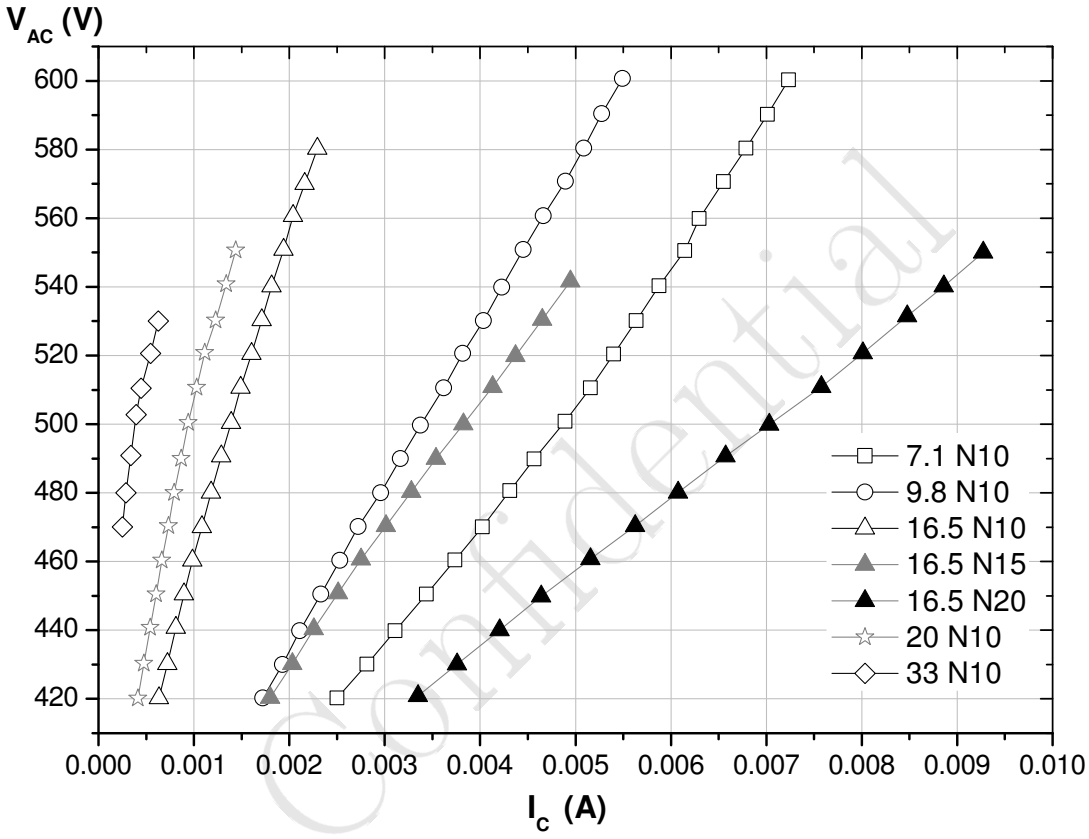

Confidential

Figure 2.7: V-I characteristics of discharge after breakdown. Influence of the inner diameter of the insulator is shown for N10, N15 and N20 GDES cells and capillary lengths: 0.33, 0.2, 0.165, 0.098 and 0.071 m.

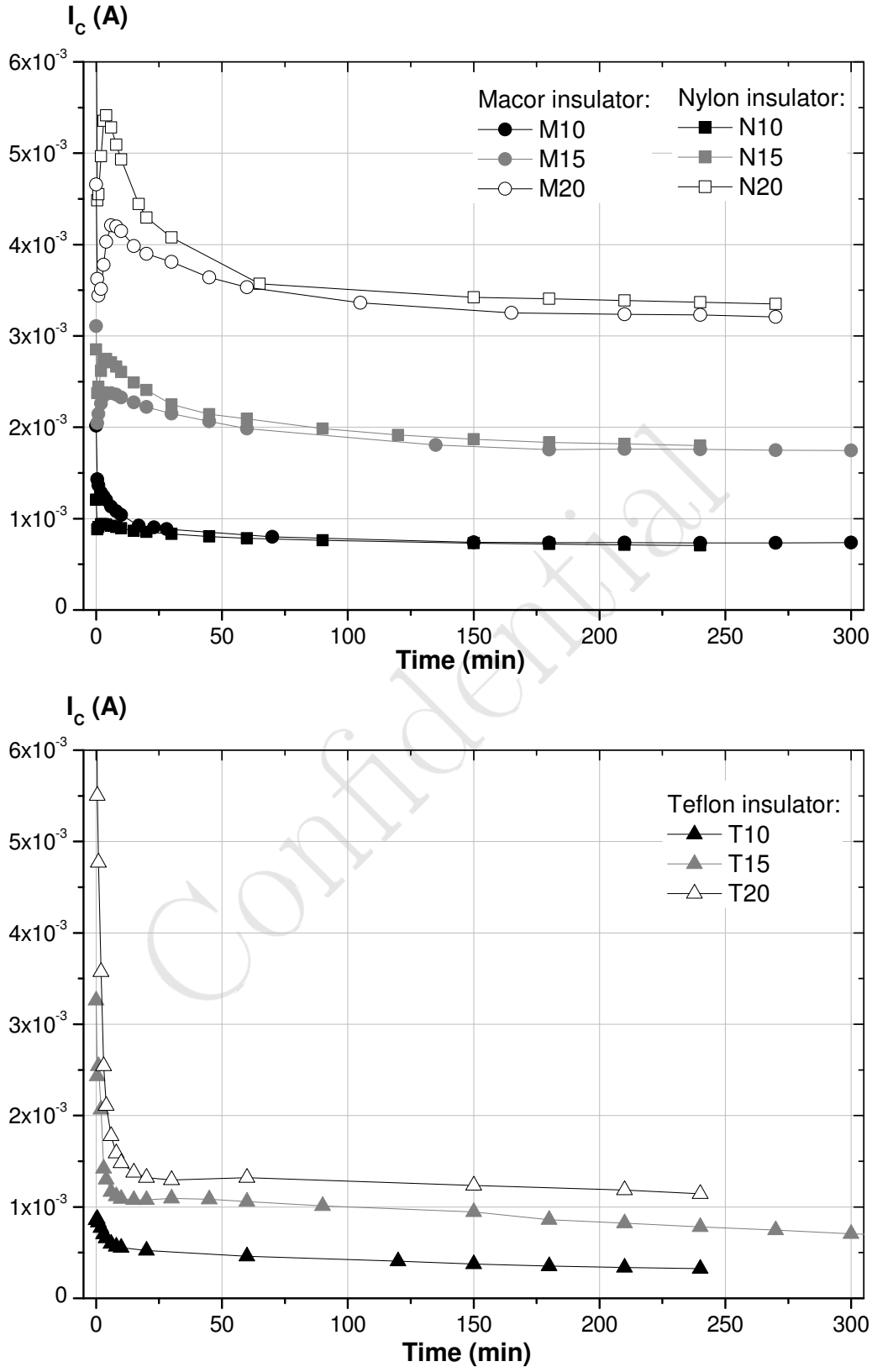

Confidential

Figure 2.8: Time dependence of the cathode current at a discharge voltage of 420 V with capillary 0.165 m, for different material and diameter insulator: (circle Macor, (square) nylon, (triangle) Teflon, and (black) 10^{-2}, (grey) 1.5x10^{-2} and (white) 2x10^{-2} m.

diameters. Obviously, with larger diameters, the discharge occupies a larger volume and the cathode current is higher. A steady discharge (cathode) current is obtained after 60-120 min running with the cells in Macor and Nylon.

For the three diameters of Teflon insulator, the cathode current values are lower than those obtained with Nylon and Macor. However, the cathode current always decreases during time and particular strong discharge instabilities are observed after a run of about 600 min.

Also, for Pyrex insulator the cathode current never attains a plateau.

The best stable glow discharge regime and the lowest power consumption are achieved for a M10 or N10 insulator (see table 2.1). As a consequence, the N10 GDES cell was used in the following sections.

2.4.4 Characterization of the deposits

The phenomenon of sputtering occurs in the GDES cell as the formation of a deposit (thin film layers) at anode has been observed even when operating the GDES cell over several minutes in typical operating conditions.

Figure 2.9 shows different deposits on the anode, cathode and insulator obtained for different insulator materials and under different gas flows.

With Teflon and airflow, was observed a deposit on the anode and on the half-part of the insulator close to the cathode. With the ceramic coating, the deposit takes place over the whole surface of the cylinder. On the teflon insulator, no deposit is observed with the air flow, while a slight deposit is formed with the argon and nitrogen flows. Upon the anode, the most significant deposit is observed with air and nitrogen flows.

Confidential

The examination of the anode deposit by Scanning Electron Microscopy (SEM) combined with Energy Dispersive Xray spectroscopy (EDX) gives, respectively, the surface topography, and the elementary composition of the deposit merely.

An example of layers on the anode around the aperture observed by SEM is shown in figure 2.10. SEM reveals a ring-shaped deposit around the anode aperture thicker than elsewhere.

The Energy Dispersive Xray spectroscopy of the thickest deposit gives the elements sputtered from stainless steel cathode, *i.e.* Fe, Cr and Ni (figure 2.10). Additional elements are measured with the Teflon insulator: Fluorine (45%), from Teflon, and O (8%), from air; and with the Nylon insulator: O (20%), from Nylon and air.

In addition, this deposit has been measured as electrically resistive. It seems to be less resistive when using Nylon than when using Teflon. The resistivity of the thin film increases with the increase of oxygen.

A temporal modification of the resistivity of the deposit affects the V-I characteristic of the discharge.

Figure 2.9: Picture of deposits for different insulator materials and under different gas flows. From left to right: Cathode; insulator; anode after a run of six hours. 1^{st} raw: Air flow and Nylon; 2^{nd} raw: Air flow and Nylon with silica gel ceramic coating; 3^{rd} raw: Air flow and Teflon; 4^{th} raw: Argon flow and Teflon; 5^{th} raw: Nitrogen flow and Teflon.

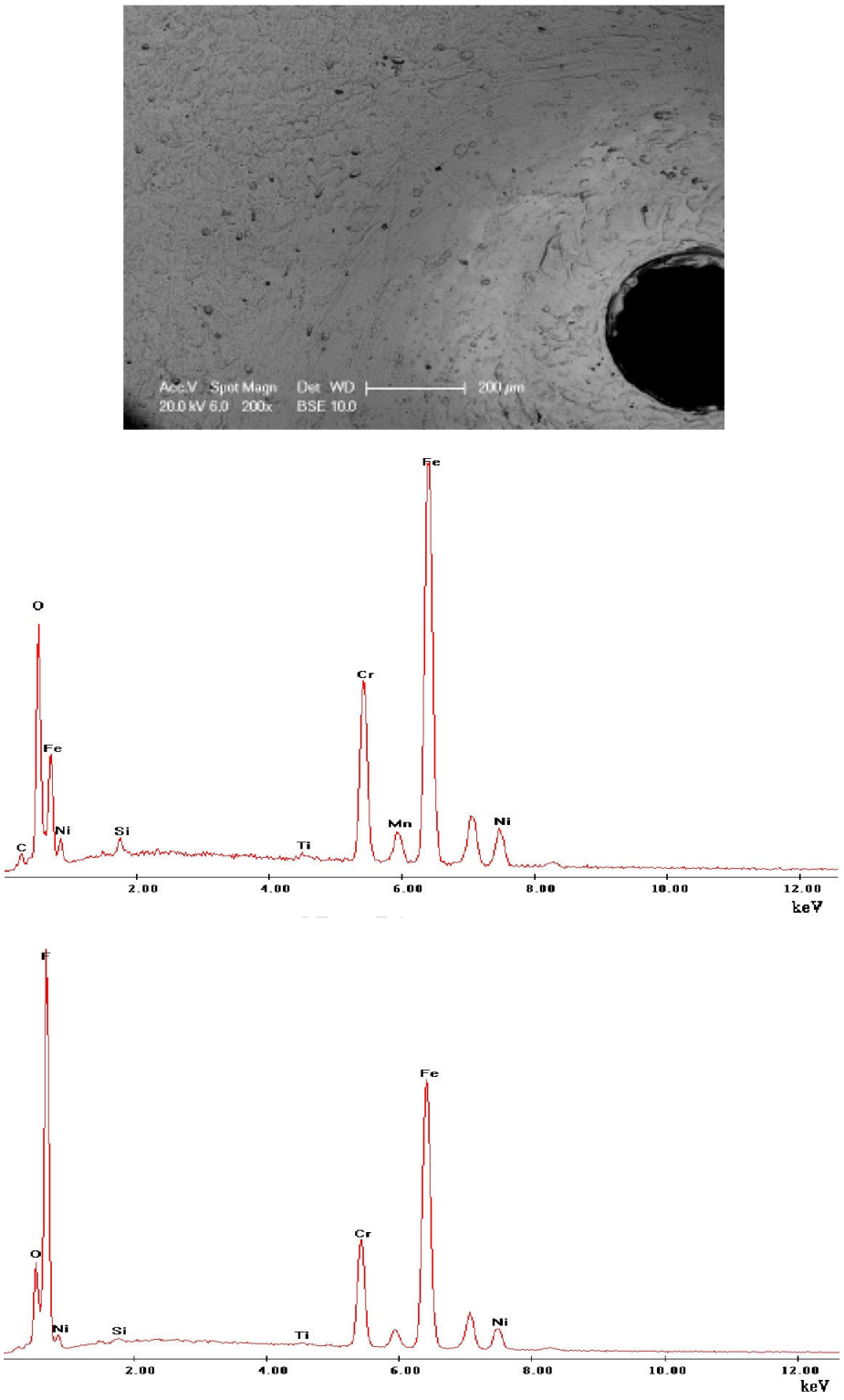

Figure 2.10: Scanning Electron Microscopy picture of the deposit on the anode close to the aperture (Top) . Energy Dispersive Xray spectrum of elements of the thickest deposit on the anode electrode in the vicinity of the aperture for Nylon (Middle) and Teflon (Bottom) insulator.

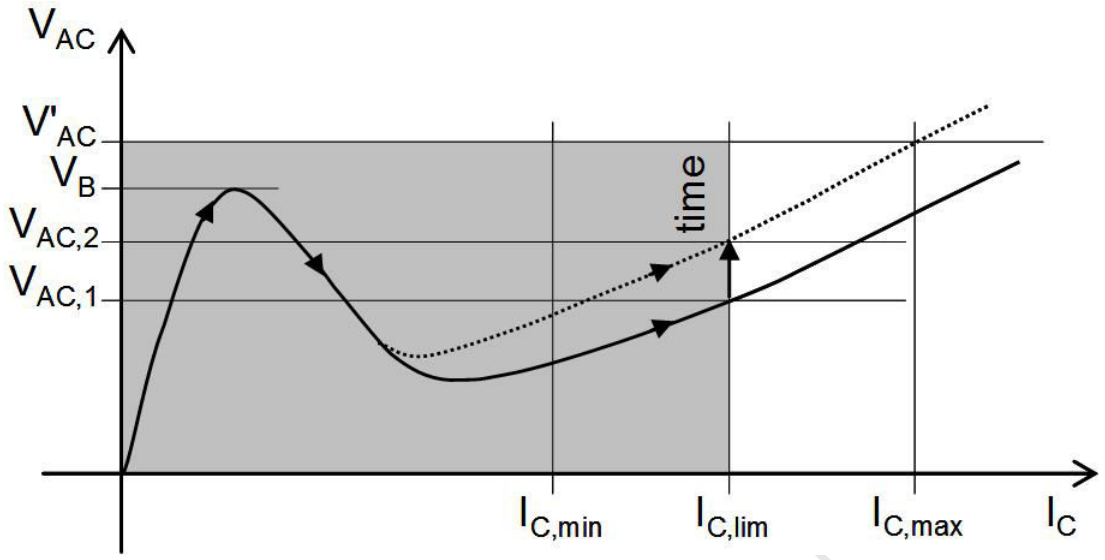

Figure 2.11: V-I characteristic of the discharge and main potential and current values used to operate the cell in glow regime with stabilisation.

Confidential

2.5 Principle to operate the discharge with stabilisation

2.5.1 Principle

The previous experimental results have been recorded with the current delivered by the discharge sustaining power supply limited at 10^{-2} A and V_{AC} chosen to optimise the operating point of the discharge. The discharge current, I_C, decreases continously due to deposits on the anode electrode. However, the discharge current must be stable.

The DC value applied between the cathode and anode V'_{AC} must be chosen higher than voltage breakdown, V_B: $V'_{AC} \geq V_B$, in order to be able to start the discharge (figure 2.11). In the experiment, V_B is measured to be equal to 410 V. In this case therefore, V'_{AC} is chosen equal to 450 V. As the discharge tends to increase the current, the current delivered by the power supply is limited to a value denoted as $I_{C,lim}$. So, the supply adapts to the operating potential. Current and potential of the supply will evolve within the grey area (see figure 2.11).

The V-I characteristic of the cell changes on the time. The full line (figure 2.11) represents the V-I characteristic when the cell is new (without deposits on anode) at t=0. At the beginning, the V-I characteristic changes quickly, then a stabilisation occurs after some hours (about 4h) and the V-I characteristic tends toward a limit represented by the dashed line (figure 2.11). As the current is limited to $I_{C,lim}$, its value is almost constant and the potential applied to the cell varies from $V_{AC,1}$ to $V_{AC,2}$. As a consequence, the discharge currents are stabilised using current limitation of the power supply.

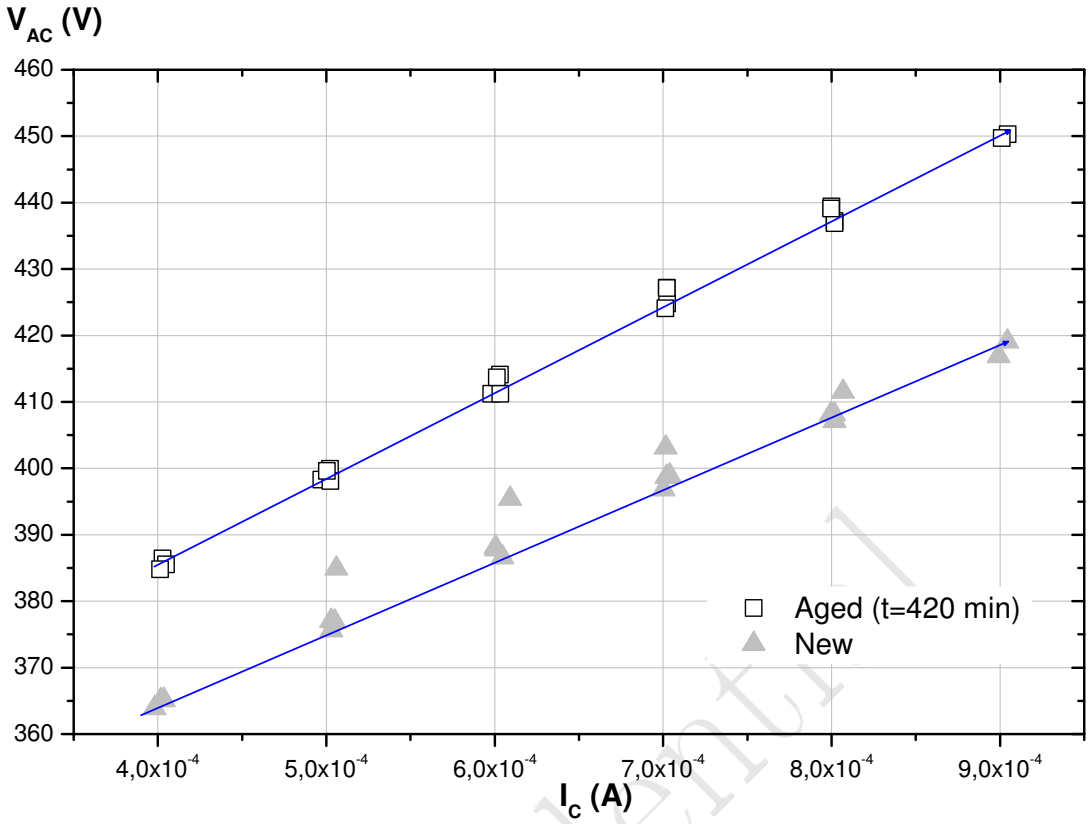

Figure 2.12: V-I characteristic of the discharge for a new and aged cell with current limitation of the power supply with N10 GDES cell (each I/V couple is measured 4 times).

2.5.2 Temporal evolution of V-I characteristic

In order to obtain the V-I characteristic of the discharge, the current limitation of the discharge sustaining power supply is varied by steps of 10^{-4} A. In figure 2.12, the V-I characteristic is plotted for a clean cell at $t = 0$ (New) and after 420 min running (Aged) *versus* six different values of the current. Each current value is measured four times by varying the current from $4\text{x}10^{-4}$ to $9\text{x}10^{-4}$ A then to $9\text{x}10^{-4}$ to $4\text{x}10^{-4}$ A, twice (each (V, I) couple is measured 4 times). The duration is about 10 min. The potential of the discharge sustaining power supply is limited to 450 V. There is a difference of about 20-30 V between the new and aged cells. The current remains constant, while the voltage changes. The measured values of the current and potential are reproducible.

2.5.3 Temporal stabilisation of discharge current

The discharge potential and the current limitation of the discharge sustaining power supply are 450 V and $4\text{x}10^{-4}$ A, respectively. The evolution of the discharge characteristic *versus* time over a period of 300 min is plotted in figure 2.13. The potential varies from 363 to 375 V (3.2%), while the current varies from $4.04\text{x}10^{-4}$ to $4.025\text{x}10^{-4}$ A (0.35%). The characteristic of the discharge changes

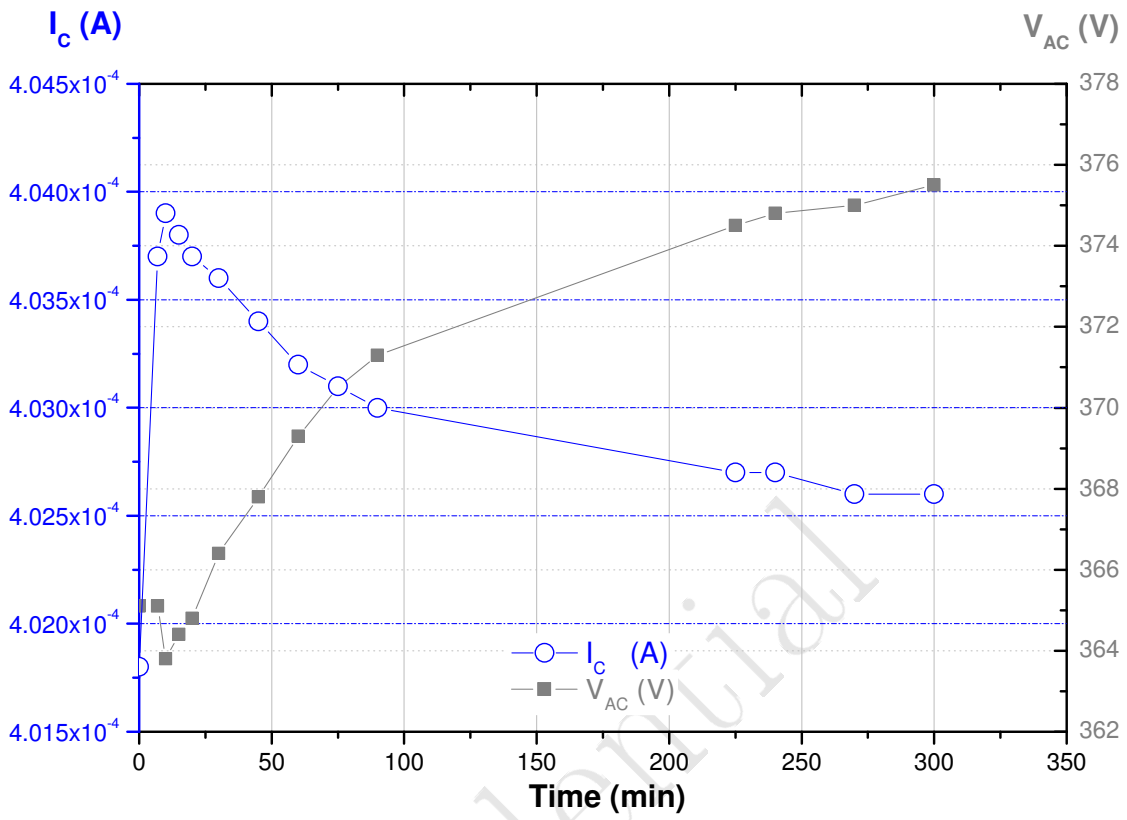

Figure 2.13: Evolution of the voltage and current of the discharge *versus* time with current limitation of the power supply and N10 GDES cell (each I/V couple is measured 4 times).

as V_{AC} varies over a 12 V range. However, the discharge current can be assumed constant with a decreasing only over a $1.5\text{x}10^{-4}$ A range.

Besides, in the case of a longer lifetime study, the discharge is turned on six successive days during 240-360 min and turned off during the night (gas inlet, power supply and pumping device are turned off) (figure 2.12). The discharge current is reproducible and varies over a $2\text{x}10^{-6}$ A range at $8.5\text{x}10^{-4}$ A. The available electron current measured by the plate at $V_{PA} = 0$ V is assumed stable at $2\text{x}10^{-5}$ A, 5 min after the discharge is started.

2.6 Characterisation of the electron beam

2.6.1 Electron kinetic energy distribution in the discharge

The potential is not linearly distributed inside the GDES cell. Due to the small cathode-anode distance, typically it exists the cathode fall, negative glow plasma and anode sheath regions merely [62, 35]. The cold cathode discharge works in abnormal regime confirmed by the shape of the current voltage characteristics of figure 2.7.

Confidential

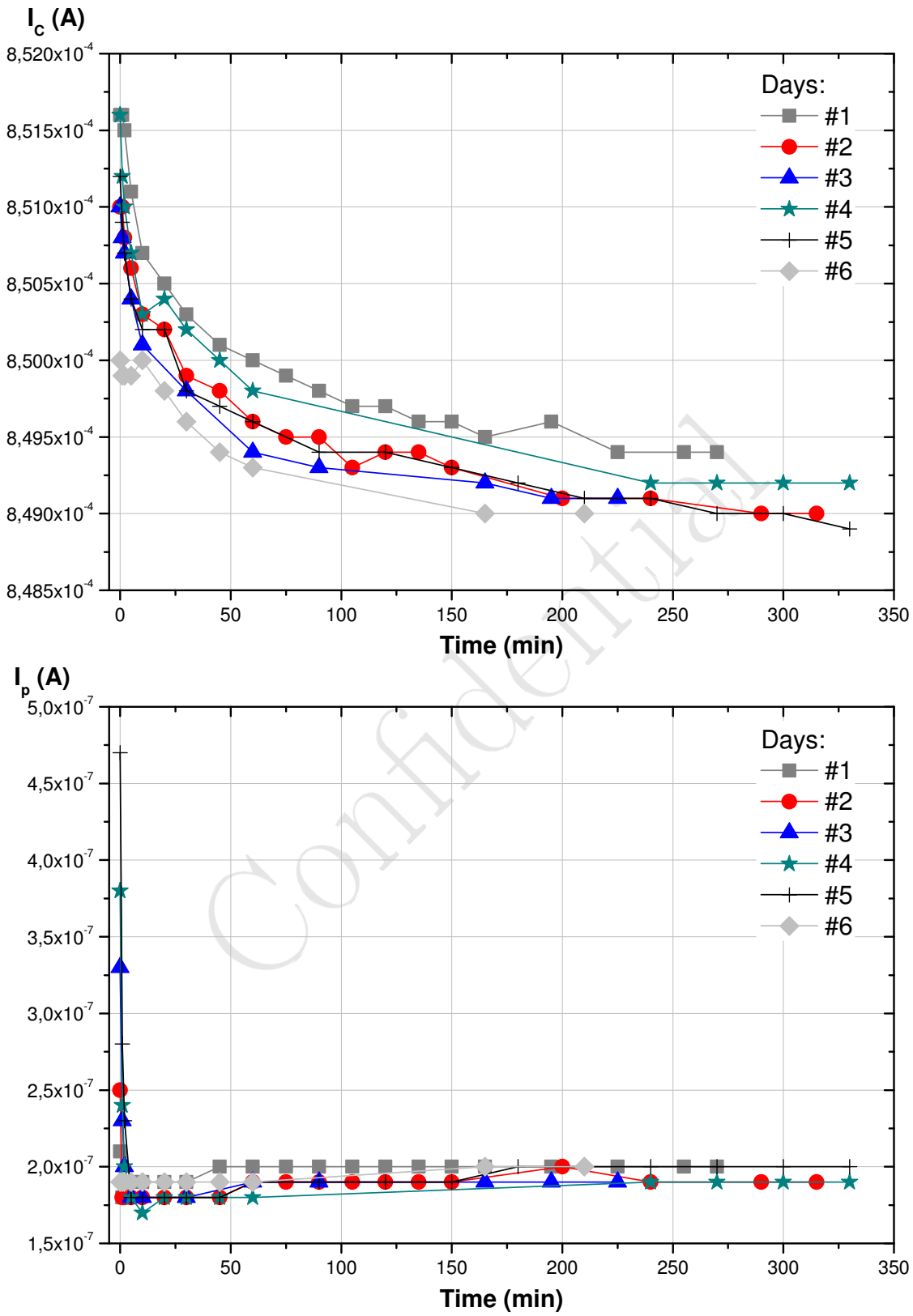

Confidential

Figure 2.14: Evolution of the voltage and current of the discharge *versus* time with current limitation of the power supply with N10 GDES cell.

The cathode fall region is close to the cathode with the largest potential difference, while the negative glow plasma region takes up the largest part of the cell with a quasi-constant positive potential. The electrons are violently accelerated by the strong electric field into the plasma where they lose kinetic energy through inelastic collisions with neutrals and ions.

The anode sheath region has a short distance where the potential plasma returns to zero, the potential typically applied to the anode. The electrons are repelled in this region. However, the voltage drop in the anode sheath is small, so electrons with enough energy can cross the sheath loosing kinetic energy and then a fraction of them passes through the anode aperture. There is a complicated electron energy distribution function in a negative glow plasma not easy to determine [63].

2.6.2 Electron kinetic energy distribution in the beam

The current measured at electron collection plate corresponds to the available electron current for further ionization.

The variation of the plate current *versus* the potential applied between the plate and anode is plotted in figure 2.15 for different values of the DC potential V_{AC} applied between the anode and cathode to sustain the discharge.

The plate current increases with the potential applied between the anode and cathode, as the discharge current.

As the shape of the curves shows an increase of the plate current for positive values of the potential applied between the plate and anode, another source of electrons exists between the anode aperture and plate (see the curve given in figure 2.5 without secondary electrons). That is confirmed by the difference of increase between I_C and I_P measured currents for a same range of V_{AC}. For an increase of V_{AC} from 400 to 545 V, I_C increases of 3.1 times while I_P increases of 4.75 times. Due to gas effusion at the anode aperture, the local pressure is high enough to take into account an additional source of secondary electrons outside the cell close to the anode aperture, according to the kinetic energy of the primary electrons exiting from the anode aperture.

In figure 2.15, for the negative values of V_{PA} until about -10 V, no electrons are detected by the plate. The primary electrons have kinetic energies lower than 10 eV and are collected by the outside conductive surface of the anode leading to $I_P = 0$. For positive values of the potential applied between the plate and anode, the plate current continues to grow in order to achieve a plateau from $V_{PA} =$ 20-30 V until 200 V, the maximal measured value, not shown in figure 2.15. That can be interpreted: no secondary electrons can reach the anode over this potential value, leading to assume that secondary electron kinetic energy is lower than 20-30 eV.

Moreover, the two insulator materials tested (Macor and Nylon) give the same results (figure 2.16). A cell with larger inner diameter does not increase significantly the plate current.

Confidential

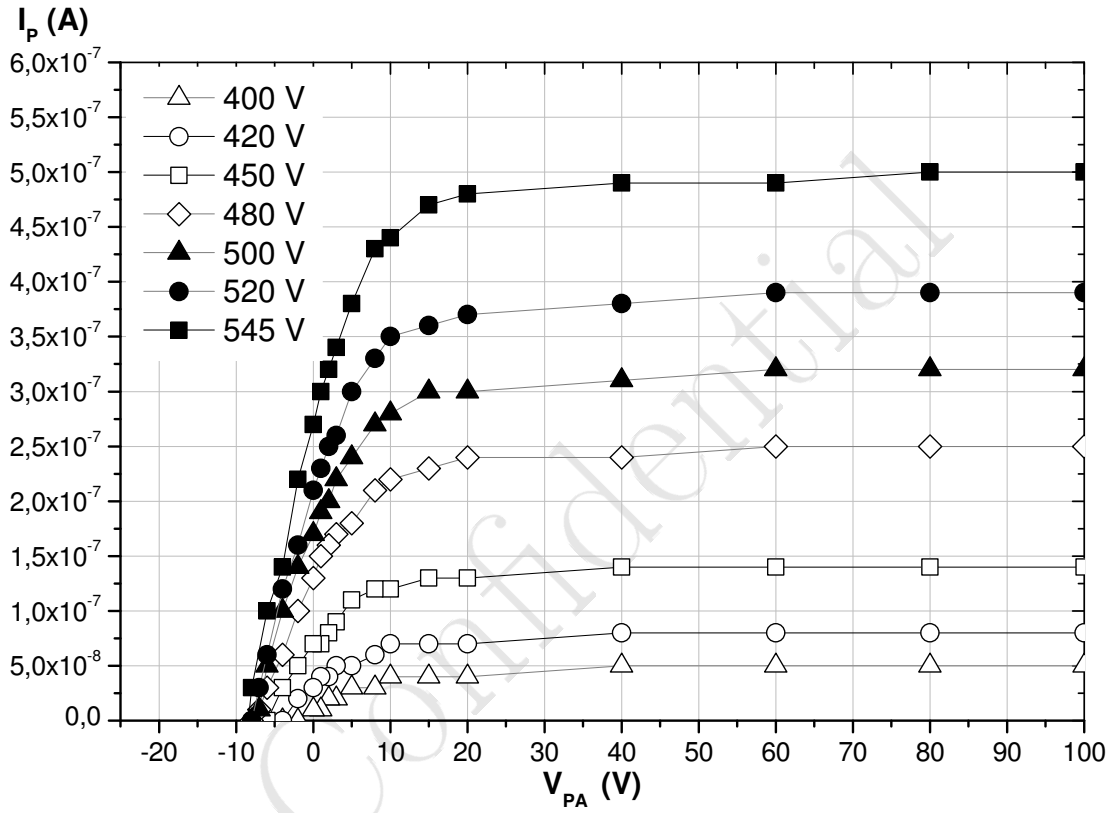

Confidential

Figure 2.15: (Top) Plate current *versus* potential applied between the plate and anode for V_{AC} = 400 (triangle), 420 (bullet), 450 (square), 480 (diamond), 500 (black triangle), 520 (black bullet) and 535 V (black square). The operating conditions are: N10 GDES cell and capillary length = 0.165 m.

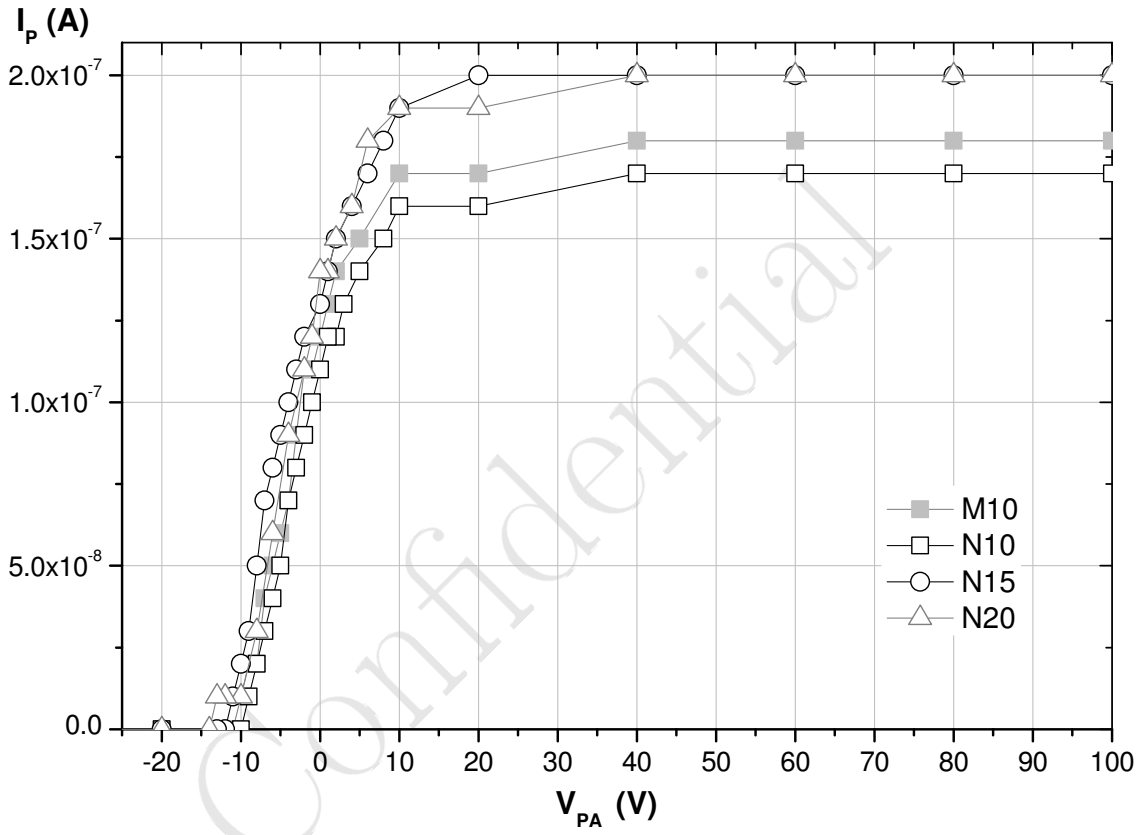

Confidential

Figure 2.16: Plate current *versus* potential applied between the plate and anode for Macor with inner diameter = 10^{-2} m (grey-square), nylon with inner diameter = 10^{-2} m (square), nylon with inner diameter = 1.5x10^{-2} m (circle) and nylon with inner diameter = 2x10^{-2} m (triangle). The operating conditions are: N10 GDES cell, $V_{AC} = 420$ V, $I_C = 7\text{x}10^{-4}$ A and $l_1 = 0.165$ m.

V_{AC} (V)	I_C (A)	I_P (A)	P_{AC} (W)	I_P/P_{AC} **(A/W)**
382.4	4.016x10^{-3}	1.4x10^{-5}	0.15	2.1x10^{-6}
396.2	5.027x10^{-3}	1.6x10^{-5}	0.20	3.2x10^{-6}
410.2	6.037x10^{-3}	1.9x10^{-5}	0.25	4.75x10^{-6}
423.5	7.009x10^{-3}	2.2x10^{-5}	0.30	6.60x10^{-6}
436.7	8.020x10^{-3}	2.6x10^{-5}	0.35	9.1x10^{-6}
449.5	9.027x10^{-3}	2.9x10^{-5}	0.41	1.19x10^{-5}

Table 2.5: Some operating points on the V-I characteristic of the GDES cell, corresponding emitted-electron current intensity, power consumption and efficiency for $V_{PA} = 40$ V for an aged N10 GDES cell.

2.6.3 Electron current intensity, power consumption and emission efficiency

The emitted electrons will be used to ionise neutrals at 70 eV. They have kinetic energies ranging in a few tens of eV at the anode. So, they must always be accelerated by a positive potential, at least 40 V, under similar geometric and potential configuration (as we will see in the next chapter). As a result, the maximal intensity of electron current available can be read from the asymptotic value of the positive voltages in figure 2.15, for $V_{PA} \geq 40$ V.

The available electron current can be increased using higher discharge sustaining voltages (figure 2.15).

In table 2.5, the intensity of the emitted electron current is measured, and the power consumption and electron beam efficiency are calculated for different V-I operating points of the discharge at $V_{PA} = 40$ V. The power consumption is calculated from: $P_{PA} = V_{PA}\, I_C$, and the electron beam efficiency from: I_P/P_{PA}. These values of the electron current intensity *versus* power consumption and of electron beam efficiency *versus* electron current intensity are plotted in figure 2.17.

For $V_{AC} = 450$ V, the emitted electron current $I_P = 4\text{x}10^{-7}$ A and the electron beam efficiency is higher than $7\text{x}10^{-7}$A per W. The electron beam efficiency slightly diminishes, while the electron current intensity increases.

2.6.4 Stability and reproducibility of measured currents

The potential applied between the anode and the plate is varied. The cathode, anode and plate currents are recorded simultaneously for each value of the potential. The potential varies from + 200 to -200 V, then from – 200 to + 200 V, and finally from + 200 to - 200 V. The measurement duration is about 15 min. The limit of the resolution of the ammeter is 10^{-7} A when measuring the cathode and anode currents, and 10^{-8} A the plate current. The experimental results are shown in figure 2.18.

confidential

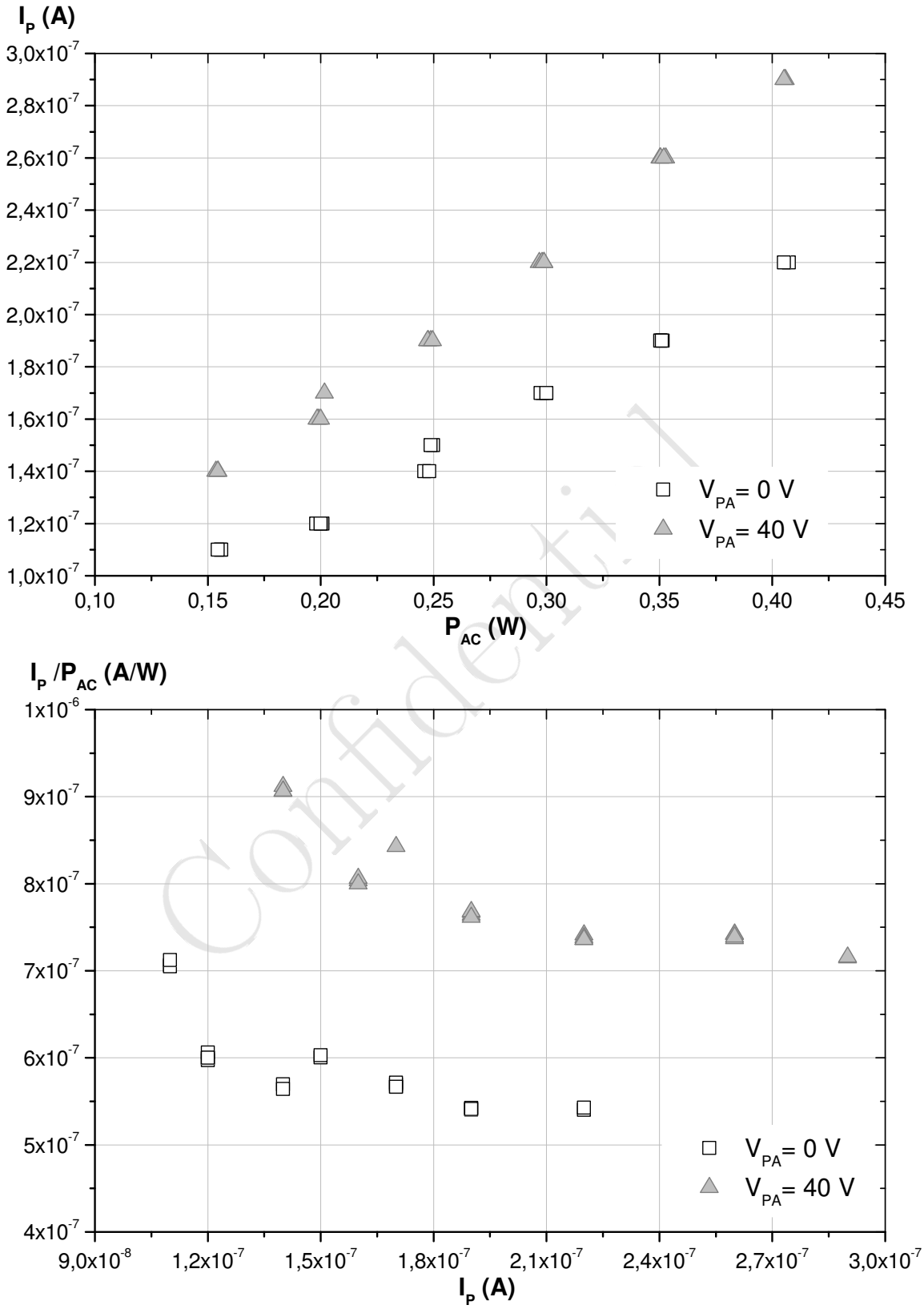

Confidential

Figure 2.17: Beam electron current *versus* power consumption (top) beam efficiency *versus* Beam electron current (bottom) for an aged N10 GDES cell (each I/V couple is measured 4 times).

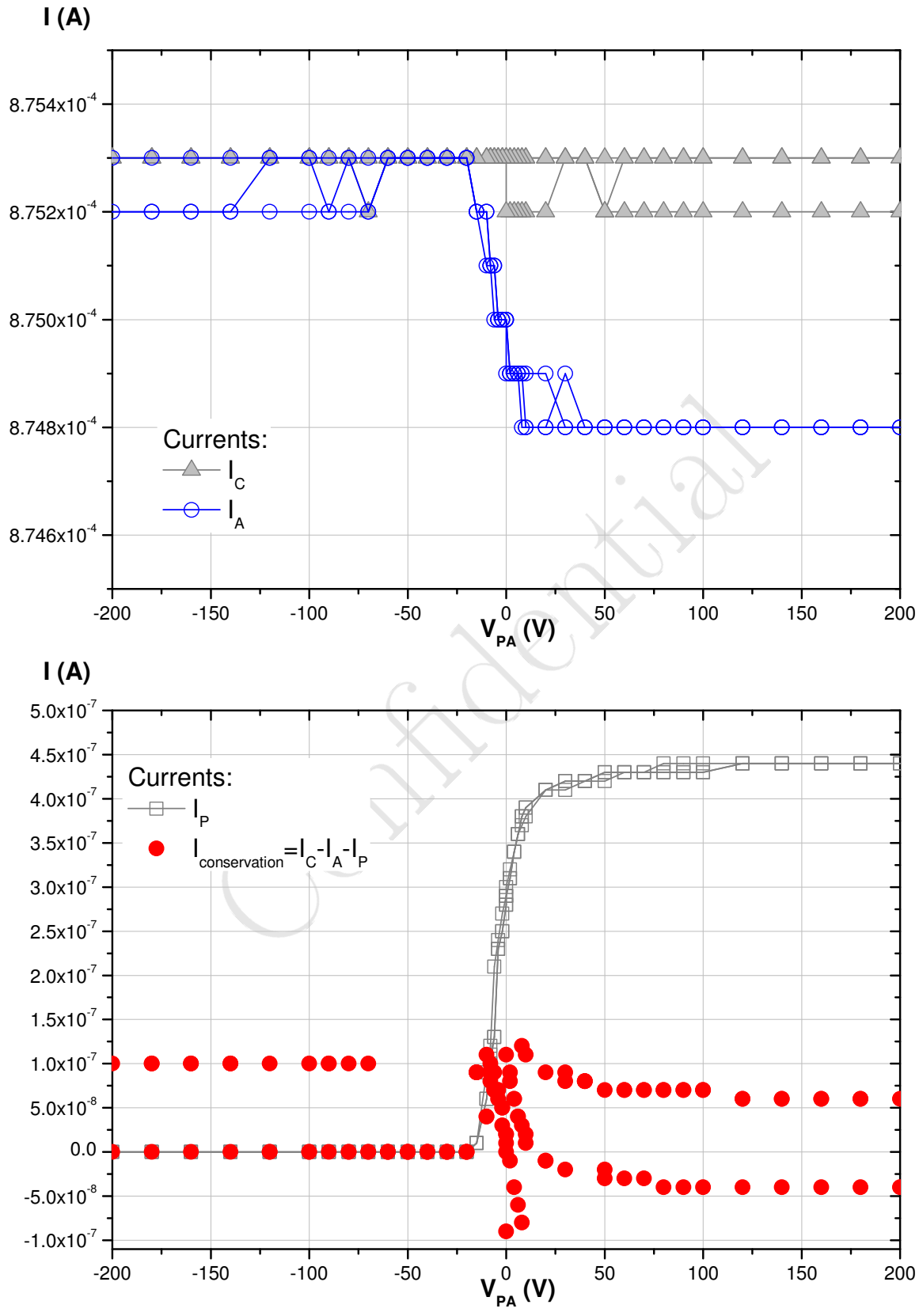

Confidential

Figure 2.18: Cathode and anode currents *versus* potential applied between the plate and anode (top); plate current and current conservation *versus* potential applied between the plate and anode (bottom) for an aged N10 GDES cell.

The measured currents are perfectly reproducible over the period of 15 min: only fluctuations of the least significant digit of the ammeter are observed. The cathode current is extremely stable during experiment according to balance equations 2.13 and 2.15. The current conservation is calculated from: $I_C - I_A - I_P$, as $I'_d = 0$. It is achieved by both the measurement system and the GDES cell.

2.7 Conclusion

To operate the GDES an inlet gas-flows of about 7×10^{-9} m^3/s is necessary. This flow can be turned off when electron beam is not required to limit gas load for the pumping system as the GDES cell can operate 5 mn after it is turned on. The Macor and Nylon are recommended for the cylindrical ring insulator, while Teflon is not, due to instabilities confirmed by Pavlik *et al* [64], and contrary to the work pulished by Gao *et al* [48]. The cheapest and easy-to-shape material is Nylon. The smallest tested inner diameter of the cell (10^{-2} m) was chosen. It is then possible to propose a smaller (lighter) GDES cell.

Nylon insulator with 10 mm of inner diameter was chosen having best stability with time and lower power consumption.

The principle of discharge regulation by limiting the current of the power supply allows us to choose an operating point of the discharge and provides stable electron currents (5 min after the discharge is started) suitable to be used as a source of electrons in a portable mass spectrometer. For the conception of the Electronic Control Unit, the characteristic of the discharge sustaining power supply must deliver DC potential values varying between 0-500 V and current values between 0-$1.5\text{x}10^{-3}$ A with limitation current capability.

The beam electron current is weak: $3\text{x}10^{-7}$ A at $V_{AC} = 450$ V for an emission efficiency equal to $7.1\text{x}10^{-7}$ A/W. However, with a narrow range of kinetic energy (10-20 eV) at anode aperture, it will be then easy to have all the electrons available to ionise the molecules.

Confidential

Chapter 3

GDES/EI Coupling

In this chapter, the GDES cell, a source of electrons operating at lower vacuum than a thermo-ionic filament, is coupled to an open Electron Impact ion source to create positive ions of targeted molecules.

Simulation studies were necessary to define the potential to be applied to the repeller of the ion cage and to the anode of the GDES cell to have the best electron focussing towards the ion cage of the source.

The coupling GDES/EI was experimentally tested with a Faraday cup detector. Currents were measured and the detected ion signal are compared when a filament and the GDES cell are used.

Confidential

3.1 Material and method

3.1.1 Device description

Figure 3.1 shows the coupling between GDES cell, EI source, and mass analyser (denoted as GDES/EI/LIT coupling). We only consider the internal ionisation by electron impact.

The open ion source comprises an electron repeller, a filament, an ion cage and a set of lenses (figure 3.2). The repeller focuses the electrons towards the ion cage. The ions created in the cage are focused towards the LIT by the set of lenses; the others are attracted by the repeller. Each lens has a function. The ion extraction lens, denoted as L_{El}, is at the same potential as the ion cage. The electron blocking/focussing lens, denoted as L_{Fo}, is held at negative potential (typically, - 70 V) to extract the ions from the ion cage and block electrons coming into the trap. The ion decelerating lens, denoted as L_{De}, is held constantly at 0V to decelerate ions during injection. The entrance end-cap lens, denoted as L_{En}, is switched between 0 V during injection and 15 V during trapping, denoted L_{En}. A positive potential higher than those applied to the ion cage ensures that no ions enter the trap. The coupling EI/lenses/LIT has been improved by simulation studies [17].

The GDES/EI source coupling is easy to implement: only the filament support is removed and the GDES is located in front of the EI source at usual gas inlet (figure 3.2). The electrons emerging

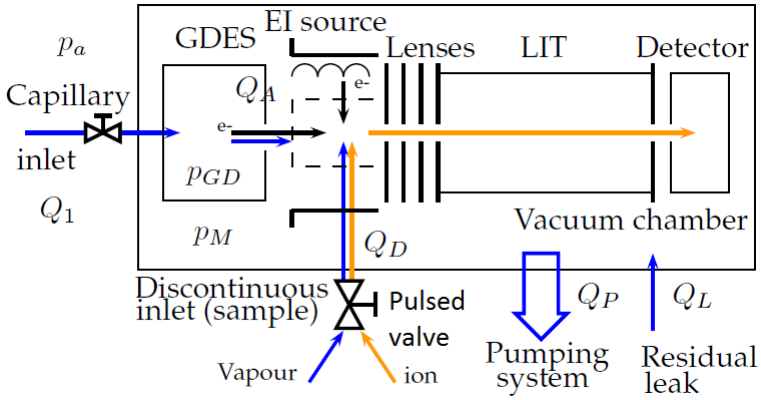

Figure 3.1: Principle of the mass spectrometer. Coupling between GDES cell, EI source, and mass analyser. Gas (blue arrow), LIT ion (yellow arrow) and electron (black arrow) flows.

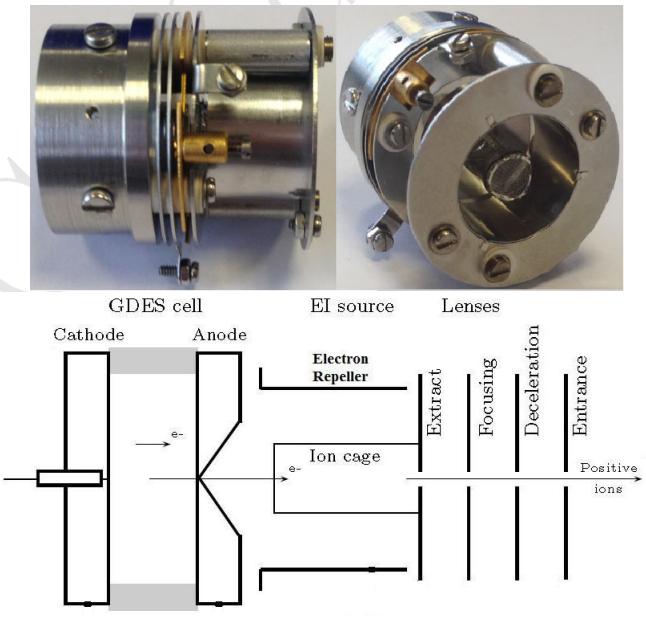

Figure 3.2: (Top) Picture of the open EI source and lenses. (Bottom) Scheme of GDES/EI coupling.

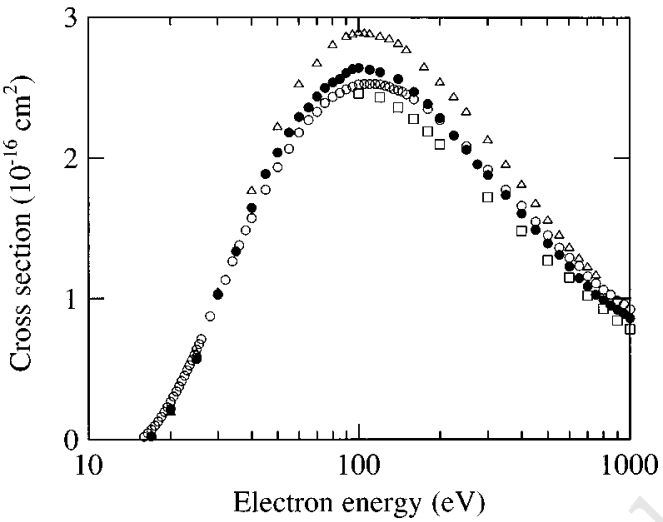

Figure 3.3: Total electron-impact ionisation cross-section of N_2 from [65].

from the anode orifice enter the repeller cylinder axially. The potential applied to the anode fixes the energy of the electrons in the ion cage, while the potentials applied to the anode and repeller have an effect on the electron focusing from the anode orifice towards the ion cage. The distance between the GDES and the repeller influences the electron focusing according to the potentials applied to the ion cage, anode and repeller. The potential applied to the ion cage was maintained at 3 V in the experiments.

3.1.2 Electron ionisation at 70 eV

Ionisation of atoms by electron impact produces single-charged or multi-charged positive ions, while molecules are fragmented. The ionisation cross-section depends on the kinetic energy of the electrons. For a large number of gases, the optimum ionisation efficiency occurs for energies ranging between 50 et 200 eV [65, 66]. Large databases (for instance, NIST) of fragmentation patterns at 70 eV of molecules are provided. For instance, the EI at 70 eV of N_2 (the major component of the ambient air, at 78 %) gives the ion fragments: $^{14}N_2^+$ at m/z: 28 (93 %), $^{14}N^+$ at m/z: 14 (6 %), $^{15}N^{14}N^+$ at m/z: 29 (1 %) and $^{15}N_2^+$ at m/z: 30. In figure 3.3, the total electron impact ionisation cross-section is given for N_2.

3.1.3 Potential applied to anode

The total energy of an electron is the sum of its kinetic and potential energies. The total energy of the electron is conserved from the GDES anode to the ion cage, whatever the trajectory path, so:

$$E_{k,A} + E_{p,A} = E_{k,IC} + E_{p,IC} \tag{3.1}$$

Confidential

$E_{k,IC}$ (eV) $\rightarrow$	30	70	100
$E_{k,A}$ (eV) $\downarrow$	V_A (V)		
0	-27	-67	-97
5	-22	-62	-92
10	-17	-57	-87
15	-12	-52	-82
20	-7	-47	-77
25	-2	-42	-72
50	23	-17	-47

Table 3.1: Polarisation potential applied to anode V_A according to electron kinetic energy at anode orifice $E_{k,A}$ for three values of the electron kinetic energy inside ion cage, $E_{k,IC}$, with ion cage at $V_{IC} = 3$ V.

Confidential

$$E_{k,A} + qV_A = E_{k,IC} + qV_{IC} \tag{3.2}$$

where $q = -1$ is the charge of electron so that qV_A have dimension of energy in eV; $E_{k,A}$ and $E_{k,IC}$ are the kinetic energies of electrons at the anode and ion cage, respectively; $E_{p,A}$ and $E_{p,IC}$ are the potential energies at the anode and ion cage, respectively. The polarisation potential of the anode can be then expressed by:

$$V_A = E_{k,A} - E_{k,IC} + V_{IC} \text{ (V)} \tag{3.3}$$

For instance, for electrons emerging from the anode orifice at kinetic energy $E_{k,A}$ and to have the electrons at 70 eV in the ion cage at $V_{IC} = 3$ V, the potential applied to the anode, is calculated from:

$$V_A = E_{k,A} - 67 \text{ (V)} \tag{3.4}$$

Table 3.1 gives the potential applied to the anode according to electron kinetic energy at the anode orifice for three targeted values of electron kinetic energy in the ion cage, with the ion cage at 3 V.

3.2 Simulation results

3.2.1 Charged Particles Optics software

The commercial software Charged Particle Optics (CPO) is used for the simulation studies [67]. In the CPO the software, the device design is constructed from either predefined electrode shapes or equations.

CPO employs a Boundary Element Method (BEM) to calculate the electrical potential and field of conducting electrodes [68]. For the BEM, charges are distributed over the electrode surface, according to the potential applied to the electrodes. Consequently, it requires a segmentation of the electrodes for charge distribution. Adaptive surface meshes become smaller where accuracy is required. Electrostatic field solving is done to high accuracy using the BEM rather than traditional Finite Element Method (FEM) [69], like in SIMION software or Finite Difference Method (FDM).

Moreover, charge (electron, ion) trajectories between the electrodes can be calculated involving space charge, collision with a background gas and relativistic effects (Bulirsch-Stoer), if any. CPO software has a drawback when using a great number of ions: a large amount of time is necessary to solve the problem.

3.2.2 Design and simulation conditions

The CPO 2D design with the electrode segmentation of GDES/EI/Lenses coupling in the plane $z0y$ is given figure 3.4. In these simulations, the GDES cell is located at 10^{-3} m of the left edge of the repeller. Close to the anode aperture, the segmentation is increased in order to have a better accuracy in electron trajectories.

The potential applied to the cathode is $V_C = -500$ V, to the ion cage and L_{El} is $V_{Io} = 3$ V, to the focussing lens is $V_{Fo} = -100$ V, to the decelerating is $V_{De} = 0$ V and to the entrance lens is $V_{En} = 0$ V. The initial positions of electrons are drawn uniformly in the circle defined by the anode aperture. The initial velocities of electrons are drawn from an uniform 3D angular distribution with a constant velocity module given by the electron kinetic energy at the anode orifice $E_{K,A}$. Electron trajectories are simulated from the anode aperture to the ion cage. The electron trajectory is stopped when the electron hits an electrode.

3.2.3 Influence of the potential applied to the repeller

The influence of the repeller potential V_{Re} has been tested for the following conditions: $E_{k,A} = 67$ eV; $V_A = 0$ V and $V_{IC} = 3$ V. Taking into account energy conservation: $E_{k,IC} = E_{k,A} + qV_A - qV_{IC}$ (with $q = -1$, for electrons), the electron kinetic energy in the ion cage is then: $E_{k,IC}$ = 70 eV.

An example of electron trajectories from the anode orifice to the ion cage is shown in figure 3.5, for four values of the potential applied to the repeller, V_{Re} = - 30, - 70, - 100 and - 200 V. Only 20 electrons are simulated.

Confidential

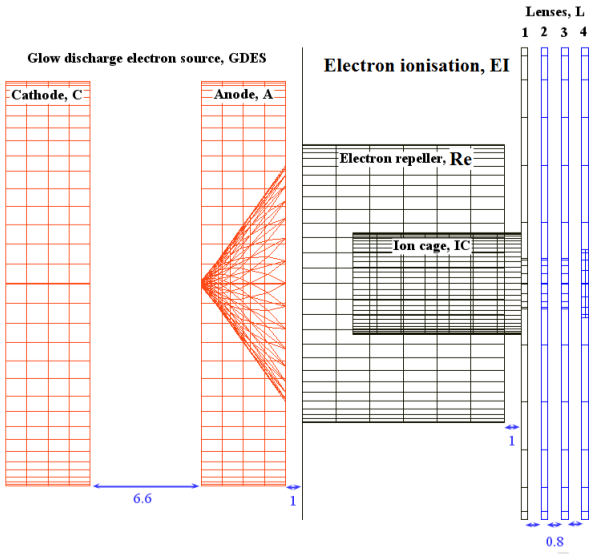

Figure 3.4: CPO 2D design with the electrode segmentation of GDES/EI/Lenses coupling in the plane $z0y$. The number between the electrodes corresponds to the distance in mm. From left to right: GDES: cathode and anode (orange); ion source: electron repeller, ion cage and extraction lens (1) (black); focussing (2), blocking/decelerating (3) and entrance lenses (blue) (4).

The best focussing of electrons towards the ion cage occurs for $V_{Re} = -70$ V.

The use of a low number of samples could induce a bias. For that reason, the number of electrons hitting the ion cage is calculated for different values of the potential applied to the repeller and for 10 different sequences of the uniform drawing of initial conditions at the anode orifice. Each simulation involves 100 electrons.

The mean value of the number of electrons hitting the ion cage and each standard deviation obtained are plotted versus the potential applied to the repeller V_{Re}, chosen from -150 to 0 V in increments of 10 V. (figure 3.6). As a result, the sequence #4 of CPO drawing is chosen for the following simulations.

3.2.4 Repeller potential according to kinetic energy

The number of electrons hitting the ion cage is plotted *versus* the potential applied to the repeller for three values of the initial kinetic energy of electrons at the anode orifice: $\mathrm{E}_{k,A} = 17$, 27 and 67 eV, to obtain electrons at kinetic energy in the ion cage at $\mathrm{E}_{k,IC} = 20$, 30 and 70 eV, respectively. Each simulation involves 500 electrons (figure 3.7).

Each curve has an optimum value of about 100%. We obtain the largest kinetic distribution with $E_{k,A} = 67$ eV. The maximum value are obtained with the three $E_{k,A}$ for V_{Re} =17, 27 and 67 eV.

For instance, the best focussing effect is for V_{Re} = - 80 V for $E_{k,IC}$= 70 eV. A large range of values for V_{Re} is possible for the highest kinetic energies. In the following simulations, the potential

Confidential

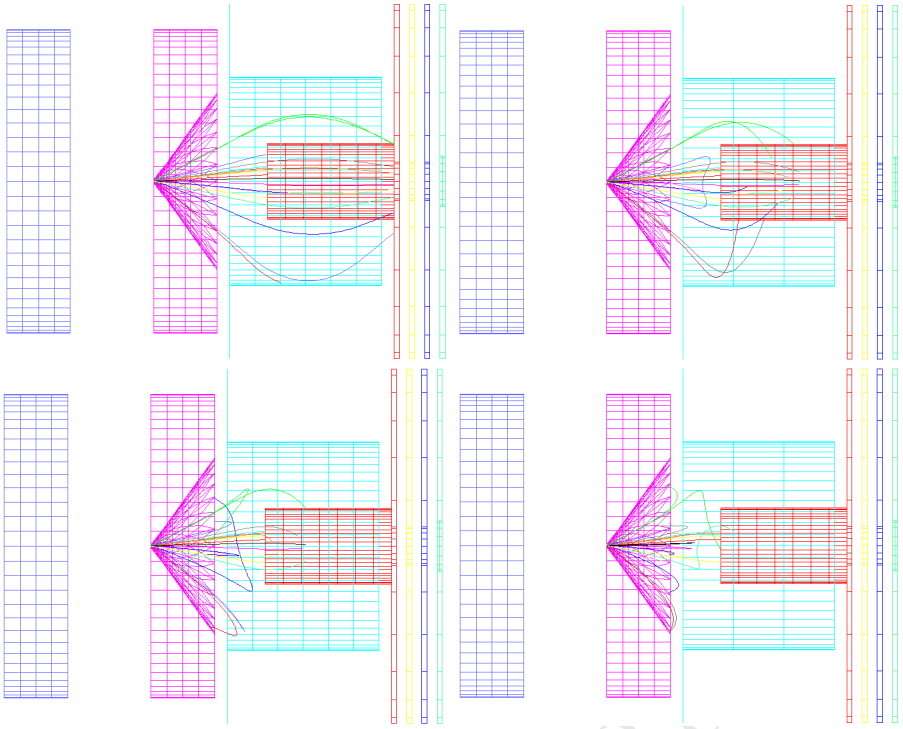

Figure 3.5: Example of electron trajectories from GDES anode orifice to ion cage for: V_{RE} = - 30, - 70, -100 and -200 V (from the left to the right, then from the top to the bottom).

repeller value will be then chosen at the optimal number of electron according to the desired value of $E_{k,IC}$.

3.2.5 Distribution of electron kinetic energy in the ion cage

The electron kinetic energy distribution at the ion cage must be known and controlled, as it is the main parameter that influences the positive ion creation and fragmentation.

The distribution of kinetic energies of electrons in the ion cage are calculated from many simulations performed for different values of the initial kinetic energy at anode and of the potential applied at the anode, and for three values of the potential repeller, V_{Re} = -27, -37 and -80 V, corresponding to the best focussing of electrons having a centred kinetic energy distribution at 20, 30 and 70 eV, respectively. Each simulation involves 100 electrons. The number of electrons hitting the ion cage is then plotted versus electron kinetic energy at the anode orifice and in the ion cage (figure 3.8, 3.9 and 3.10).

For instance, if the distribution of initial kinetic energy at anode is uniform between 0-20 eV, the mean value is 10 eV. To have a distribution of kinetic energy centred around 30 eV in the ion cage, the potential applied to the anode must be V_A= -17 V and to have the best focussing of electrons

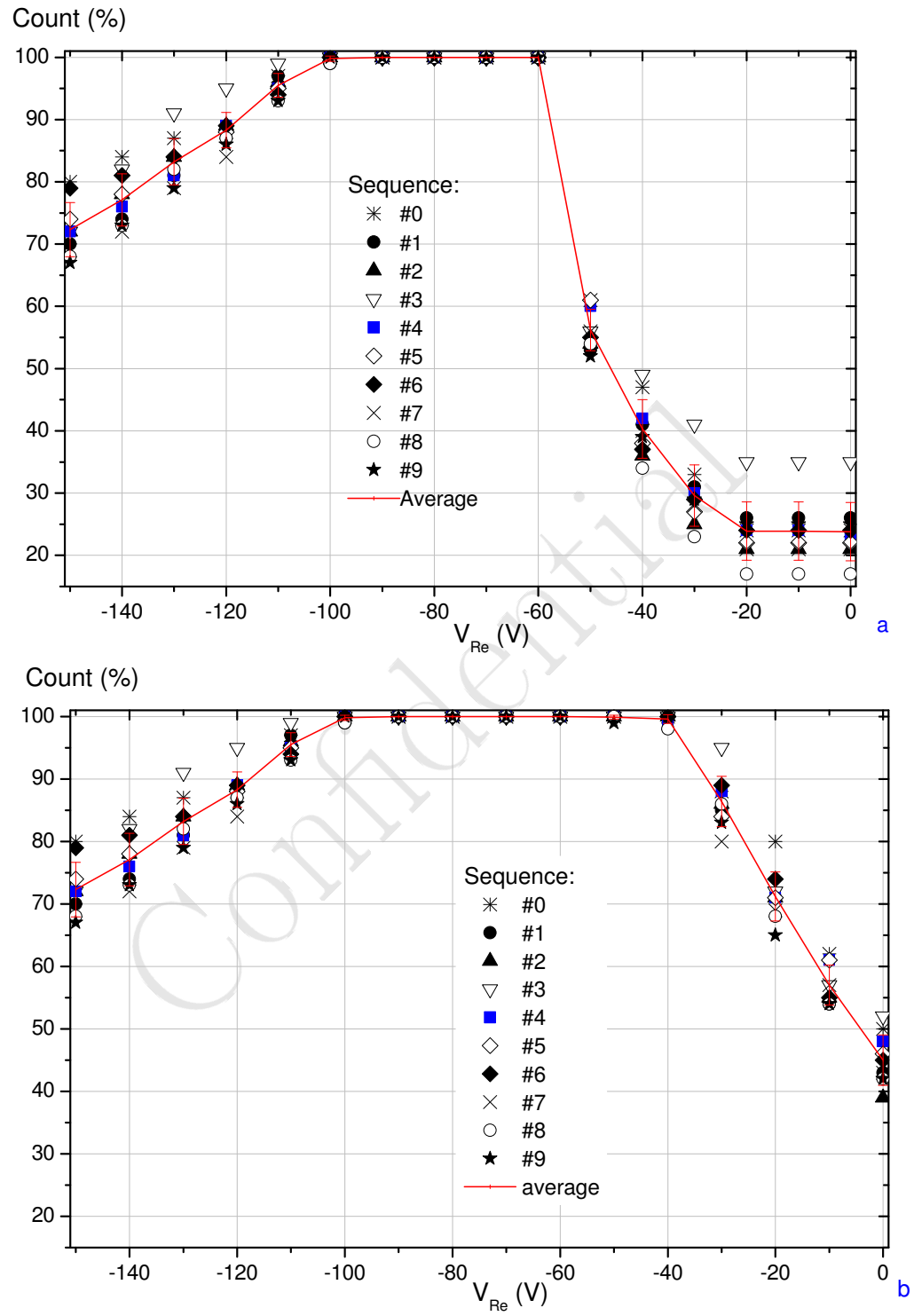

Confidential

Figure 3.6: Number of electrons hitting the IC, graph a and hitting IC+L_E, graph b at different V_{Re} potentials at $E_{kA} = 67$ eV for 10 sequences with 100 electrons simulated.

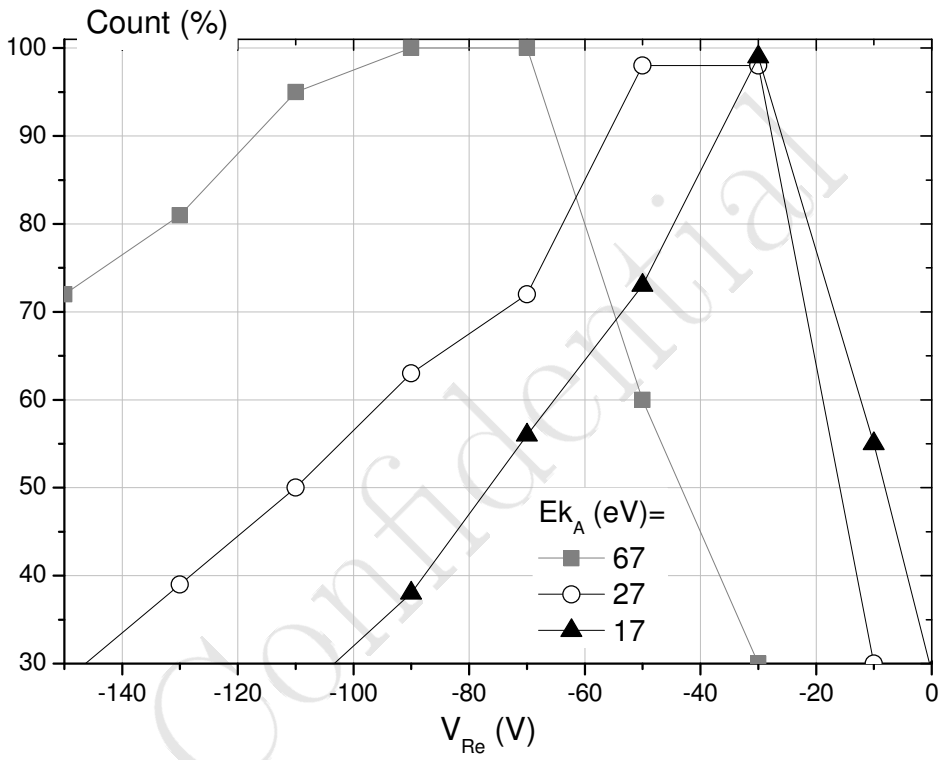

Confidential

Figure 3.7: Number of electrons hitting the ion cage *versus* V_{Re} varying between -150 to 0 V, with $E_{k,A}$ = 17, 27 and 67 eV. 500 electrons are simulated with sequence #4.

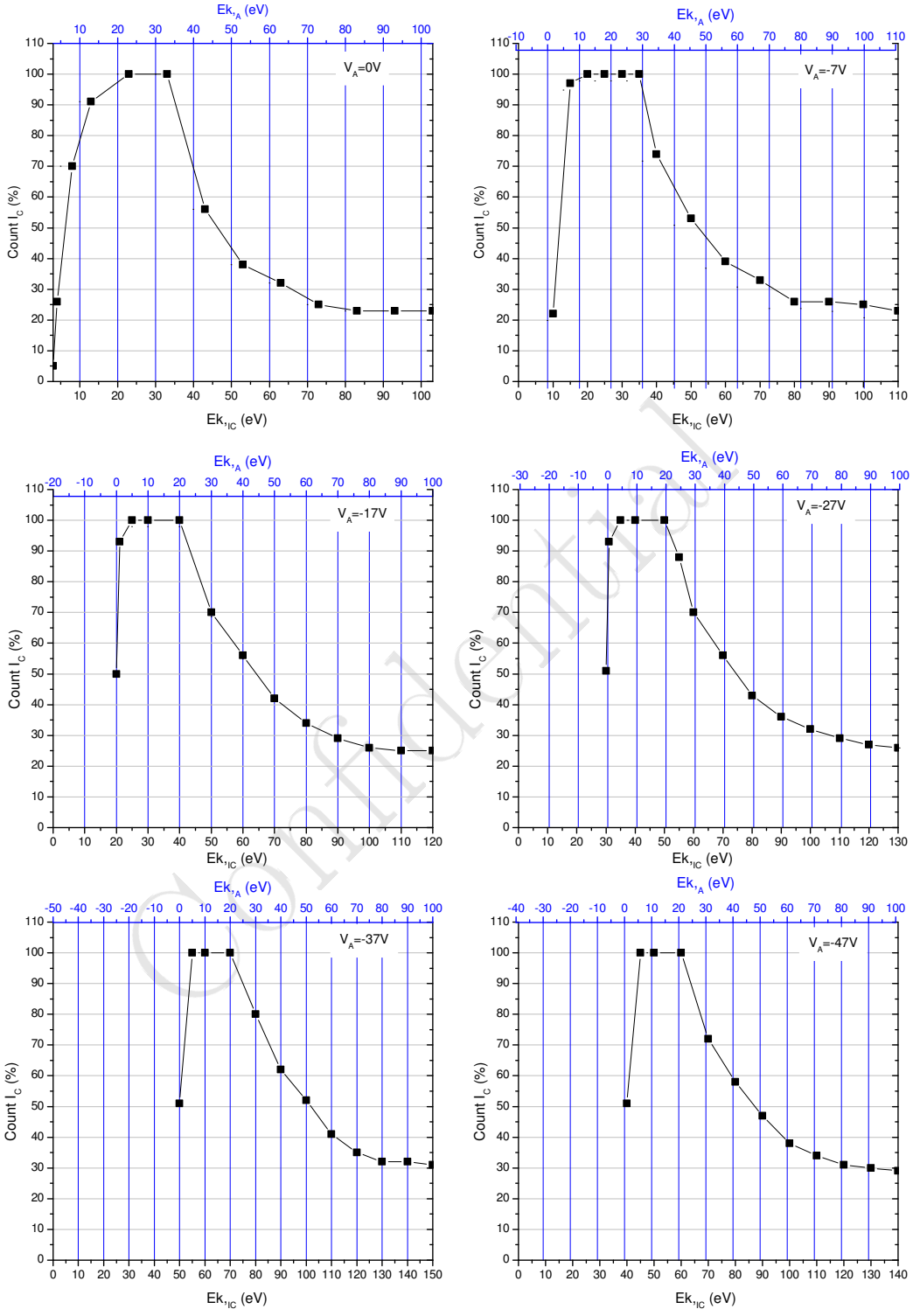

Figure 3.8: Distributions of kinetic energies of electrons at the ion cage for uniform distribution of kinetic energies at the anode orifice. $V_{Re} = -27$ V.

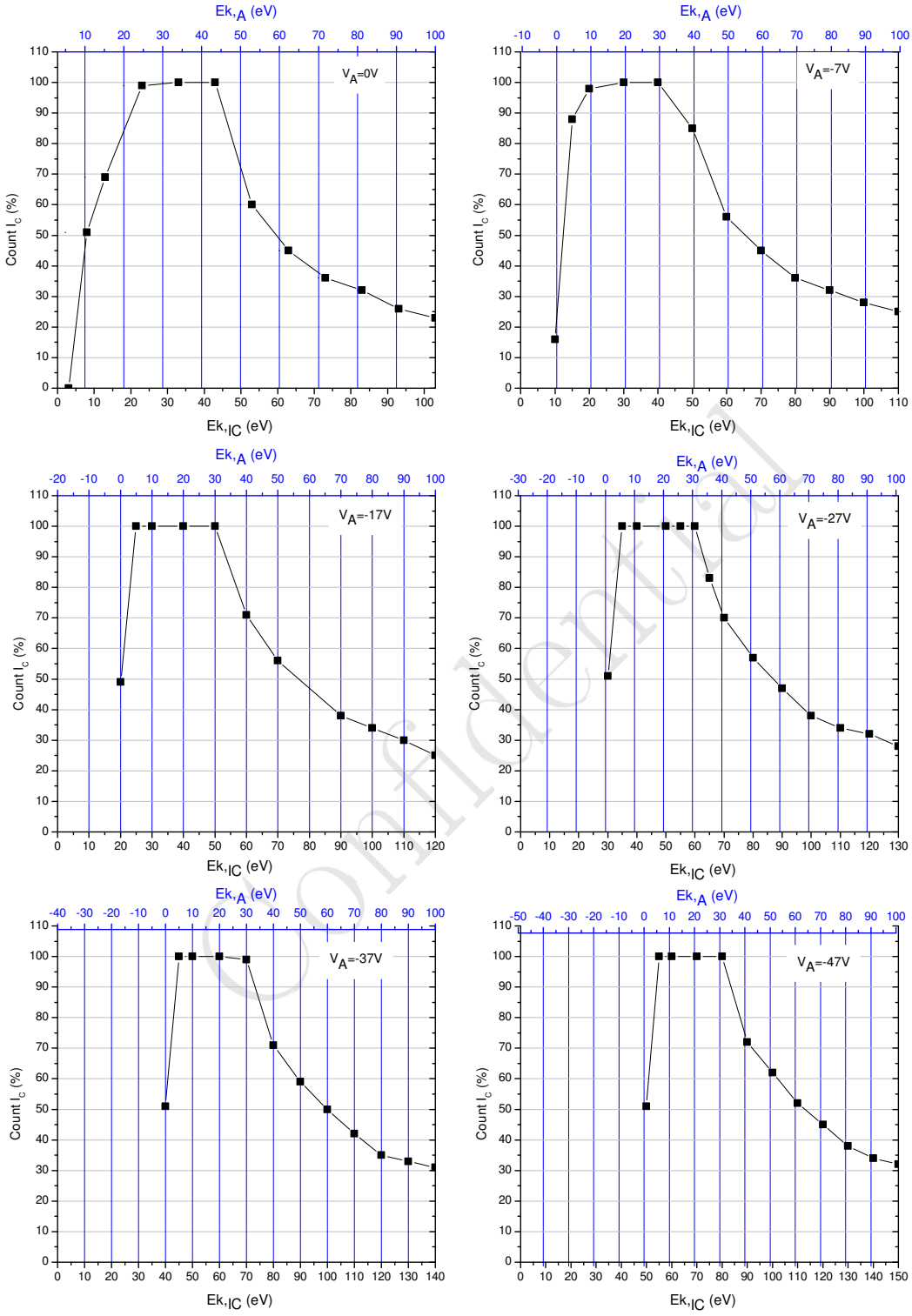

Figure 3.9: Distributions of kinetic energies of electrons at the ion cage for a uniform distribution of kinetic energies at the anode orifice. $V_{Re} = -37$ V.

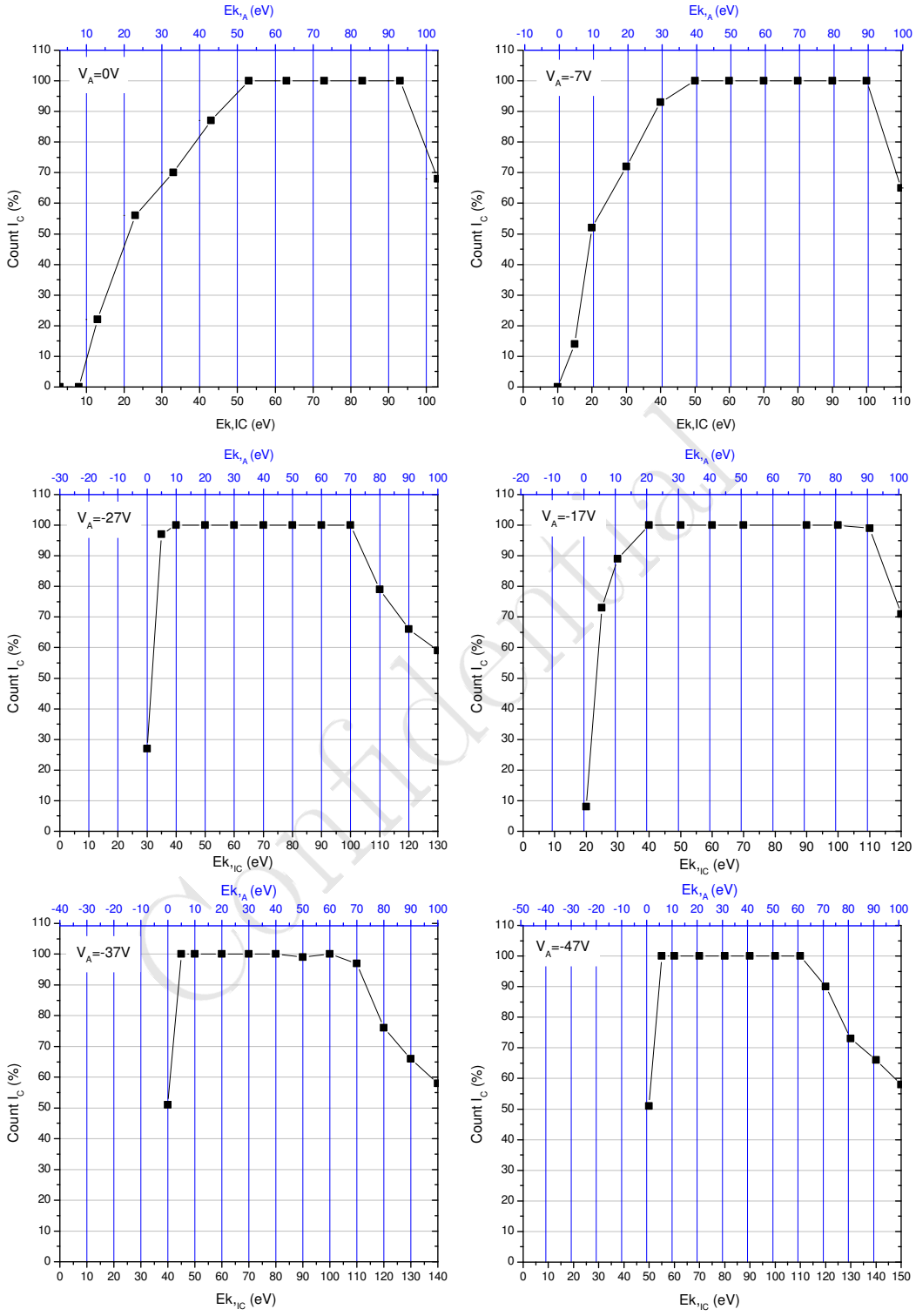

Figure 3.10: Distributions of kinetic energies of electrons at the ion cage for a uniform distribution of kinetic energies at the anode orifice. $V_{Re} = -80$ V.

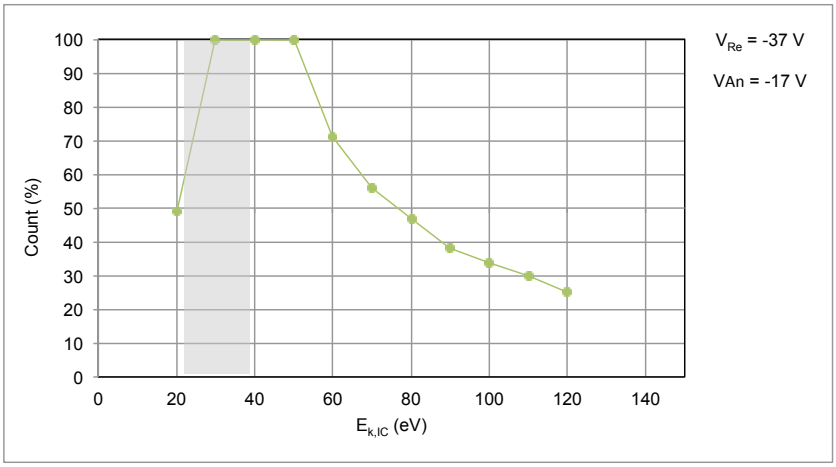

Figure 3.11: Distribution of kinetic energy of electrons at the ion cage for a uniform distribution of kinetic energies at the anode orifice and for $V_A = -17$ V and $V_{Re} = -27$ V.

V_{Re}= -37 V (figure 3.11). The grey rectangle corresponds to the initial distribution of kinetic energy at anode from 0 to 20 eV. The electrons having desired kinetic energies are transferred to the ion cage with these applied voltages.

Other results show that it is always possible to find a pair of values for the potentials applied to the repeller and between the anode and ion cage to have a kinetic energy distribution with a mean value centred between 20 and 100 eV giving a maximal number of electrons.

3.3 Experimental results with filament

First, experiments were performed with the coupling EI/Lenses/Detector for determination of the general operating conditions and to have results with filament to compare with those obtained with GDES.

3.3.1 Experimental device

The EI source and Faraday cup detector, provided by University of Liverpool, is flange-mounted. The gas inlet is mounted on another flange located on the opposite side to the one supporting the EI-lenses-detector assembly (figure 3.12). The gas inlet is adjusted by means of a capillary and/or fine-metering valve. A 1/4" tubing carries the neutrals at the entrance of the filament support of the EI source.

For the vacuum chamber, the mass throughput conservation at equilibrium is given by the following relation:

$$C_1(p_a - p_M) = S_{ef} p_M \tag{3.5}$$

where C_1 (m^3/s) is the capillary conductance, S_{ef} (m^3/s) the effective pumping speed, p_a (Pa)

Confidential

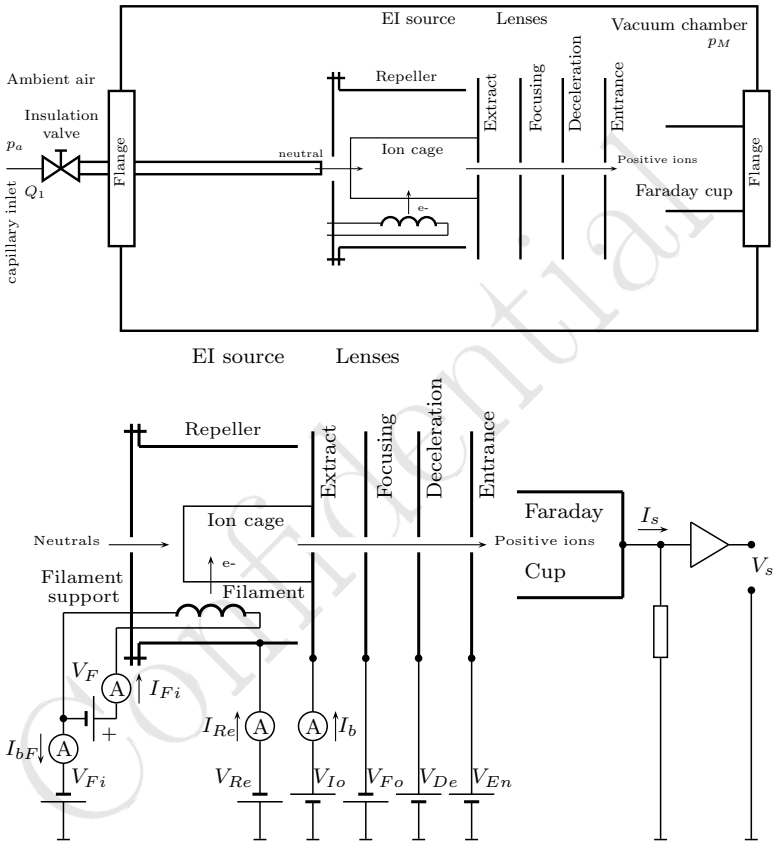

Figure 3.12: (Top) Mechanical design to test EI source with Faraday cup. (Bottom) Electrical design to test EI source with Faraday cup.

the atmospheric pressure and p_M (Pa) the vacuum chamber pressure. With l_1 = 16.5x10^{-2} m, C_1 = 7 × 10^{-9} m^3/s (see previous chapter). It is assumed that S_{ef} = 125 l/s with Varian Turbo V250 Macro-torr pump having 250 l/s pumping speed. The lowest value (measured by a Bayer-Alpert gauge) for p_M is then about 5.33×10^{-3} Pa.

The measured currents of the system are conserved and satisfy the following equation (figure 3.12):

$$I_{bF} = I_{Re} + I_b \tag{3.6}$$

The currents measured on lenses are null, whatever the potential applied on the lenses.

The current measured by the Faraday cup I_s is expressed by:

$$I_s = \frac{N \times e}{t} \tag{3.7}$$

where N is the number of ions striking the cup in a time t (min) and e the elementary charge (about 1.6 × 10^{-19} C). For instance, a measured current of one nano amp corresponds to about 6 × 10^9 ions striking the Faraday cup each second. A signal amplifier provides an output voltage proportional to the current: $V_s = \alpha I_s$. The amplifier/converter factor α is unknown.

3.3.2 Electron current stability

The stability of the currents I_F and I_b are achieved after 10 min the filament is turned on (figure 3.13).

3.3.3 Potential applied to the repeller

The electron currents I_{bF}, I_{Re} and I_b are measured according to the potential applied to the repeller V_{Re}, for three values of the potential applied to the filament V_{Fi} = -67, -27 and -17 V, corresponding to the electron kinetic energies in the ion cage of 70, 30 and 20 eV, respectively (figure 3.14).

As the filament is close to the repeller, the potential applied between the filament and repeller influences the filament electron emission as well as the potential applied between the filament and ion cage. As a consequence, the current collected by the ion cage and extract lens decreases for the highest values of V_{Re}, corresponding to $I_{Re} \neq 0$. Hence, the potential applied to the repeller is chosen for the highest value of I_b (the maximal value of the current collected by the ion cage) with $I_{Re} = 0$, *i.e.* V_{Re}= -66, -26 and -16 V for V_{Fi} = -67, -27 and -17 V ($E_{k,IC}$ = 70, 30 and 20 eV, respectively). The more V_{Fi} is negative, the higher the currents are. The results on the figure 3.14 show the important space charge, because we doesn't observe the negative value of current.

Confidential

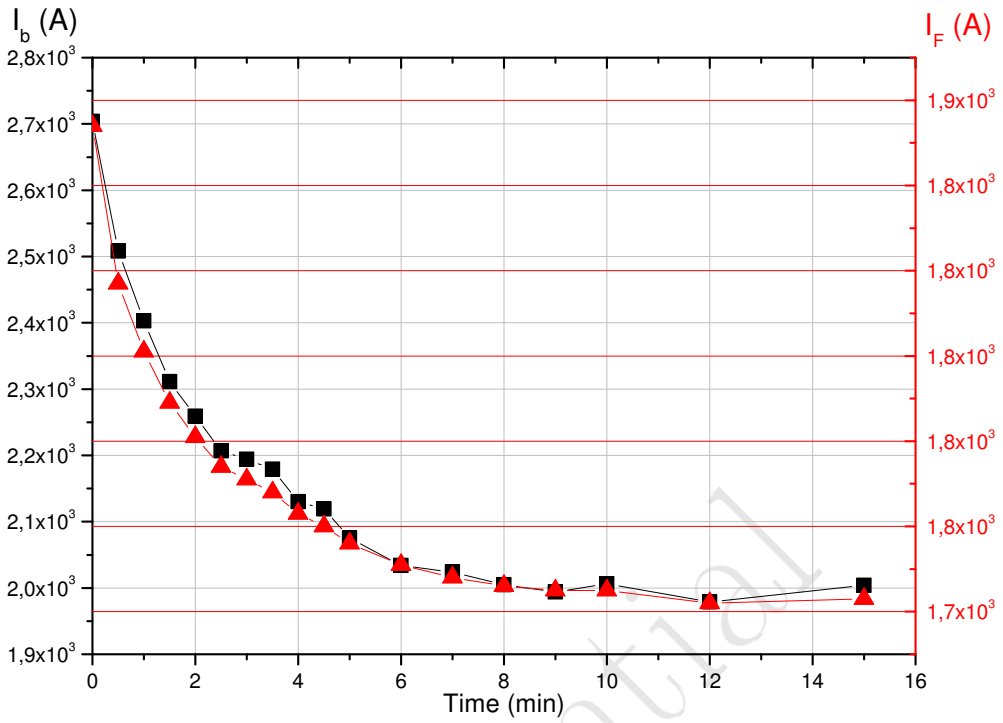

Figure 3.13: Evolution of filament current and emitted current according to time at $p_M = 3.99 \times 10^{-5}$ Pa.

3.3.4 Ion focussing and transmission

The ion focussing and transmission towards the Faraday cup depend only on the potentials applied to the ion cage and lenses (figure 3.15). V_{IC} is fixed at 3 V. An optimal value is obtained for V_{Fo} = -70 V , V_{De} = -10 V and V_{En} = -5 V.

3.3.5 Sensitivity and detection low-threshold

The sensitivity of detection is expressed as the capability to detect an ion current by the Faraday cup detector according to the electron current at the ion cage (involved in the ion creation). The current I_b is varied by means of I_F, the current of the filament. The pressure value of the vacuum chamber is varied by means of a fine-metering valve located at gas inlet and measured by the Bayard-Alpert gauge. The value of p_M = 4.66 $\times$ 10^{-3} Pa is obtained with the $1.65.10^{-3}$ m capillary at inlet.

V_s is plotted versus I_b for different values of p_M, the pressure in the vacuum chamber (top-curve of figure 3.16). The Faraday cup signal is measurable as much lower than 10^{-4} V with a negative offset of about 2×10^{-3} V, measured when a positive voltage is applied to the focussing lens, so that no positive ions created in the ion cage are detected.

The Faraday cup signal depends on the vacuum chamber pressure (middle-curve of figure 3.16). The optimal value of the detected signal for low values of electron current is when vacuum chamber

Confidential

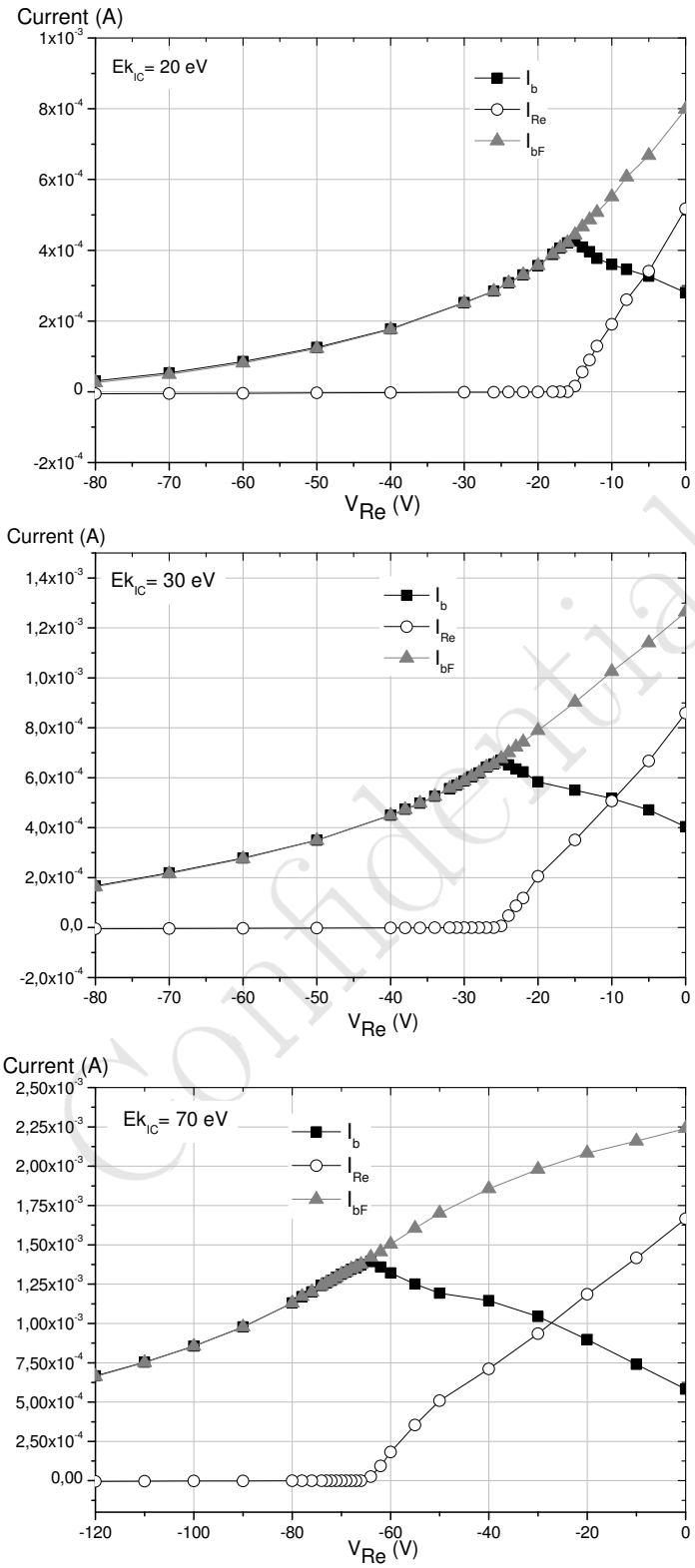

Confidential

Figure 3.14: Electron currents in the ion source according to the potential applied to the repeller for three values of the potential applied to the filament. The potential applied to the ion cage is 3 V.

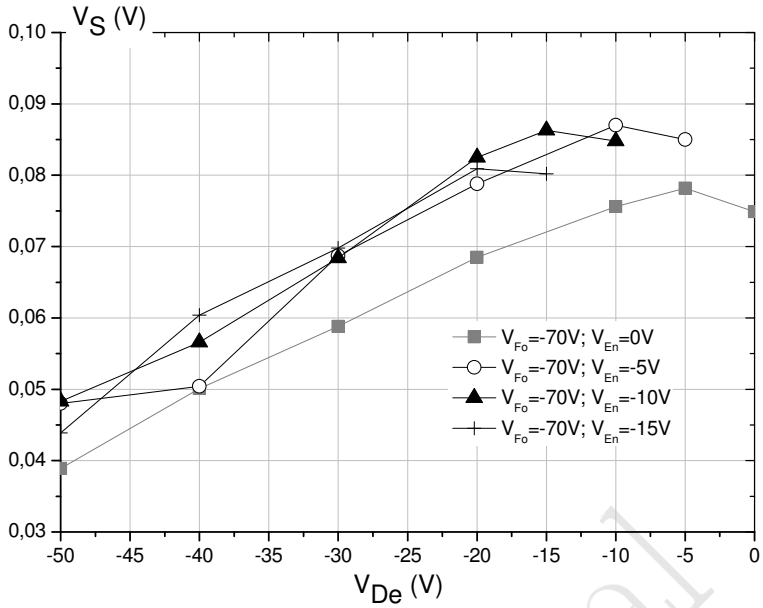

Figure 3.15: Faraday cup detector signal *versus* potentials applied to the lenses.

operates at a pressure value of about p_M = 6.66-9.33 x 10^{-4} Pa (bottom-curve of figure 3.16).

3.4 GDES/EI Experimental results

3.4.1 Experimental device

The same vacuum chamber and flanges are used. The filament support is removed from the ion source. The glow discharge cell is mounted on the flange supporting the gas inlet with the $1.65.10^{-3}$ m capillary (figure 3.17). The GDES cell is located 10^{-2} m away from the repeller.

To operate the Faraday cup detector at a higher sensitivity (bottom curve of figure 3.16), a lower pressure value (two times lower) is then achieved by using another identical pumping system. The experimental value $p_M = 2.26 \times 10^{-3}$ Pa is then measured by the Bayard-Alpert gauge.

The neutrals and electrons passing through the anode aperture are involved for ion creation in the ion cage of the source. The ion signal measured is mainly due to ionisation of N_2.

The kinetic energy of electrons in the ion cage is set by the voltage applied to the anode, with respect to the voltage applied to the ion cage. The cathode, anode, repeller and electron beam currents are measured. The measured currents of the system are conserved and satisfy the following equation (bottom figure 3.17):

$$I_C = I_A + I_{Re} + I_b \tag{3.8}$$

Confidential

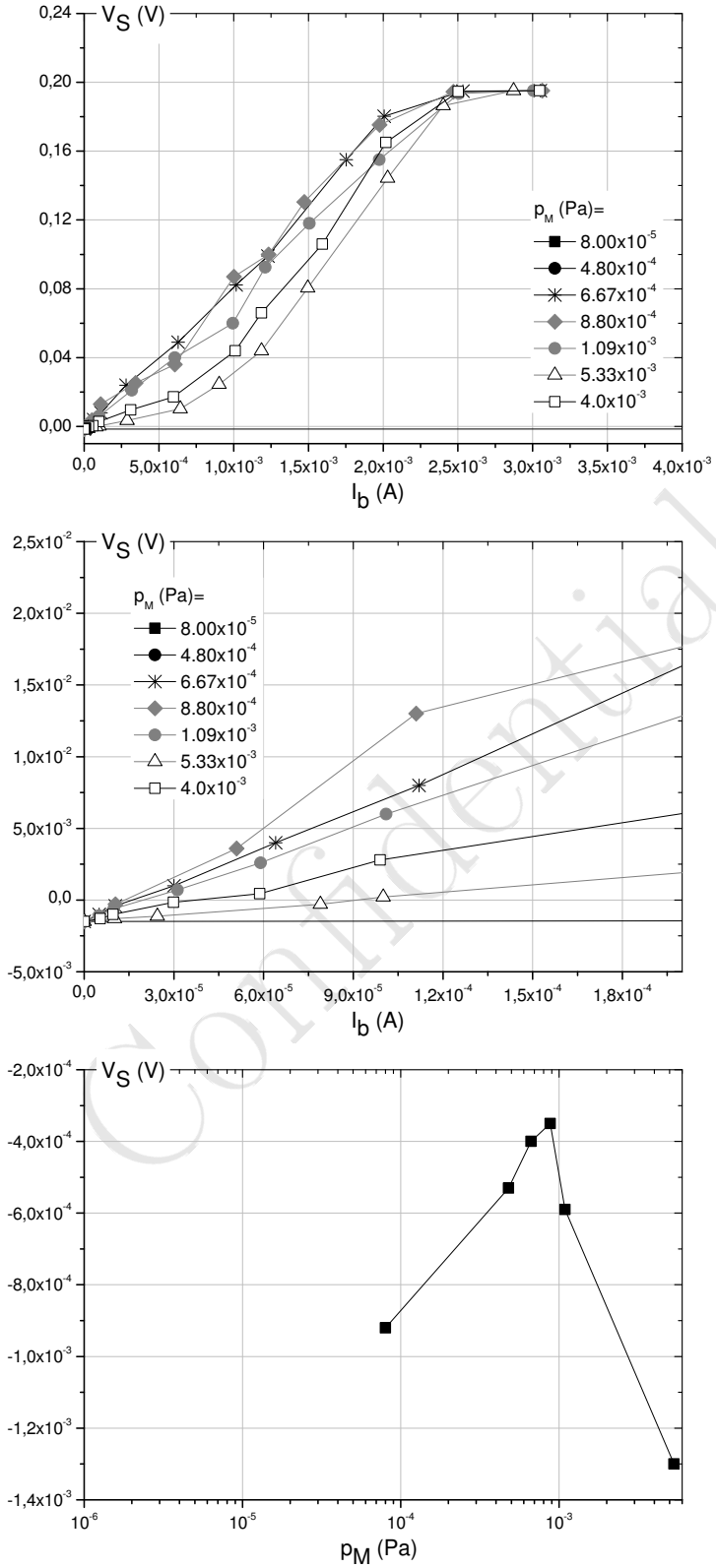

Confidential

Figure 3.16: Faraday cup detector signal *versus* electron current and pressure in the vacuum chamber. (Top) Signal detected by the Faraday cup detector versus I_b. (Middle) Zoom of the top curve for low values of I_b. (Bottom) Signal detected by the Faraday cup detector versus p_M when $I_b = 10^{-5}$ A.

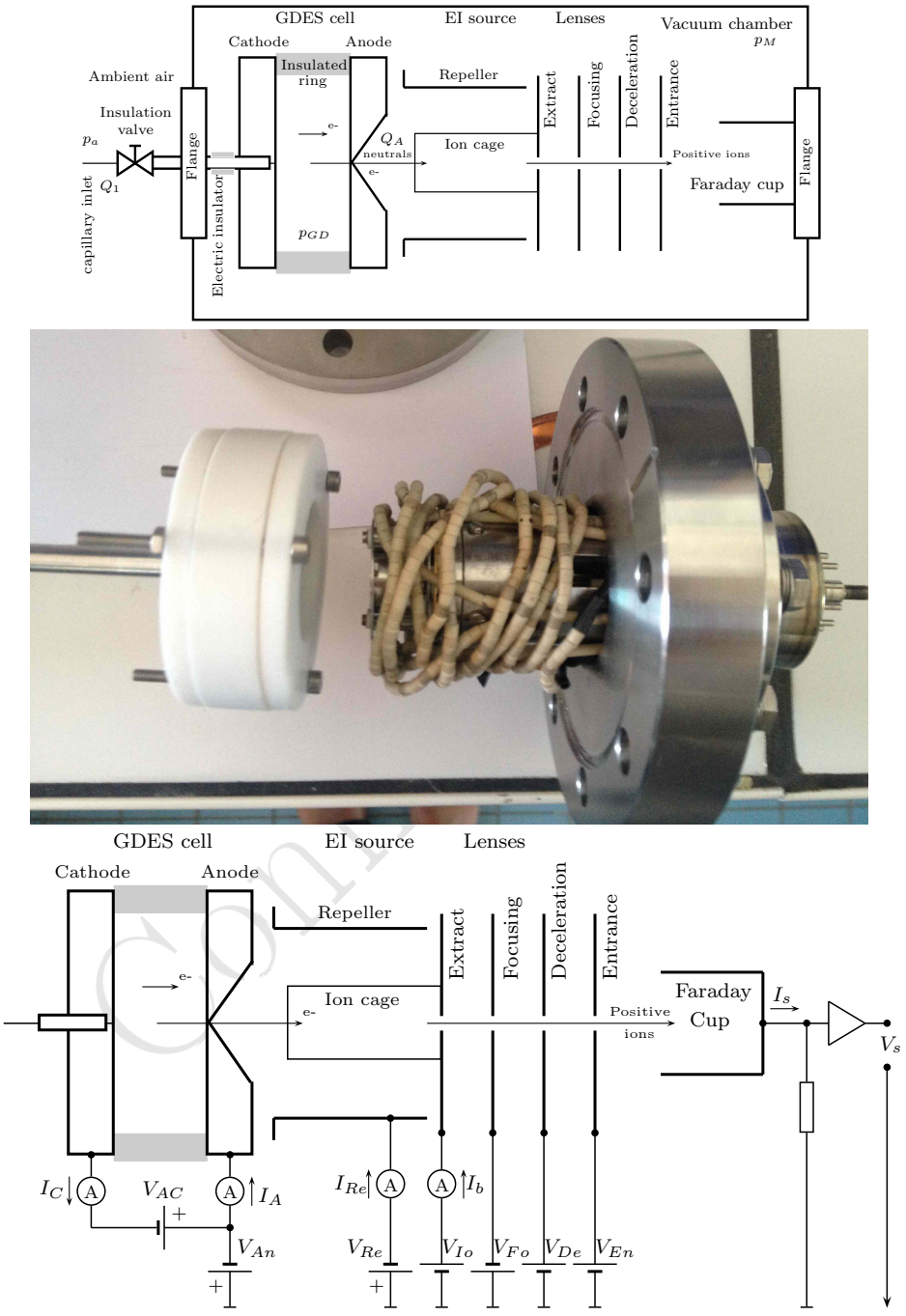

Figure 3.17: GDES-EI source coupling with Faraday cup detector. (Top) Scheme of testing device. (Middle) photo of GDES and EI/lenses/Faraday cup mounted on a flange. (Bottom) Electric testing device.

	I_F or I_C (A)	V_F or V_{AC} (V)	P (W)	I_b (A)	V_s (V)	I_b/P (A/W)	V_S/P (V/W)
Filament (optimal)	1.75	2.3	4	1.5×10^{-3}	0.1	3.8×10^{-4}	25×10^{-3}
Filament (degraded)	1.56	2.3	3.6	10^{-5}	5×10^{-4}	2.8×10^{-6}	14×10^{-5}
GDES (optimal)	630×10^{-6}	420	0.2	1.2×10^{-7}	1.9×10^{-3}	6×10^{-7}	9.5×10^{-3}

Table 3.2: Comparison between filament and GDES of currents and detector signal, for V_{Re} = -80 V and V_A = -57 V, corresponding to optimal operating conditions to have electron kinetic energy in the ion cage centred at 70 eV.

The discharge sustaining voltage applied between the anode and cathode is $V_{AC} = 420$ V, with $I_C = 630.10^{-6}$ A and $1.65.10^{-3}$ m capillary inlet.

3.4.2 Electron currents and Faraday cup signal

The currents measured at the ion cage and repeller, and the Faraday cup detector signal are plotted *versus* the potential applied to the anode for different values of the potential applied to the repeller (in figure 3.18), and *versus* the potential applied to the repeller for different values of the potential applied to the anode (in figure 3.19).

The maximum value of the current measured by the ion cage is about $2\text{x}10^{-7}$ A. The currents measured have the same magnitude than those measured by the plate located in front of anode aperture, when the GDES cell is tested alone. The optimal values of the current I_b are obtained for: $-40 < V_{Re}(\text{V}) < -20$ and $-100 < V_A(\text{V}) < -40$. No current is measured at the repeller except when the potential applied to the repeller increases from -20 to 0 V: few electrons are then attracted by the repeller instead of the ion cage (see top and middle curves of figure 3.19).

The ion signal measured by the Faraday cup V_s and the electron current I_b have not the same variations. A shape discrepancy exists between V_s and I_b when they are plotted versus V_A, as kinetic energy varies, due to the total electron ionisation cross-section function, while not when V_s and I_b are plotted versus V_{Re}, as V_{Re} has only an effect on the focussing of electrons. In order to understand these variations, further experimentation was carried out.

3.5 Result comparisons

3.5.1 Between filament and GDES experimental results

The current I_b and I_{Re} measured with filament (figure 3.14) and with GDES (figure 3.19) show the same variation. The differences could be induced by the range of kinetic energies for GDES.

Although several operating conditions are different (the local pressure, the intensity of the emitted electron etc), a comparison between filament and GDES is done and summarised in table 3.2.

Confidential

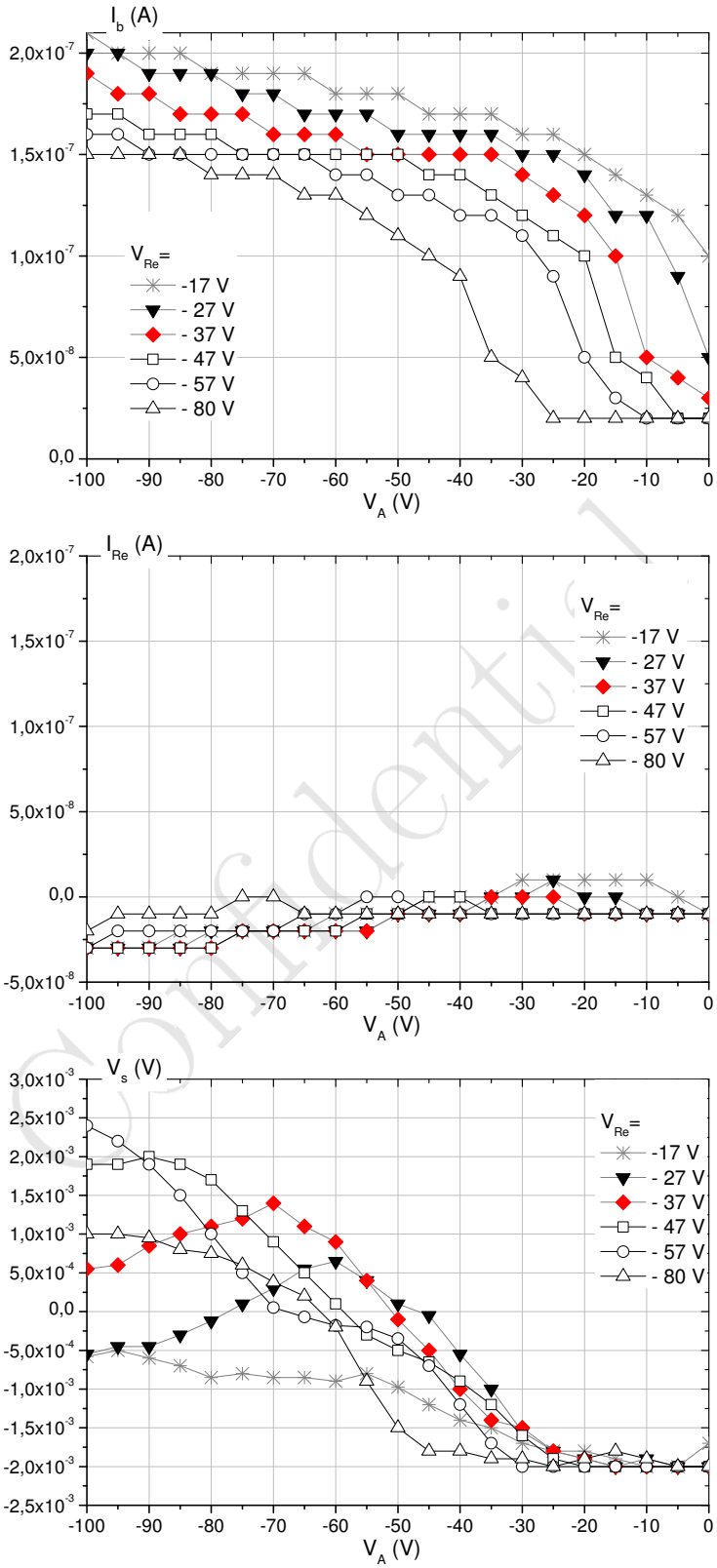

Figure 3.18: Electron currents measured at the ion cage (top) and repeller (middle). Faraday cup detector ion signal (bottom) *versus* potential applied to anode for different values of potential applied to repeller.

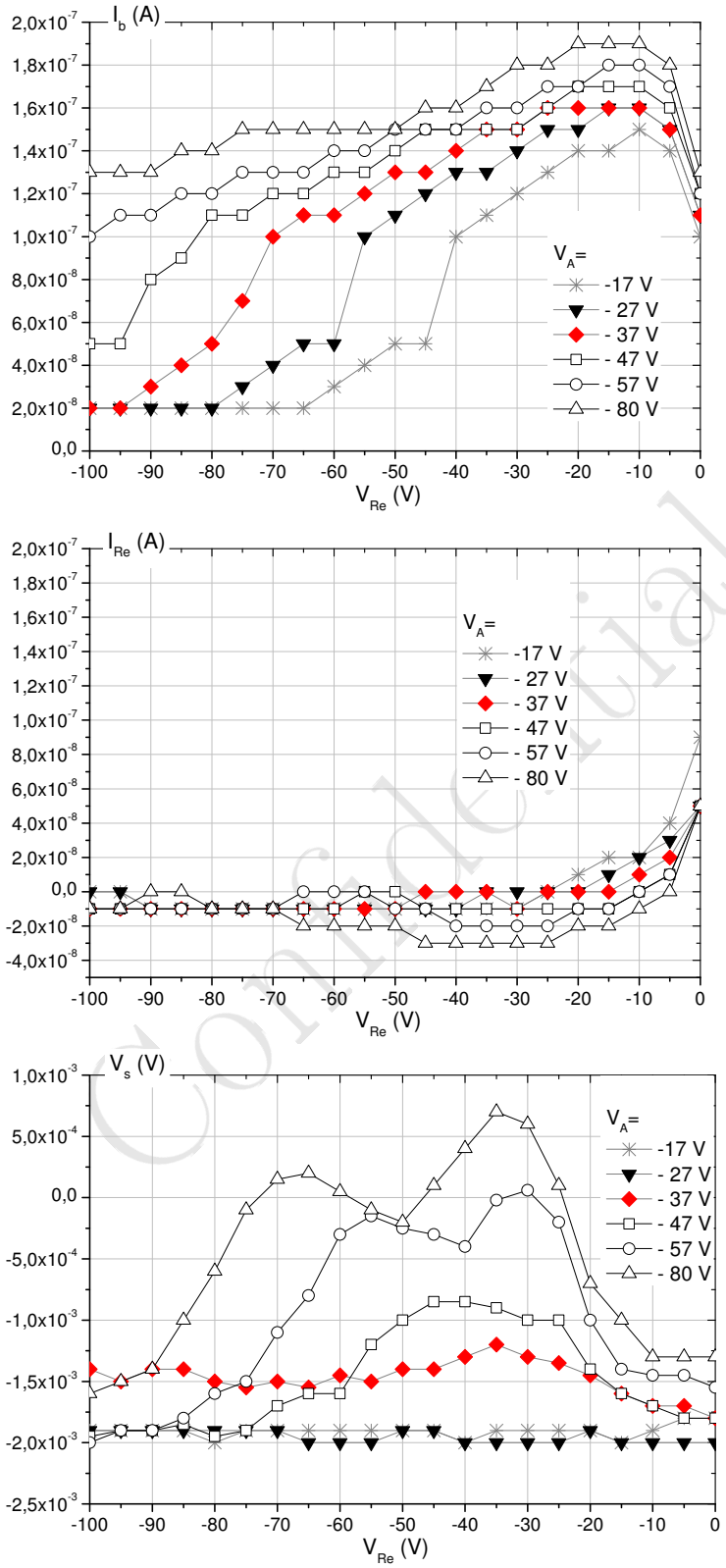

Figure 3.19: Electron currents measured at the ion cage (top) and repeller (middle). Faraday cup detector ion signal (bottom) *versus* potential applied to repeller for different values of potential applied to anode.

To conclude, the current I_b is four orders of magnitude smaller with the GDES cell than with a filament, while the ion detected signal V_s is only two orders of magnitude smaller. If we compare these two values per Watt, I_b/P is three orders of magnitude the smaller, while V_S/P is only 2.6 times smaller.

3.5.2 Between GDES experimental and simulation results

Further simulations were performed with a distance separating the GDES and the EI source equal to 10^{-3} m as in experiment. This distance has a great influence on the electron focussing. We compute the electron currents at the ion cage only I_{IC}, at the ion cage and extract lens I_b (representing the current I_b measured in the experiments), and at the repeller *versus* the potential applied to the anode (figure 3.20). These currents are calculated by taking into account different ranges of kinetic energies of electrons at the anode orifice.

The current at the repeller is null as in experiment only for the low values of the maximal kinetic energy, *i.e.* for the ranges 0-10 and 0-20 eV.

In figure 3.21 experimental and simulation data are compared: the currents I_b and I_{Re} and the ion signal V_s versus the potential applied to the anode. The best fit is obtained for the low values of the maximal kinetic energy, *i.e.* for the ranges 0-10 and 0-20 eV.

3.6 Conclusion

It is possible by adjusting the potential applied to the anode (with respect to the potential applied to the ion cage) to have the all of the electrons in the ion cage with kinetic energies corresponding to the maximal values of the ionisation cross-section of the targeted molecules. Comparisons between experimental and simulation data confirm that the electron kinetic energy at anode orifice ranges from zero to 10-20 eV.

An ion signal at the Faraday cup detector has been measured with high sensitivity, if we compare the results recorded with the filament and the GDES cell. That confirms that the narrow dispersion of kinetic energies makes the all of the electrons have the highest cross section for ionisation, in spite of a small number of electrons available at the anode orifice of GDES and, consequently, at the ion cage. Moreover, certainly the number of electrons available for ionisation is too important in the source when using the filament and then impairs the detection.

In conclusion to experimental and simulation tests, the GDES/EI source coupling is operating. This is a low-temperature (reducing desorption phenomena) and a low-power source of electrons requiring 0.2 W to operate that a handled mass spectrometer can employ. Tests with a mass spectrometer will be done to investigate molecule identification, in the following.

Confidential

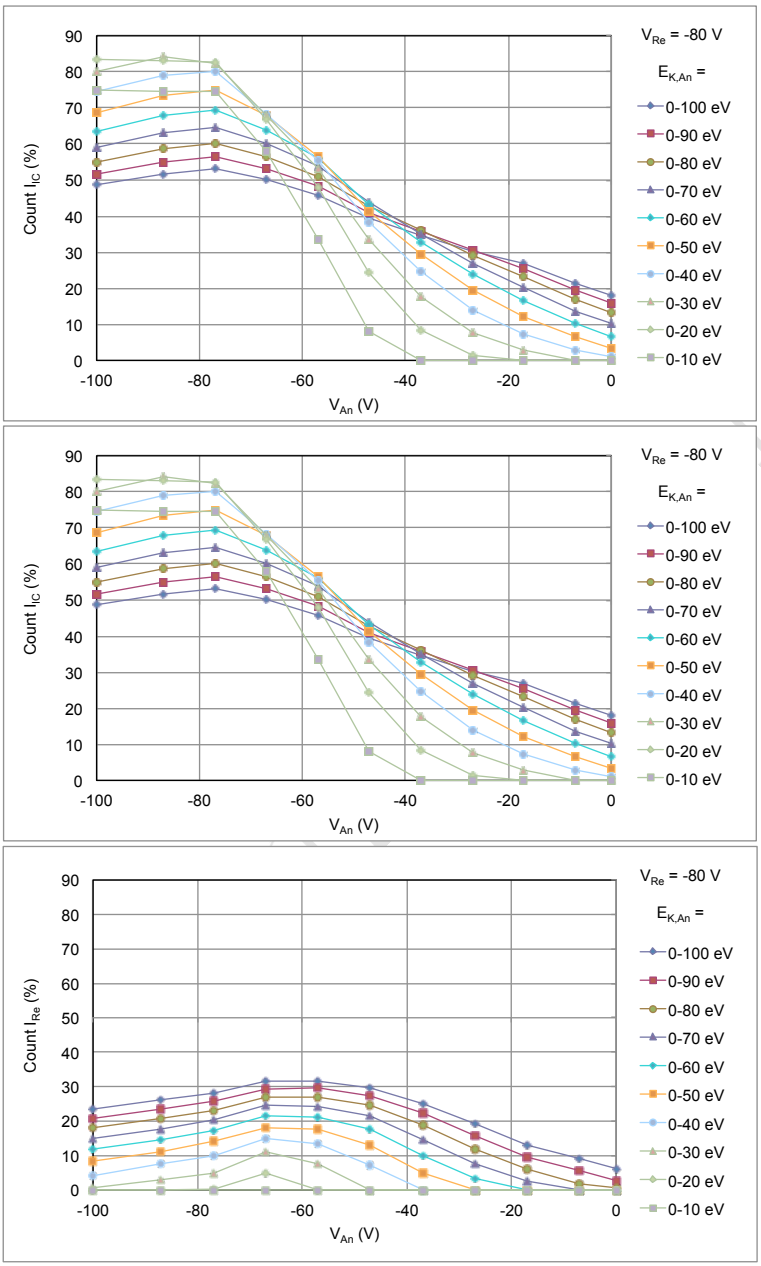

Figure 3.20: Simulation: electron currents at the ion cage I_{IC}, at the ion cage and extract lens I_b, and at the repeller I_{Re} versus the potential applied to the anode for different ranges of electron kinetic energy at the anode orifice.

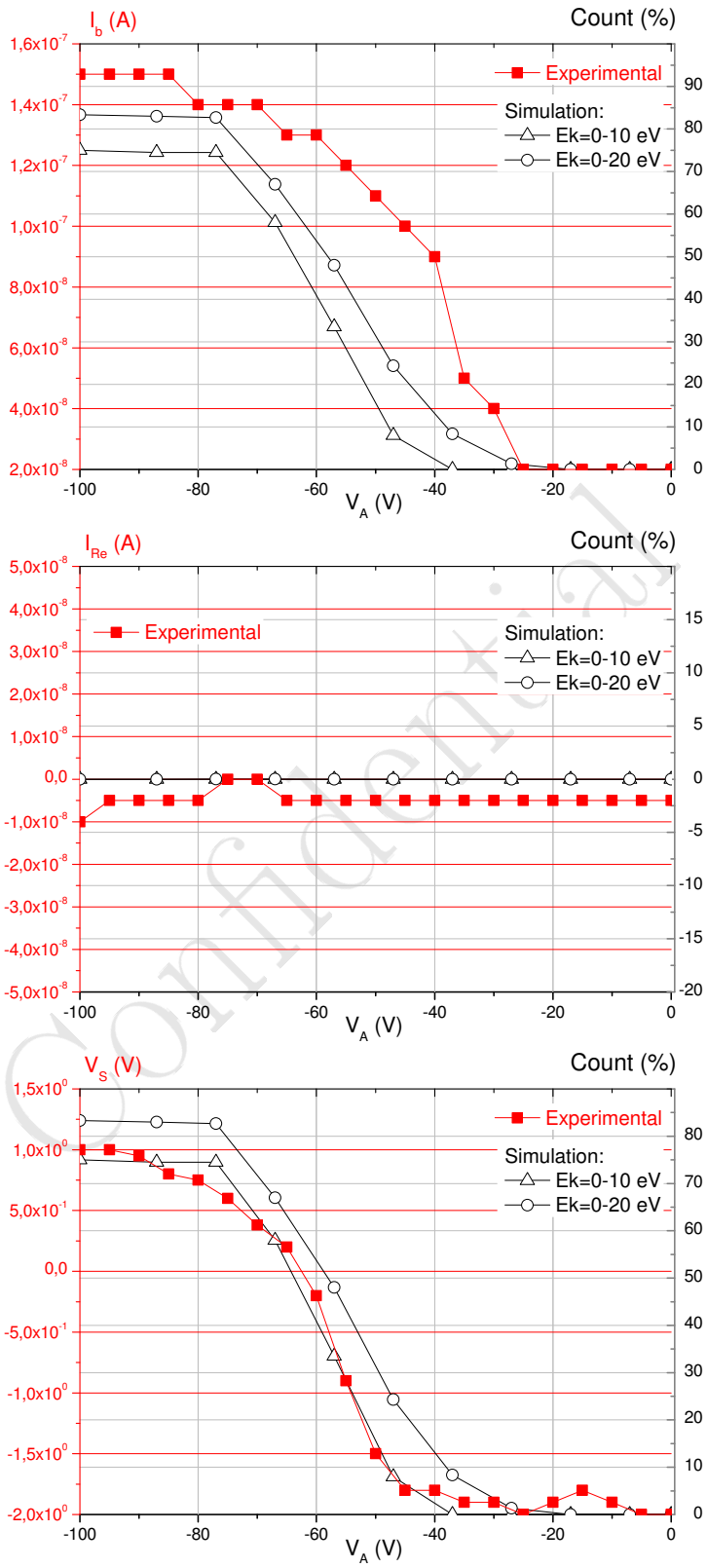

Figure 3.21: Experimental and simulation data:

Part II
Ion injection and confinement in a Linear Ion Trap

Confidential

Confidential

Chapter 4

Theoretical aspects of quadrupole fields

The linear ion trap (LIT) used consists of a quadrupole mass filter (QMF) and two lenses or electrodes on both ends. We will separate the contribution of the potentials induced by rods of the mass filter and by the two end-electrodes.

4.1 The mass filter

4.1.1 2D quadrupole potential and mass filter design

A pure 2D quadrupolar potential is expressed by the equation [70, 71, 72, 73, 74, 75, 76, 77, 78]:

$$\phi(x, y) = \alpha x^2 + \beta y^2 \tag{4.1}$$

This potential must satisfy the Laplace equation: $\triangle\phi(x, y) = 0$. As a consequence, $\alpha + \beta = 0$. The potential is then written:

$$\phi(x, y) = \frac{A}{r_0^2}\left[x^2 - y^2\right] + B \tag{4.2}$$

where A and B are potentials, and r_0 is a distance.

With DC potential values, such a potential distribution is attractive one direction and repulsive in the other direction for an ion. An RF potential is required to invert periodically the electric force in each of the two directions of the radial plane. As a consequence, an ion can be maintained in both directions of this plane around the centre of the radial plane. Under certain conditions (amplitude, initial energy), ion can oscillate in $x0y$ plane, with finite amplitude trajectories.

Furthermore, in the radial plane, the equipotential lines are hyperbolas. The inner side of the four mass-filter electrodes are the four equipotential lines located at r_0, the smallest distance separating an electrode from the centre. So, the quadrupole mass filter consists of a set of four electrodes, ideally of hyperbolic cross section, that are accurately positioned in the radial plane $(x0y)$ and arranged about the central axis, the $0z$-direction (see figure 4.1).

Confidential

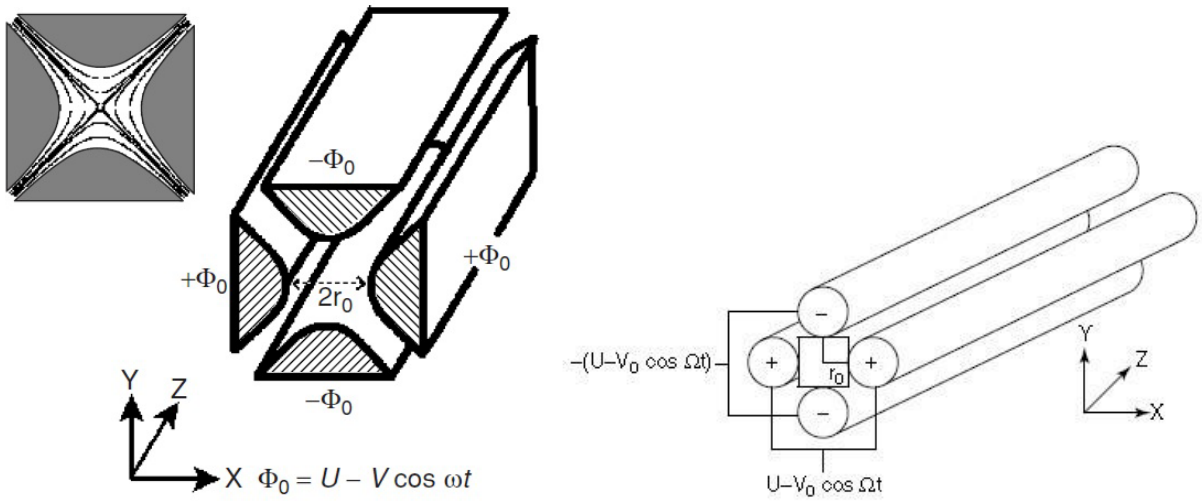

Figure 4.1: (Right) The ideal quadrupole mass filter electrodes having the hyperbolic cross section and with the equipotential lines for a quadrupole field (From [58]). (Left) Mass filter with cylindrical rod and potentials applied to the rods (From [76]).

For mechanical manufacturing and also economic reasons, most mass filters employs four electrodes (rods) of circular cross section, see figure 4.1, but with the hyperbolic electrodes, a better resolution was obtained [79].

The parameters A and B are calculated from the potential applied to the four electrodes. For instance, $V(t) = U_0 + V_0 \cos(\Omega t)$ is applied to the pair of opposite electrodes of the $0x$-direction and $-V(t)$ is applied to the pair of opposite electrodes of the $0y$-direction, with Ω, the frequency of RF voltage in rad/s:

$$\begin{aligned} \phi(r_0, 0) &= \frac{A}{r_0^2}\left[r_0^2\right] + B = V(t) \\ \phi(0, r_0) &= \frac{A}{r_0^2}\left[-r_0^2\right] + B = -V(t) \end{aligned} \tag{4.3}$$

That leads to:

$$\begin{aligned} A &= V(t) \\ B &= 0 \end{aligned} \tag{4.4}$$

The potential in the mass filter is then expressed by:

Confidential

$$\phi_{QMF}(x,y,t) = \frac{V(t)}{r_0^2}\left[x^2 - y^2\right] \tag{4.5}$$

More generally, a 2D potential verifying the Laplace equation, can be expanded in multipoles as [80, 81]:

$$\phi_{QMF}(x,y,t) = V(t)\sum_{j=0}^{+\infty} A_j \Re\left[\left(\frac{x+iy}{r_0}\right)^j\right] \tag{4.6}$$

where A_j is a dimensionless parameter depending on the potential values at boundaries. The geometric differences (desired or no) to the pure quadrupolar form are taken into account in this equation.

4.1.2 The ion motion

The motion of a single ion is derived from the equation, assuming that the ion incurs only the electric field from the electrical potential :

$$m\overrightarrow{\gamma} = q\overrightarrow{E} = -Ze\overrightarrow{\nabla}\phi_{QMF}(x,y,t) \tag{4.7}$$

were γ is the acceleration, Z is the number of charge and m the mass of the ion.

The equations in each Cartesian direction are :

$$\frac{d^2x}{dt^2} + \frac{2Ze(U_0 + V_0\cos(\Omega t))}{mr_0^2}x = 0 \tag{4.8}$$

$$\frac{d^2y}{dt^2} - \frac{2Ze(U_0 + V_0\cos(\Omega t))}{mr_0^2}y = 0$$

$$\frac{d^2z}{dt^2} = 0$$

In the radial plane, using appropriated reduced parameters:

$$a_x = -a_y = \frac{8ZeU_0}{mr_0^2\Omega^2} \tag{4.9}$$

$$q_x = -q_y = \frac{-4ZeV_0}{mr_0^2\Omega^2}$$

$$2\tau = \Omega t$$

the motion equation becomes a Mathieu equation:

Confidential

$$\frac{d^2u}{d\tau^2} + (a_u - 2q_u \cos 2\tau)u = 0 \tag{4.10}$$

where u is one of the $0x$- and $0z$-directions.

4.1.3 Motion stability and stability diagram

The Mathieu equation leads to stable and unstable solutions for the ion motion. An ion has a finite displacement with oscillations around the 0z axis if its motion is stable, otherwise its amplitude have an exponential increase according a direction of the radial plane. The stable motion is effective inside zones in the plane (a_x, q_x), see figure 4.2, [82]. The stability zones in the $0y$-direction are deduced from those in the $0x$-direction by symmetry.

The ion motion must be stable in both directions. The intersections of the stability zones in each direction give the stability zones of the mass filter. The first zone (or main stability diagram) is interesting as lower amplitudes for the confinement voltages are required. The higher limit of the main stability diagram is at $a_x = 0$ and $q_x = 0.908$ and the apex is at $a_{x,apex} = 0.237$ and $q_{x,apex} = 0.707$. Higher resolutions can be attained with the other zones (for example, see [83, 84, 85, 86, 87, 88]).

Finally, even with a stable motion, the maximal extension of the ion radial displacement must not exceed the limits of the mass filter fixed by the electrodes in order to be transmitted successfully the ion motion. Motion extension depends on the initial conditions of the radial positions and velocities of the ion when it enters the mass filter. So, the ions enter and cross in the z-direction, and oscillate in the xy-plane. This oscillation is the property of the mass-to-charge ratio of ions, the potential applied and the dimension of the mass filter.

4.1.4 Stability diagrams in (U_0, V_0) plane and mass spectrometry analysis

In (U_0, V_0) plane and under a set of same operating conditions (r_0 and Ω), each masse-to-charge ratio has a stability diagram (figure 4.3). The smallest mass has the smallest stability diagram. This is the basis of operation of the mass analyser. With $U_0 = 0$, it operates as a high-pass mass filter, denoted as RF only mode. Near the apex, it operates in a selective ion mode, denoted as Single Ion Monitoring mode (SIM). A scan line with an appropriate U_0/V_0 ratio passing by the apex of each stability diagram is used for sequential mass analysis over large mass ranges [89].

There is a trade-off between sensitivity and resolution depending on where the scan line intercepts the apex of the stability diagram. Closer to the apex the resolution is higher. The resolution can be expressed by:

$$R_{max} = \frac{m/z}{\Delta(m/z)} \propto \frac{L^2.V_0}{Ze.v_z.r_02} \tag{4.11}$$

where $Ze.v_z$ represent the initial kinetic energy of ions according to Oz axis, L, the rod length and V_0, the maximum amplitude of the RF voltage. Typically, mass separation is about m/z: 1 over a

Confidential

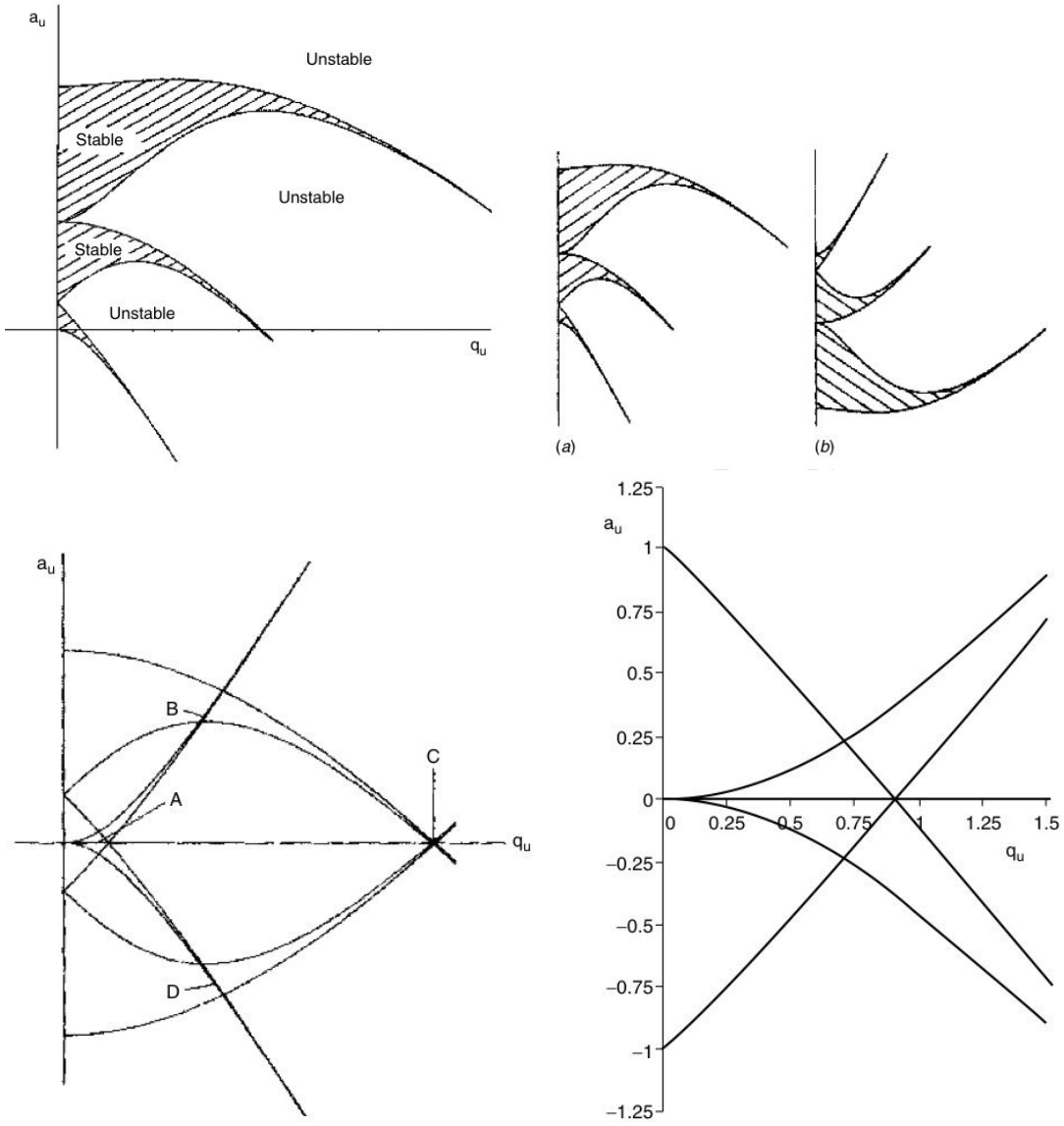

Figure 4.2: (From left to right and from top to bottom) Three stability zones of the Mathieu equation. Three stability zones of the Mathieu equation for the directions 0x (a) and 0y (b). First zones of stability of the mass filter. Zoom on the first stability diagram (From [76]).

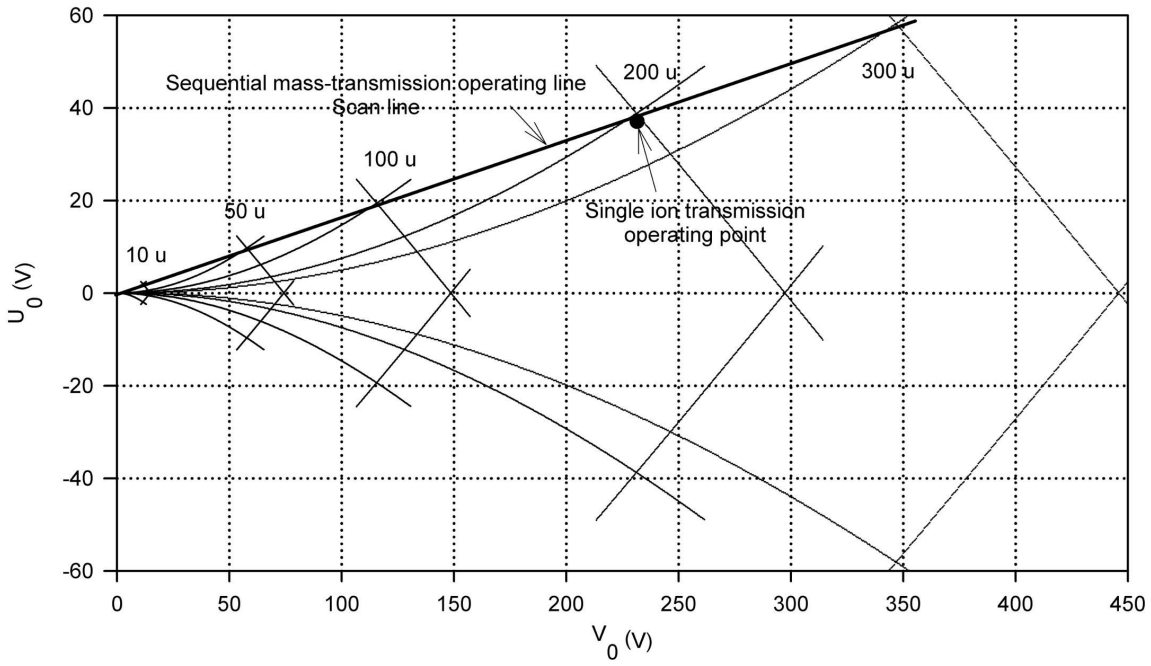

Figure 4.3: Principal stability diagrams of a QMF for m/z: 10, 50, 100, 200 and 300 in (U_0, V_0) plane, for $r_0 = 4\text{x}10^{-3}$ m and $\Omega/2\pi = 10^6$ Hz.

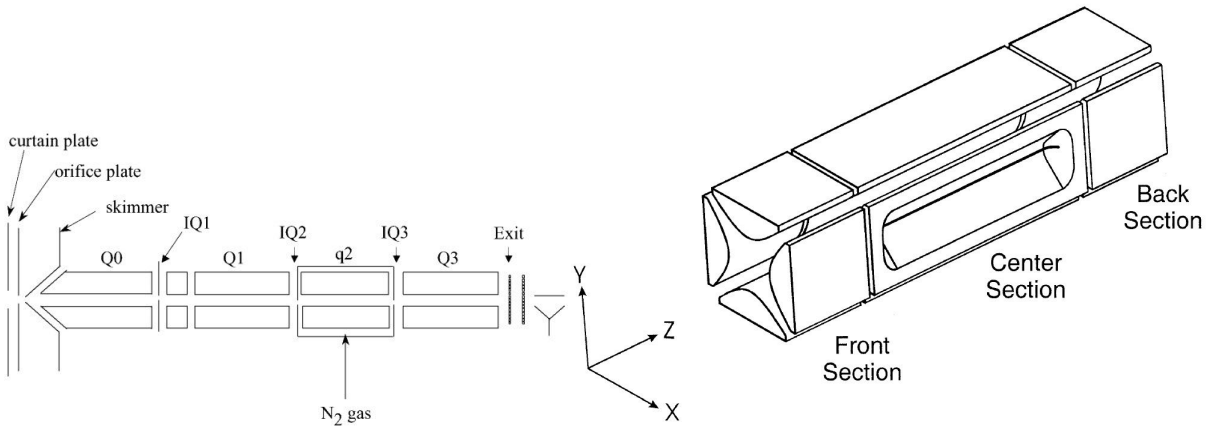

Figure 4.4: Basic design of two-dimensional linear ion traps. On the left, the linear ion trap mass spectrometer was created from a triple quadrupole mass filter [90]. On the right, a quadrupole structure with hyperbolic rod cut into three axial sections [91].

mass range of m/z: 200-300. The transmission is high, however it is a function of $\frac{m/z}{\triangle(m/z)}$ so it rapidly decreases with increasing mass.

4.2 The Linear Ion Trap

4.2.1 Introduction

A linear ion trap or two-dimensional (2D) linear ion trap is a mass filter with at both ends two end-electrodes. These end-electrodes can be either mass-filters of short length or simple lenses: they are denoted as entrance and exit filters or lenses. The linear trap can confine ions radially by DC and AC electrical potentials (as a mass filter) and axially by a static electrical potential applied between the end-electrodes. The advantages of LIT include a reduced space charge effect, a better ion trapping efficiency and a large ion storage volume, compared to the 3D Paul trap.

Hager *et al* modified the functionality of a triple mass filter instrument (figure 4.4). q2 or Q3 mass filter can be operated as linear ion trap using lenses at both ends and modifying the sequence of applied potentials [90]. Schwartz *et al*. proposed a quadrupole structure with hyperbolic rod profiles, each rod being cut into three axial sections (figure 4.4). The DC potential applied to the front and back sections allow containment of the ions along the axis in the central section, avoiding any possible fringe field distortions to the trapping and resonance excitation fields [91].

4.2.2 LIT and Mass spectrometry

Mass spectrometry in a LIT can be performed in different ways. Fourier transform mass spectrometry was demonstrated by Senko *et al.* [92, 93]. The ions are excited into a coherent motion, and then an image current induced by ion motion is detected for Fourier analysis. Detecting a weak

Confidential

image current in the presence of a high RF trapping field is challenging.

Schwartz *et al.* [91] described ion ejection out a slot in one of the rods using the mass selective instability mode of operation. Resonance ejection and excitation are used to enhance mass analysis and to allow isolation and activation of ions for $\mathrm{MS^n}$ capability. Improved trapping efficiency and increased ion capacity are observed relative to a three-dimensional (3D) ion trap with similar mass range.

Later, Hager *et al.* [94, 95] proposed to apply this technique to a LIT. Mass-selective axial ion ejection uses the coupling of the radial and axial motions in the exit fringing fields located in the vicinity of the simulation studies of ion injection in the LIT entrance and exit lenses. The fringing fields convert radial ion excitation into axial ejection. A further improvement uses an auxiliary voltage applied in a dipolar manner that is ramped in concert with the drive RF voltage for improving sensitivity (by increasing the number of ejected ions). Using this method, Qiao *et al.* [96] proposed the application of quadrupole DC voltage that appears to increase the ion cloud temperature, which lowers mass shifts measured on spectra due to space charge effects.

Moradian *et al.* [97] proposed the addition of octopole field to provide mass resolution and ejection efficiencies when mass selective axial ion ejection is performed in linear quadrupoles.

A LIT can be used for ion fragmentation in MS/MS experiment. For instance, Michaud *et al.* [98] showed that efficiencies ($\mathrm{N_2}$ collision gas) can be substantially higher with a linear ion trap with a 4 % added octopole field than with a conventional rod set.

Douglas *et al.* [99] studied mass selectivity and resolution of a LIT operating with dipolar excitation of ions for either axial or radial ejection. A short time later the same authors also proposed the study the influence of the higher multipoles introduced to the electric potential by round rods on the ion ejection process [100]. They have therefore investigated the optimum ratio of rod radius to field radius for excitation and ejection of ions. Remes *et al.* [101] proposed a new methodology accelerating ion trajectory modelling for the simulation of mass analysis of ions in RF traps. The comprehensive characterization of the effects on peak shape and resolution of electrode features was demonstrated. Simulation results were compared to those from a real commercial linear ion trap instrument. Several of the modelled trap configurations indicated a possible improvement of resolution.

Confidential

4.2.3 Potential

The potential in the LIT is the superposition of two potentials induced by four hyperbolic rods $\phi_{QMF}(x, y, t)$ and two end-cap electrodes $\phi_e(x, y, z)$:

$$\phi(x, y, t) = \phi_{QMF}(x, y, t) + \phi_e(x, y, z) \tag{4.12}$$

Considering its development to the quadrupole order and a value different from zero in the centre of the LIT, the potential induced by the two end-caps can be expressed by [102, 103]:

$$\phi_e(x,y,z) = C + \frac{kU_e}{z_0^2}\left[z^2 - \frac{x^2+y^2}{2}\right] + ... \tag{4.13}$$

The constant potential is attractive in the axial direction while it is repulsive in the radial plane. The motion equations become:

$$\frac{d^2x}{dt^2} + \left(\frac{2Ze(U_0 + V_0\cos(\Omega t))}{mr_0^2} - \frac{ZekU_e}{mz_0^2}\right)x = 0 \tag{4.14}$$

$$\frac{d^2y}{dt^2} - \left(\frac{2Ze(U_0 + V_0\cos(\Omega t))}{mr_0^2} + \frac{ZekU_e}{mz_0^2}\right)y = 0$$

$$\frac{d^2z}{dt^2} + \frac{2ZekU_e}{mz_0^2}z = 0$$

and the Mathieu parameters are modified:

$$\tilde{a}_x = \frac{8ZeU_0}{mr_0^2\Omega^2} - \frac{4ZekU_e}{mz_0^2\Omega^2} \tag{4.15}$$

$$\tilde{a}_y = -\frac{8ZeU_0}{mr_0^2\Omega^2} - \frac{4ZekU_e}{mz_0^2\Omega^2}$$

$$\tilde{a}_z = \frac{8ZekU_e}{mz_0^2\Omega^2}$$

$$q_x = -q_y = \frac{-4ZeV_0}{mz_0^2\Omega^2}$$

$$2\tau = \Omega t$$

The defocusing effect in both radial directions induced by the both end-electrodes leads to a stability diagram different from that of the quadrupole mass filter [104].

Confidential

Confidential

Chapter 5

Operating conditions for simulation

5.1 Device design

For a pratical LIT design, we take into account the geometrical optimisations of the lenses described in a published work concerning the optimisation of the ion source lens system coupled to the LIT [17]. The general CPO design of the device with electrode location is shown in figure 5.1. In this case LIT-50 corresponds to $z_0 = 25\text{x}10^{-3}$ m, the half length of LIT, with $r_0 = 4\text{x}10^{-3}$ m, the smallest distance separating an electrode from the centre, and $l_0 = z_0 + 10^{-3} = 26\text{x}10^{-3}$ m, the distance separating the centre of LIT to the end-cap electrode. Other LITs were also been simulated with only different values of z_0: LIT-8, LIT-20, LIT-30, LIT-40 and LIT-60.

Increasing the segmentation of the electrodes increases the accuracy of the Boundary Element Method used by CPO to compute the potential. For that reason, depending on the simulation studies, only the part of the device having an influence upon the electron or ion trajectories has been simulated in order to have the highest number of segments imposed by the program.

Confidential

5.2 Potential configurations for the mass filter electrodes

Different potential configurations can be employed to confine ions. The table 5.1 summarise the potential applied to the electrodes of the mass-filter, the potential inside the mass filter and the reduced parameters associated to the Mathieu equation for three different potential configurations.

The configuration #1 is the standard potential configuration, the potential $V(t) = U_0 + V_0 \cos(\Omega t)$ is applied to the pair of opposite electrodes on the $0x$-direction and $-V(t)$ is applied to the pair of opposite electrodes on the $0y$-direction (see previous part).

With the objective of reduced power consumption and weight, in the final prototype, only one AC RF power supply was used. In the configuration #2, the potential $V(t) = U_0 + V_0 \cos(\Omega t)$ is applied to the pair of opposite electrodes on the $0y$-direction, while the pair of opposite electrodes on the $0x$-direction are grounded. This configuration is not interesting as the centre of the trap is always at U_0 leading to off-centring the ions at injection. In the configuration #3, the potential

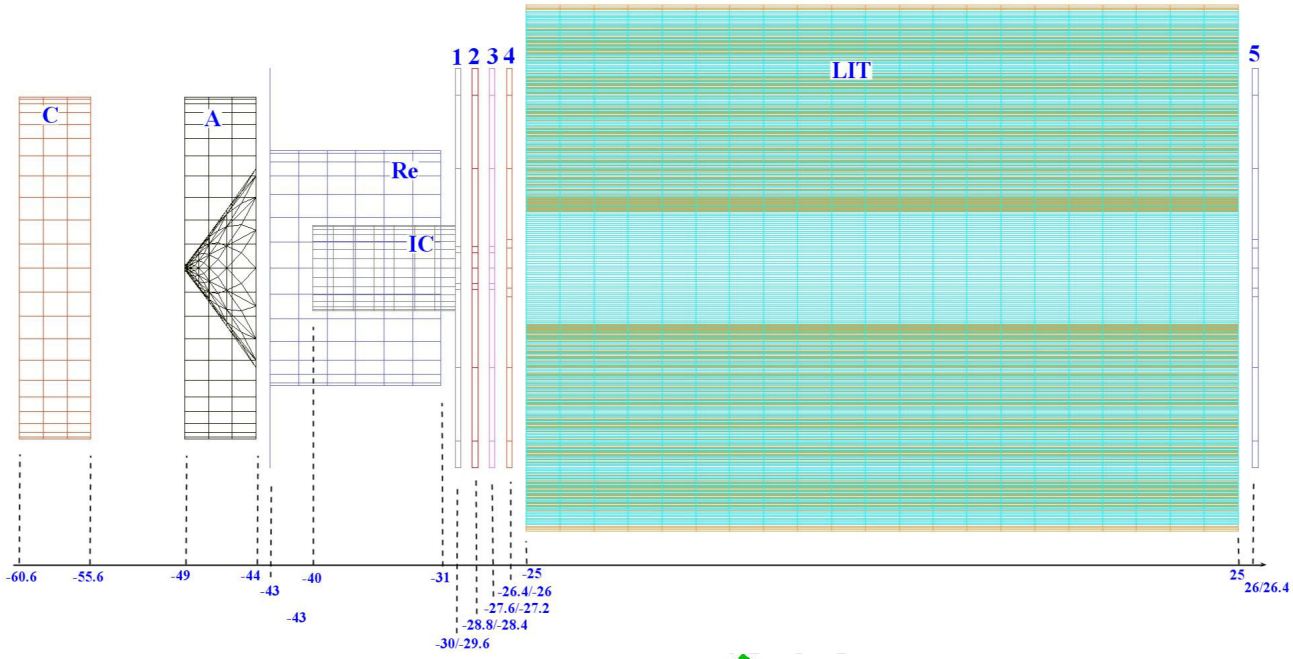

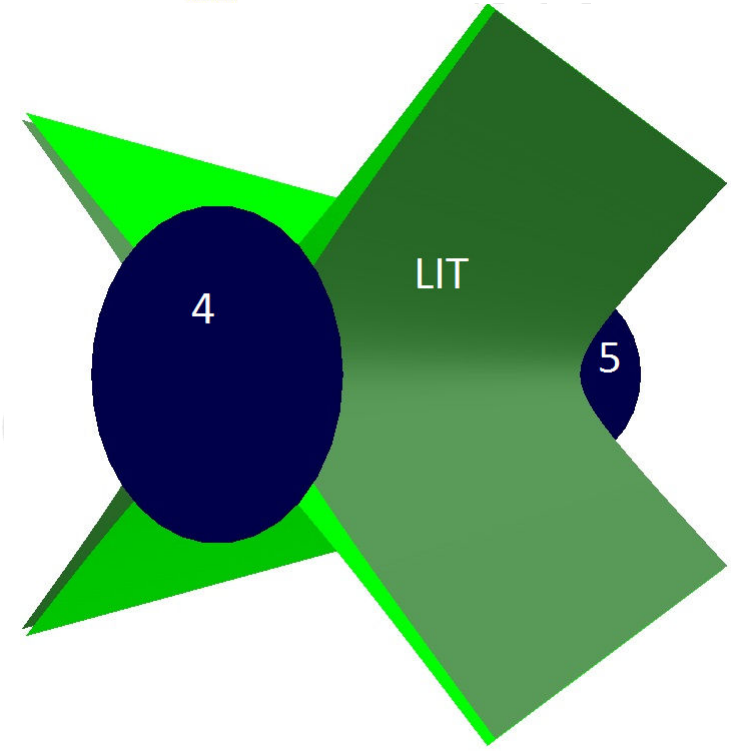

Figure 5.1: (Top) General CPO 2D (ZX plane) design with electrode location (in mm), including, from left to right, GDES cathode and anode, repeller (Re), ion cage (IC), (1) extraction lens, (2) focussing lens, (3) decelerating lens, (4) entrance lens, LIT-50 and (5) exit lens. CPO design 3D view including only entrance and exit lenses and LIT. (Bottom) CPO 3D design with LIT, entrance (4) and exit (5) end-caps.

	Configuration #1	Configuration #2	Configuration #3
x-electrode	$-U_0 - V_0\cos(\Omega t)$	0	$-U_0$
y-electrode	$U_0 + V_0\cos(\Omega t)$	$U_0 + V_0\cos(\Omega t)$	$U_0 + V_0\cos(\Omega t)$
$\phi_{QMF}(x,y,t)$	$[U_0 + V_0\cos(\Omega t)]\left[\frac{x^2-y^2}{r_0^2}\right]$	$\frac{U_0 + V_0\cos(\Omega t)}{2}\left[\frac{x^2-y^2}{r_0^2}\right]$ $+\frac{U_0 + V_0\cos(\Omega t)}{2}$	$\left[-U_0 - \frac{V_0\cos(\Omega t)}{2}\right]\left[\frac{x^2-y^2}{r_0^2}\right]$ $+\frac{V_0\cos(\Omega t)}{2}$
Reduced parameters	$a_x = -a_y = \frac{8ZeU_0}{mr_0^2\Omega^2}$ $q_x = -q_y = -\frac{4ZeV_0}{mr_0^2\Omega^2}$	$a_x = -a_y = \frac{4ZeU_0}{mr_0^2\Omega^2}$ $q_x = -q_y = -\frac{2ZeV_0}{mr_0^2\Omega^2}$	$a_x = -a_y = -\frac{8ZeU_0}{mr_0^2\Omega^2}$ $q_x = -q_y = \frac{2ZeV_0}{mr_0^2\Omega^2}$

Table 5.1: Potential applied to the rods during confinement, 2D potential and reduced parameters of Mathieu equations.

$V(t) = U_0 + V_0\cos(\Omega t)$ is applied to the pair of opposite electrodes on the $0y$-direction and the DC potential $-U_0$ is applied to the pair of opposite electrodes on the $0x$-direction. In this manner, over a period of the RF field, the average value of the potential in the centre of the trap is zero.

Simulations were performed at different initial phases, φ of the RF confinement field. So the applied AC potential must be written as: $V_0\cos(\Omega t + \varphi)$.

The initial phases of the RF voltage are chosen equal to 0, $\pi/2$, π and $3\pi/2$ for the configuration #3; and equal to 0 and $\pi/2$ for the configuration #1 assuming that the drawings are statistically the same on x and y-directions. Rather, these phases are related to the function $V_0\sin(\Omega t + \varphi)$ used in CPO software.

The ion injection and confinement in the LIT are tested for the configurations #1 and #3 of confinement potentials. To study the motion stability according to the potential configuration, a same operating point must be chosen. For instance, at the QMF apex, the potential values $U_{0,apex}^{QMF}$ and $V_{0,apex}^{QMF}$ are calculated by the formula:

$$U_{0,apex}^{QMF} = \frac{0.237 r_0^2\Omega^2}{8e} \times \frac{m}{Z}$$

$$V_{0,apex}^{QMF} = \frac{0.707 r_0^2\Omega^2}{4e} \times \frac{m}{Z} \text{ for configuration \#1} \tag{5.1}$$

$$V_{0,apex}^{QMF} = \frac{0.707 r_0^2\Omega^2}{2e} \times \frac{m}{Z} \text{ for configuration \#3}$$

Confidential

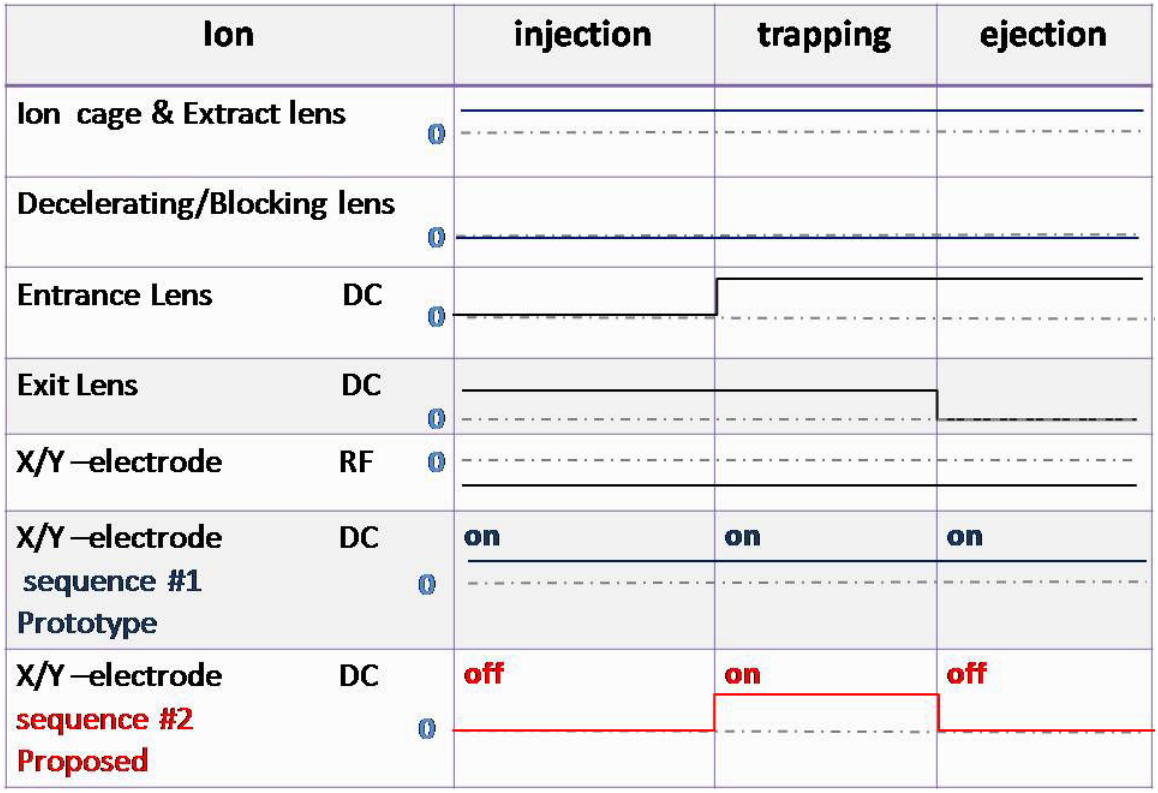

Figure 5.2: Detail of the "single ion monitoring", SIM.

5.3 Single Ion Monitoring operating mode sequences

The operating mode Single Ion Monitoring is employed in the prototype “LIT designed for the SNIFFLES project”. As merely 3-to-4 ion fragments having apart mass values are targeted, a succession of Single Ion Monitoring sequences (one sequence per ion) can be used reducing analysis time and increasing sensitivity [17]. The single ion monitoring sequence refers to: (1) Injection of ions created in the EI source, (2) LIT confinement, then (3) total ejection of the ions toward the detector. The LIT operates in a selective mode during injection, confinement and ejection. Some appropriate values of U_0 and V_0 can be used in the vicinity of the apex to have the shape of a pic associated to a targeted mass-to-charge ratio. Ion manipulation is performed by switching the DC potentials applied only to the entrance and exit lenses. This operating mode is denoted as “single ion monitoring” (SIM) operating mode (figure 5.2).

Typically, the ion source is coupled to a mass filter by means of an entrance lens having a smaller inner diameter than the inner diameter of the filter. The transmission efficiency was demonstrated by Brubaker and Tuul [105], and later, the filter acceptance was examined in term of phase space dynamics by Dawson [71, 106]. In 1968, Brubaker proposed the use of a pre-filter operating in a

RF only mode (i.e. with $U_0 = 0$) to greatly increase the number of injected ions [107, 108].

In our device, the entrance lens has a larger inner diameter. Moreover, the ions cross an instability zone between the lens and the trap reducing the injection efficiency. The LIT injection is tested for two different Single Ion Monitoring sequences, as described in figure 5.2. The SIM sequence #1 refers to the sequence used in the prototype. This sequence has been implemented for simplicity of manufacture, but it leads to a constant DC potentials applied to the electrodes during injection stage. Moreover, the ions cross an instability zone between the lens and the trap reducing the injection efficiency.

We propose to compare its injection efficiency results to those of the sequence #2 in which the DC confinement potential is applied only during confinement and switched to zero during injection leading to a RF only mode during ion injection stage (figure 5.2).

5.4 Ion injection stage conditions

The design used for testing injection is limited to the ion-blocking/decelerating lens, entrance lens, LIT-50 and exit lens (5.1).

The injection stage is studied with initial conditions drawn at the ion-decelerating lens. The total kinetic energy at decelerating lens is chosen equal to 3 eV, as the ion cage is at 3 V while the decelerating lens is at 0 V. The ion direction at the decelerating lens is chosen in a conical volume defined by the radius of the decelerating and entrance lenses equal to 10^{-3} and $2\text{x}10^{-3}$ m, respectively. The total initial kinetic energy is mainly distributed along $0z$ axis.

The entrance lens is biased at 0 V and the exit lens at 40 V (see table 5.2). The confinement potentials are applied on the LIT electrodes according to the configurations #1 and #3 during injection stage.

The initial number of ions in the CPO simulation is 50. The calculations were done with a constant temporal step. They represent a population of ions created at the same time. For that reason, some initial phases of the RF confinement potentials are used in simulations.

5.5 Ion confinement stage conditions

Only one ion is simulated according to injection conditions (positions, velocities). The potential applied to electrodes is summarized in table 5.3.

Confidential

Lenses	Applied potential (V)	
Extraction (1)	3	
Focusing (2)	0	
Decelerating (3)	0	
Entrance (4)	0	
Exit (5)	40	
Ion Cage	3	
LIT:	Configuration #1	Configuration #3
$\Omega/2\pi$	1 MHz	1 MHz
U_0	0	0
V_0	24.3	48.6

Table 5.2: Potentials applied to the electrodes during injection stage

Confidential

Lenses	Potential applied (V)	
Entrance (4)	40	
Exit (5)	40	
LIT:	Configuration #1	Configuration #3
$\Omega/2\pi$	1 MHz	1 MHz
x-electrode	$-U_0 - V_0 \sin(\Omega t + \varphi)$	$-U_0$
y-electrode	$U_0 + V_0 \sin(\Omega t + \varphi)$	$U_0 + V_0 \sin(\Omega t + \varphi)$

Table 5.3: Potential applied to the electrodes during confinement stage.

Chapter 6

Ion injection simulation results

The aim of these simulations is to determine a potential configuration at injection leading to the greatest number of injected ions to improve sensitivity. The portability of the mass spectrometer is taken into account: the RF confinement potential remains turned on during injection to simplify the realisation of the electrode supply device (ECU). The ion behaviour during the injection stage is simulated for determination of the position and velocity distributions of the injected ions. As during injection, on exit there is a continuous flow of ions, these distributions represent also the initial condition distributions of the ion cloud at the beginning of confinement.

In addition, the injection time is also identified in order to reduce the duration of the mass analysis sequence.

Confidential

6.1 Ion trajectories

In this chapter, the simulations are performed with an ion cloud of 100 ions with m/z: 86 and LIT-50. An example of trajectories of ions in the Cartesian coordinate system are shown in figures 6.1 and 6.2 for the two potential configurations and different initial phases of the RF voltage. The duration of the round trip never exceeds $6\text{x}10^{-5}$ s for the set of electrical configurations. The axial trajectories have large parts represented by a straight line over a range of about $-2\text{x}10^{-2}$ to $2\text{x}10^{-2}$ m around the centre (with the LIT extremities at $-2.5\text{x}10^{-2}$ to $2.5\text{x}10^{-2}$ m): the axial motion is assumed to have a constant velocity, except close to exit end-cap where the motion is almost zero. Velocity (slope) differences are due to non-linearity direction couplings at both end-cap electrodes.

As a consequence, motions are uncoupled over a large volume of the LIT.

6.2 Temporal ion distribution

Each curve of figure 6.3 represents the temporal evolution of a population of ions created at the same time, at t=0. The function describing each curve is denoted as $F_{\varphi_i}(t)$. The total number of ions can be computed by (1) integrating the function for t varying from 0 to t_{inj} (if we assume

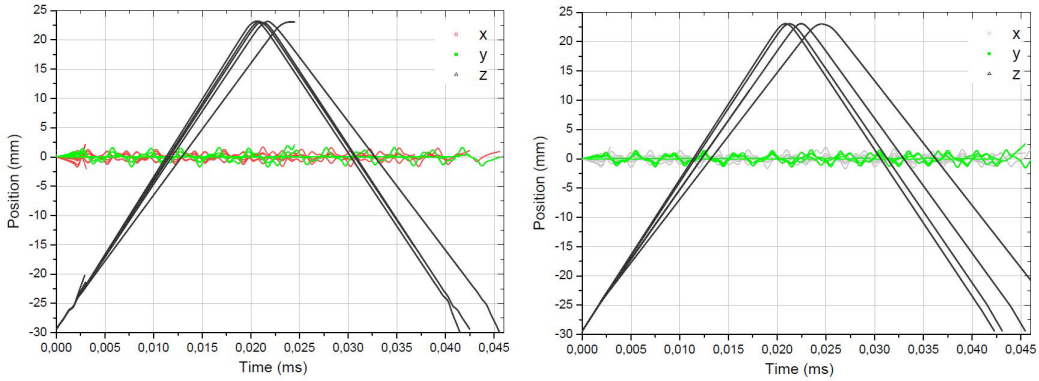

Figure 6.1: Some ion trajectories for each Cartesian coordinate versus injection time for configuration #1 and different initial phases of the RF voltage (from left to right, the phase equals 0 and $\pi/2$).

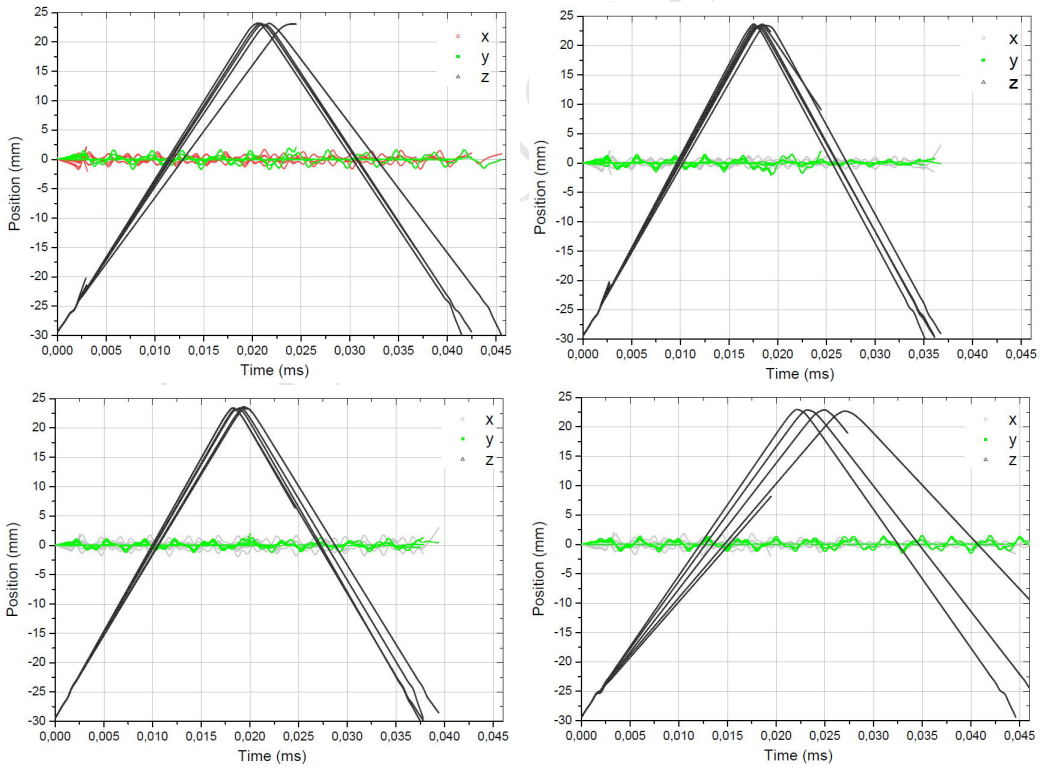

Figure 6.2: Some ion trajectories for each Cartesian coordinate versus injection time for configuration #3 and different initial phases of the RF voltage (from left to right and from top to bottom, the phase equals 0, $\pi/2$, π and $3\pi/2$).

that $F_{\varphi_i}(t)$ is zero at $t = t_{inj}$), (2) by integrating each function shifted to the right by u, for u varying from 0 to t_{inj} (to take into account all the instants of creation between 0 and t_{inj}, and (3) by summing the functions for the different RF phases.

The total number of ions at time t_{inj} can be then calculated from:

$$N(t_{inj}) \propto \sum_{\varphi_i} \int_0^{t_{inj}} \int_0^{t_{inj}} F_{\varphi_i}(t - \frac{\varphi_i}{\Omega} - u)\, dt\, du \tag{6.1}$$

The number of injected ions is an integral function of $F_{\varphi_i}(t)$. The maximal value is then obtained when $F_{\varphi_i}(t)$ is zero. As a consequence, it is not necessary that injection duration exceeds 0.06 ms. The total number of injected ions decreases quickly after about 0.03 ms (3 periods of the RF confinement voltage) due to fringing fields between the lens and the LIT and in the LIT in the vicinity of the entrance lens, leading to instabilities in the radial plane (figure 6.3). Then some plateaus are observed corresponding to three types of ion losses: 1) in the region of the entrance lens, 2) in the region of the exit lens and 3) in the region of the exit lens when ions leave the LIT. The number of ions is generally greater for configuration #1 than #3.

At the bottom of the figure 6.3 the dashed line represents the number of injected ions by continous flow, it can be estimated by:

$$N(t_{inj}) \propto \int_0^{t_{inj,max}} f(t_{inj} - u)\, du \tag{6.2}$$

For a punctual injection, the number of injected ions tends to zero at 0.06 ms, the minimum time required for injection.

6.3 Ion distribution in positions and velocities

The distributions in positions and velocities at the end of injection give a good estimation for the ion initial conditions in the trap for confinement. The ion trajectories are calculated for a population of ions created at the same time. It is assumed that the injection duration is sufficient to obtain a constant number of injected ions. Then, each point of a trajectory calculated with a constant time step can represent a set of ions present in the LIT. All the phases must be taken into account, as potentials applied to the device are not static.

Figures 6.4, 6.5 and 6.6 give the distributions in position. Figures 6.7, 6.8 and 6.9 give the distributions in velocity.

The radial distributions in position and velocity are zero-centred. The smallest dispersion is obtained for configuration #1. The wide dispersion of ions will induce a significant ion loss during trapping. The ion cooling by collision with a light buffer gas (He) can reduce this dispersion and the radial distribution tends to a Gaussian function determined by: $exp\left(-\frac{x-\bar{x}}{2\sigma_x^2}\right)$with x the value of

Confidential

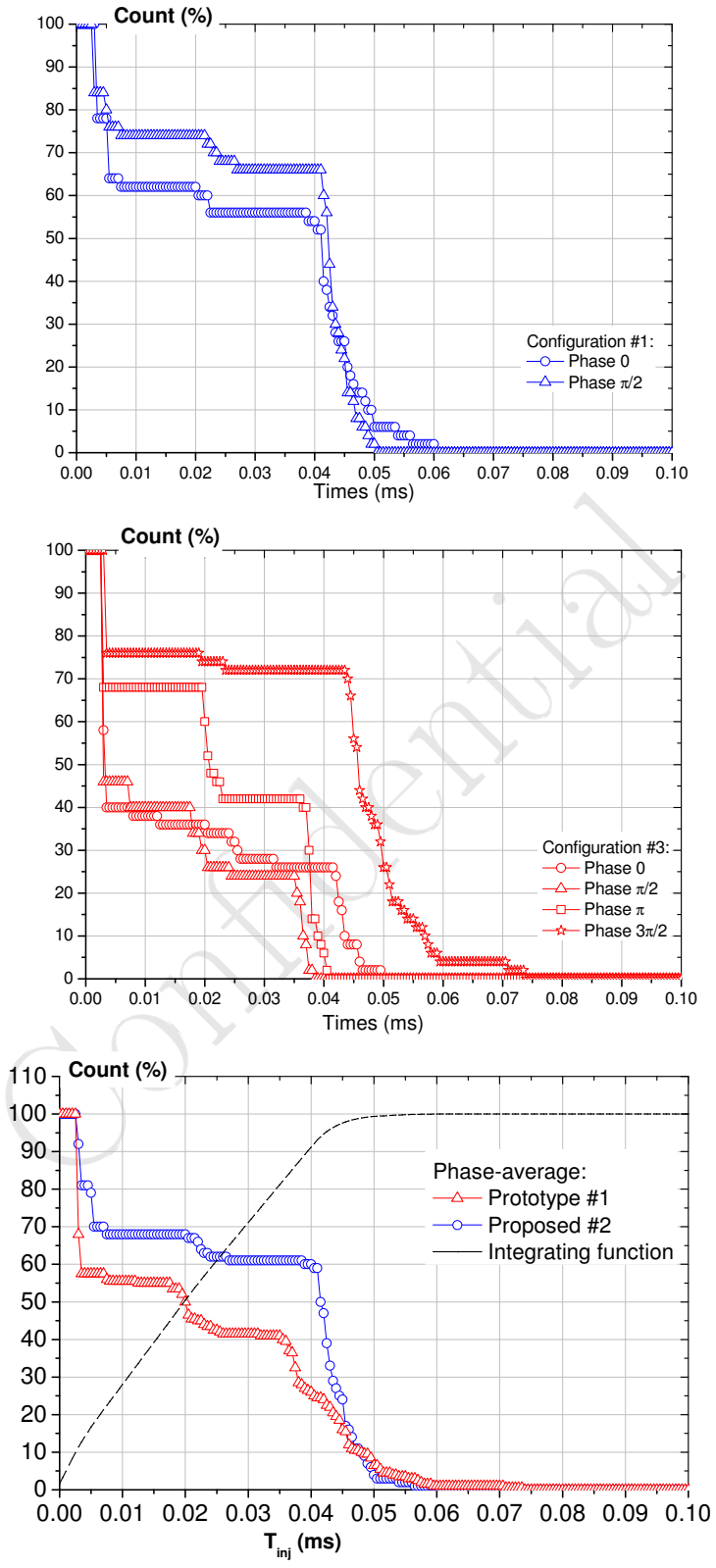

Confidential

Figure 6.3: Number of injected ions *versus* injection time for different initial phases of the RF voltage. (**Top**) configuration #1, (**middle**) configuration #3, and (**bottom**) the average value for both configurations.

the position and $\overline{x}$, the average value of ion density and $\sigma_x = 0.2.10^{-3}$ m, the maximal radius of ion cloud in x-direction, see the top of figure 6.4.

The axial position distribution is uniform excepted in the vicinity of the exit lens where the ion density is greater as ion velocities tend to zero.

The axial velocity distribution has two bands centred on + 2 500 and − 2 500 m/s representing an initial kinetic energy of 2.7 eV. The total initial kinetic energy has been chosen at 3 eV, due to a radial dispersion and energy exchange between directions, the value of the axial kinetic energy is then founded lower. The dispersion of velocity is about ± 500 m/s.

From distributions at steady-state of injection, the initial trapping conditions are obtained, as there is between injection and confinement.

6.4 Maximal number of injected ions

The total number of injected ions is calculated for two SIM sequences #1 and #2, and for two configurations #1 and #3, with 0, $\frac{\pi}{2}$, π and $\frac{3\pi}{2}$.

It is also important to compare the number of ions reaching the entrance end-caps after a round trip in the LIT. Indeed, these ions will be necessarily trapped when confinement is switched on. The number of ions is compared for the two electrical configurations and the two SIM operating modes in table 6.1.

Combining SIM sequence #2 and confinement potential configuration #1 gives the highest number of injected ions. However, the configuration #1 requires an additional power supply, and the sequence #2 requires to switch to zero the DC potential during trapping. The number of injected ions can be increased using a buffer gas by reducing the ion kinetic energy.

6.5 Conclusion

The distributions of positions and velocities of the ions at the beginning of confinement are estimated. It is not necessary to have large injection times to increase the number of ions. The injection time can be reduced to one hundred microseconds leading to shorter sequence times for mass analysis.

The potential of configuration #1 leads to higher numbers of ions than configuration #3 and the single ion monitoring sequence #2, too. The number of ions can be increased by a factor 2 by using either the potential configuration #1 or the sequence #2, and by a factor 3 by using both the potential configuration #1 and the sequence #2.

It is recommended to use the single ion monitoring mode with sequence #2 and a confinement of potential configuration #1 for the best improvements. However, the configuration #1 requires an additional power supply and the sequence #2 requires to switch to zero the DC confinement potentials during injection (RF only mode at injection).

Confidential

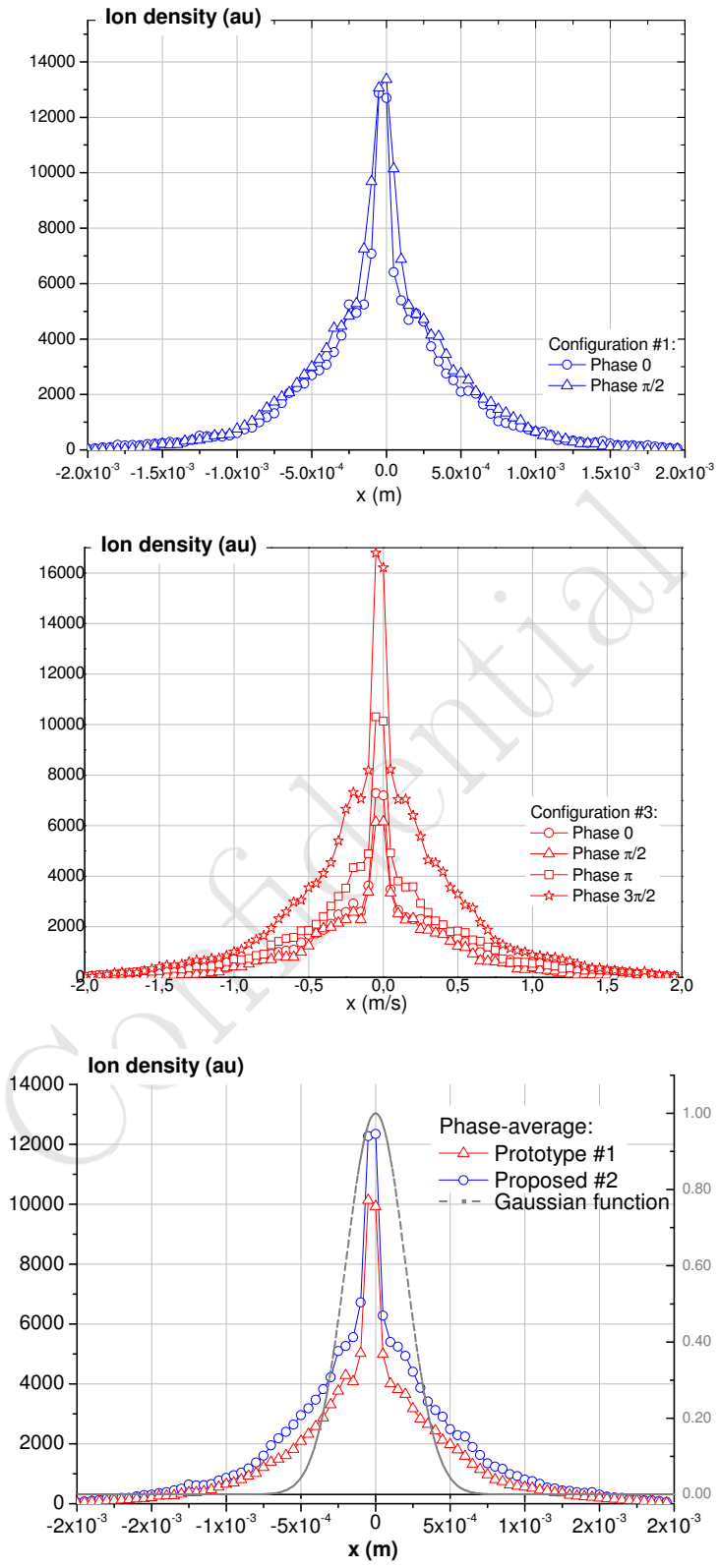

Figure 6.4: Injected ion density *versus* position x for two potential configurations and different initial phases of the RF voltage. (**Top**) configuration #1, (**middle**) configuration #3, and (**bottom**) average value for both configurations.

Confidential

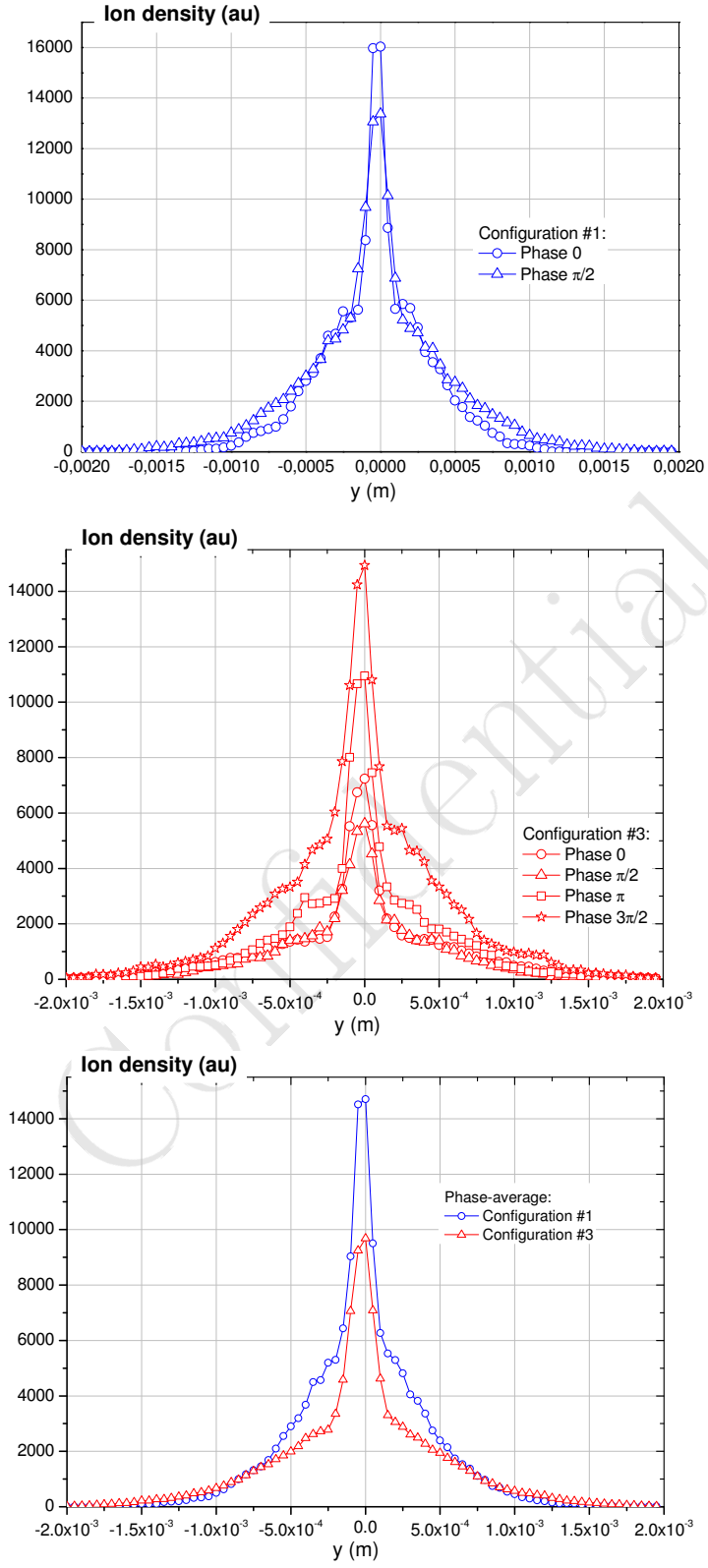

Figure 6.5: Injected ion density *versus* position y for two potential configurations and different initial phases of the RF voltage. (**Top**) configuration #1, (**middle**) configuration #3, and (**bottom**) average value for both configurations.

Confidential

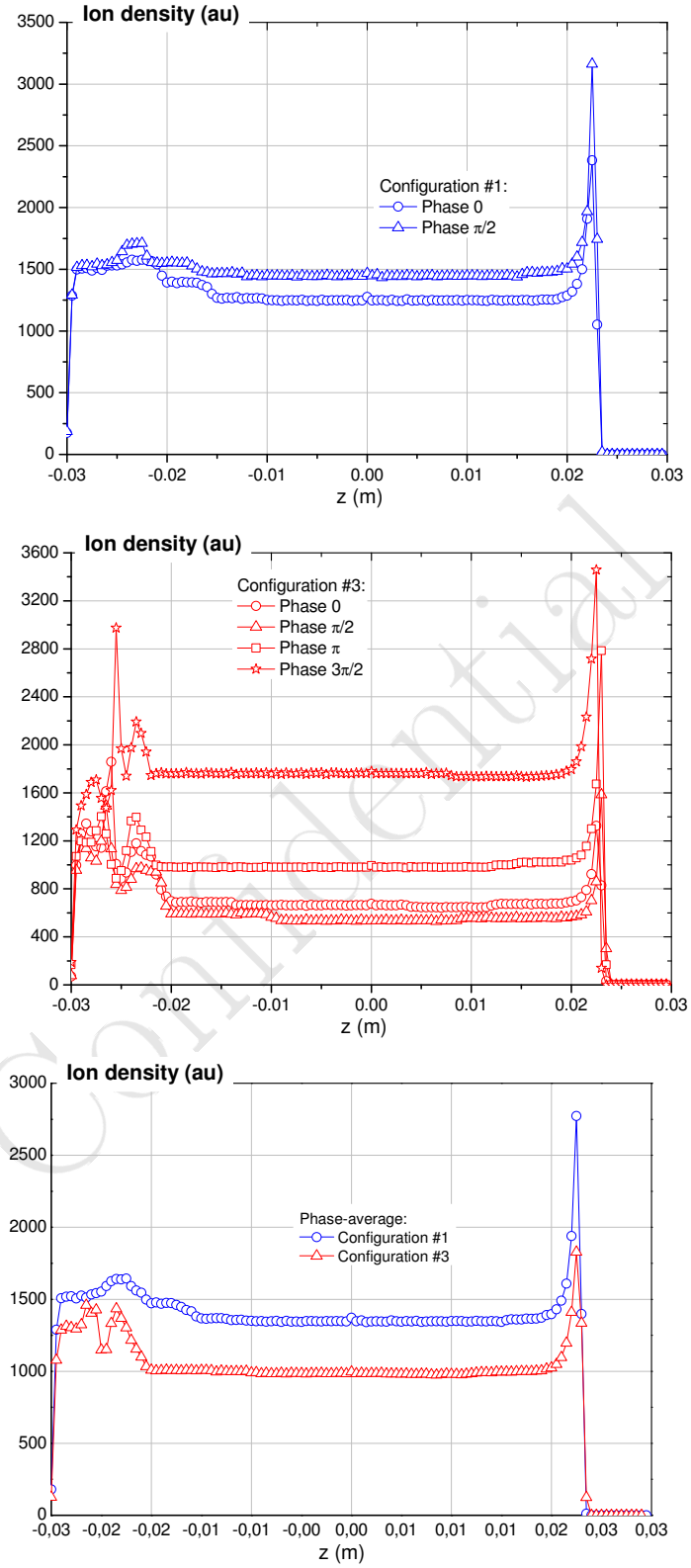

Confidential

Figure 6.6: Injected ion density *versus* position z for two potential configurations and different initial phases of the RF voltage. (**Top**) configuration #1, (**middle**) configuration #3, and (**bottom**) average value for both configurations.

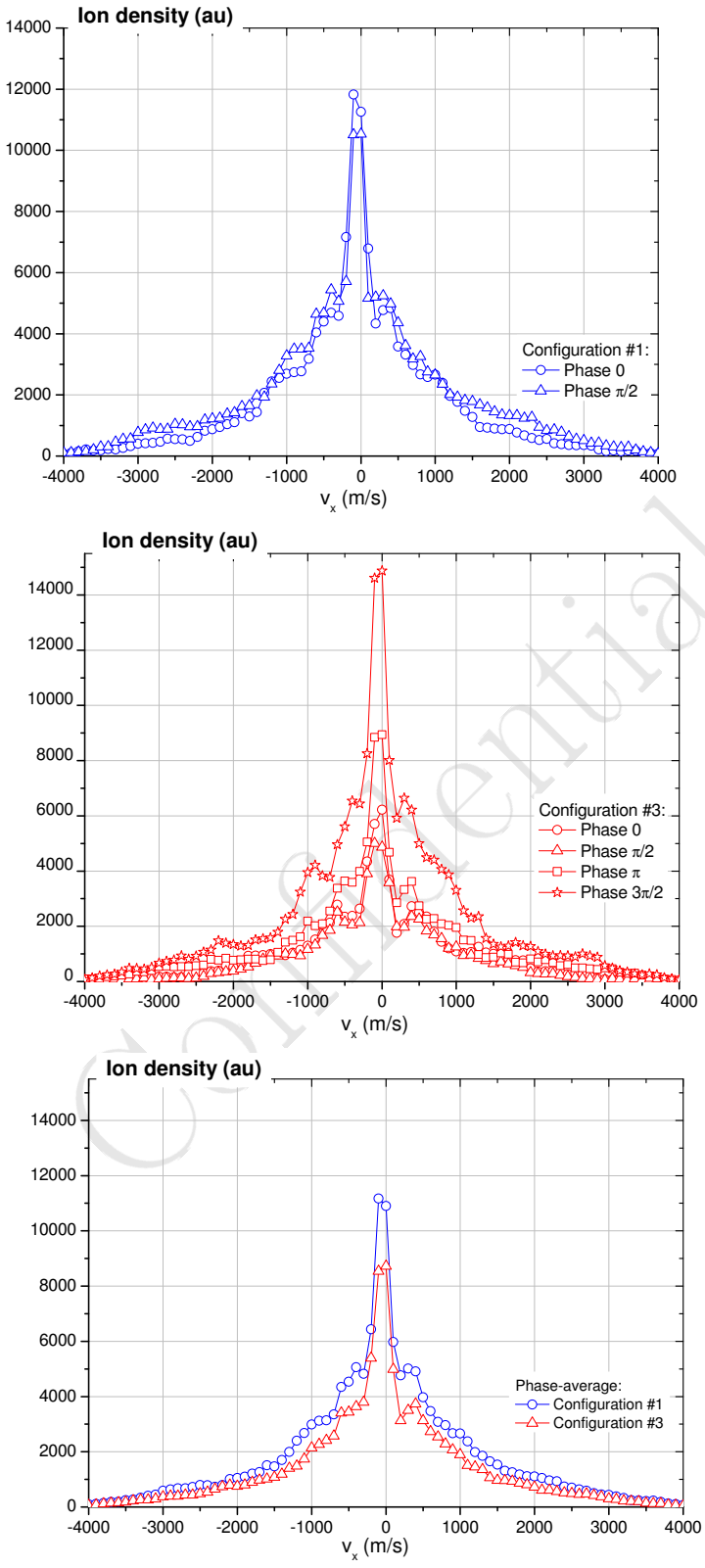

Confidential

Figure 6.7: Injected ion density *versus* velocity v_x for two potential configurations and different initial phases of the RF voltage. (**Top**) configuration #1, (**middle**) configuration #3, and (**bottom**) average value for both configurations.

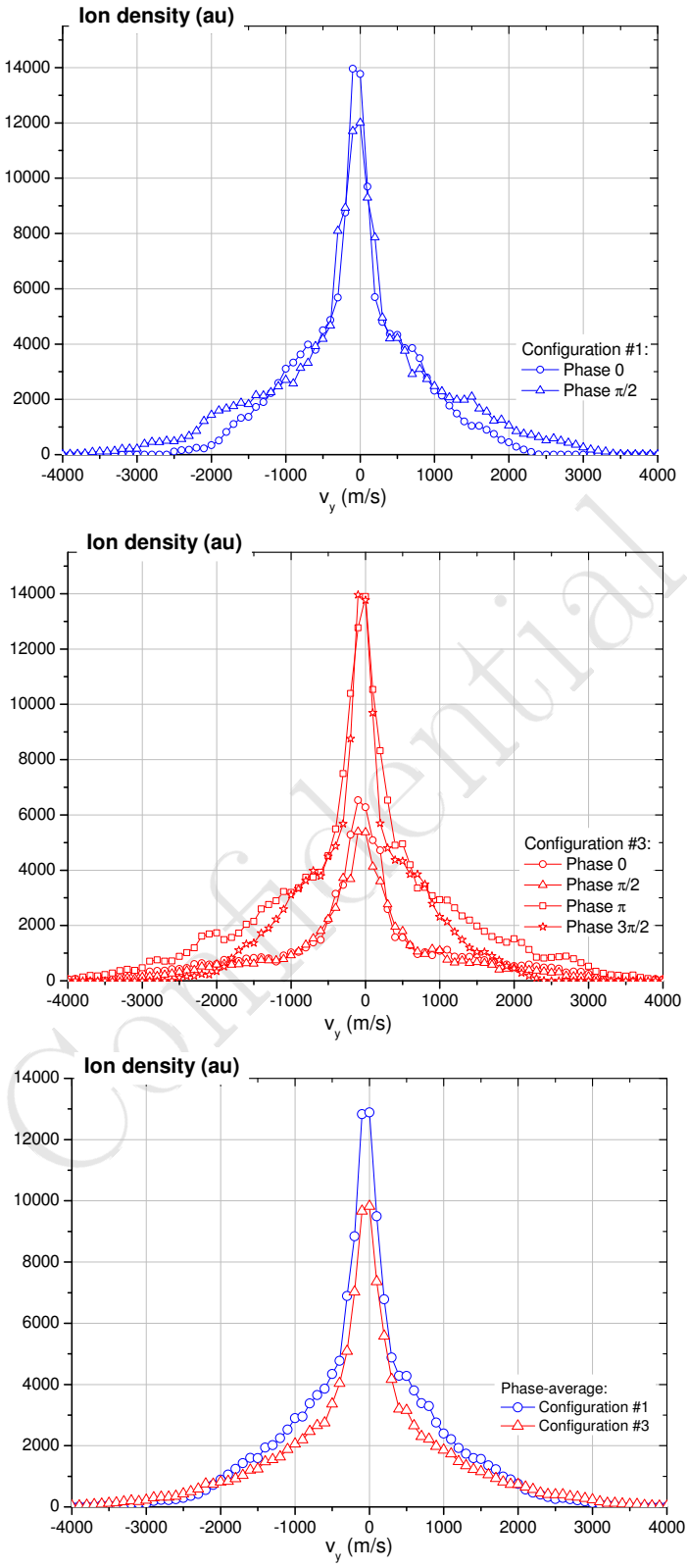

Confidential

Figure 6.8: Injected ion density *versus* velocity v_y for two potential configurations and different initial phases of the RF voltage. (**Top**) configuration #1, (**middle**) configuration #3, and (**bottom**) average value for both configurations.

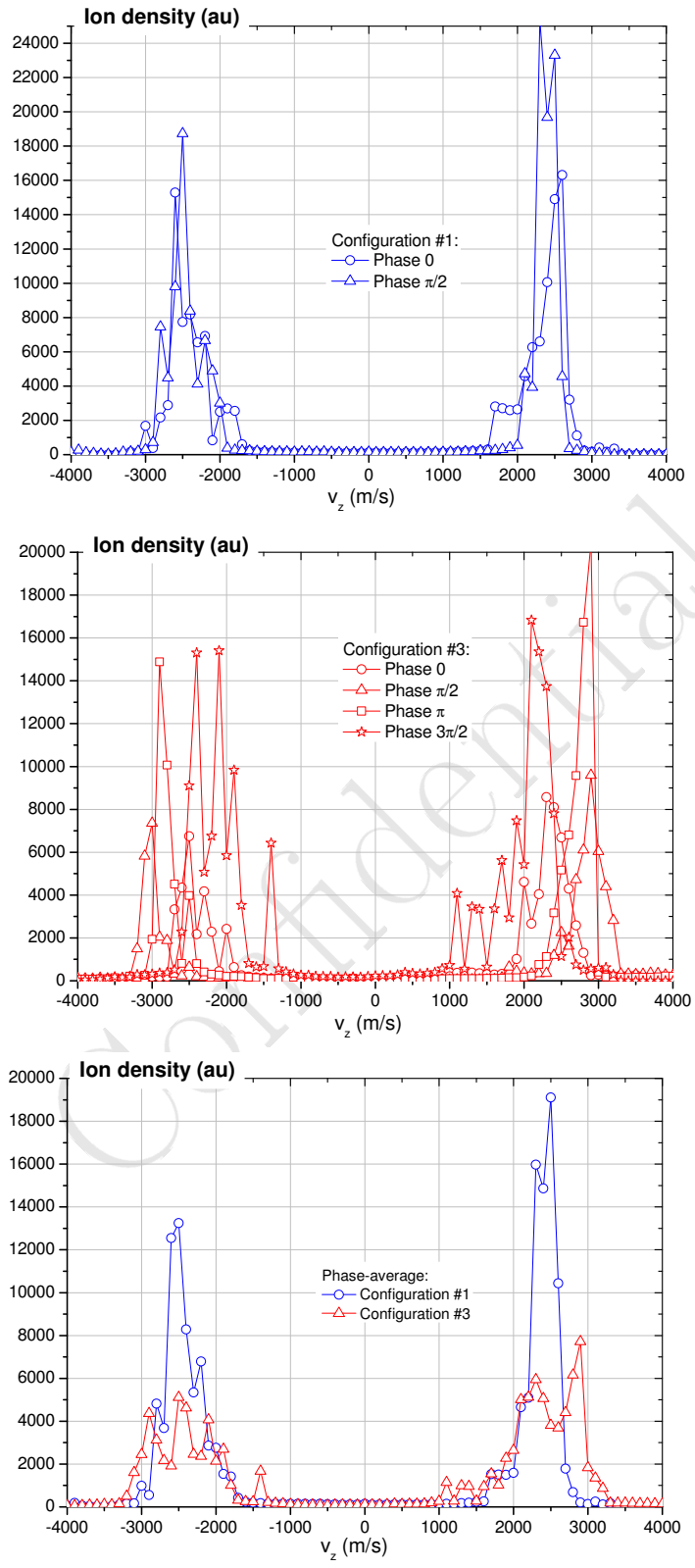

Confidential

Figure 6.9: Injected ion density *versus* velocity v_z for two potential configurations and different initial phases of the RF voltage. (**Top**) configuration #1, (**middle**) configuration #3, and (**bottom**) average value for both configurations.

SIM sequence	Confinement configuration	RF phase	Number of ions (%)
#1	#1	0	44
#1	#1	$\pi/2$	44
#1	#1	average	44
#1	#3	0	16
#1	#3	$\pi/2$	10
#1	#3	π	16
#1	#3	$3\pi/2$	26
#1	#3	average	17
#2	#1	0	56
#2	#1	$\pi/2$	66
#2	#1	average	61
#2	#3	0	26
#2	#3	$\pi/2$	24
#2	#3	π	42
#2	#3	$3\pi/2$	68
#2	#3	average	40

Table 6.1: Number of ions reaching the entrance lens after a round trip in the LIT during injection for two single ion monitoring (SIM) sequences, two confinement potential configurations and different phases of the RF potential.

The initial injection conditions of the ion cloud at decelerating lens have been chosen with a large radial dispersion with initial radial positions and velocities in the trap different from zero as the initial conditions are drawn in the whole of a conic volume defines by the apertures of the decelerating and entrance lenses. A smaller aperture in the entrance length can reduce this radial dispersion. Moreover, the number of injected ions can be increased using a buffer gas, such as He, by reducing the ion kinetic energy, providing that the number of ion/neutral collisions be sufficient during injection. That depends on He pressure in the trap.

Confidential

Chapter 7

Simulation studies of LIT confinement

It is difficult to develop the exact equations of the motion of an ion confined inside a LIT. It can be assumed that the motion equations are uncoupled over a large region around the centre of the LIT and the ion has a constant velocity along the axial direction. However, in the vicinity of the entrance and exit lenses strong non linearities couple the ion motion according to the geometrical dimensions of the lenses and of the LIT, and the potentials applied to the electrodes. The more accurate way to study LIT ion confinement is to design the device and simulate ion trajectories.

Confidential

7.1 Evolution of the number of confined ions

Following the injection studies of the previous chapter, the same operating conditions are kept for a population of 100 ions and the drawing of the initial axial conditions is performed according to the axial distributions obtained for position and velocity. Elsewhere, the initial radial position is chosen off centre at $x(0) = 7\text{x}10^{-4}$ m representing 10 % of the injected ions according to the radial distribution obtained from injection results (figure 6.4).

The evolution of the number of confined ions is tested at operating point $a_x = 0.116 \approx a_{x,apex}/2$ (*i.e.* $U_0 = 2$ V for m/z: 86) and $q_x = q_{x,apex} = 0.706$, for the potential configurations #1 and #3 (figure 7.1). After a fast and large ion loss at the beginning of confinement, the two potential configurations maintain a small amount of injected ions with a same efficiency at about 10 % of injected ions at $5\text{x}10^{-4}$ s, even with an operating point far from the apex.

In order to understand and define the origin of ions lost, the following studies will concern the behaviour of a single confined ion. In addition, some LITs will be compared with different lengths z_0 and an electrode separation $r_0 = 4\text{x}10^{-3}$ m.

7.2 LIT stability diagram in (a_x, q_x) plane

Let us assume that the DC potential induced by the end-cap electrodes is developed at the second order (see the end of the chapter "some elements of theory"). The LIT stability diagram in the

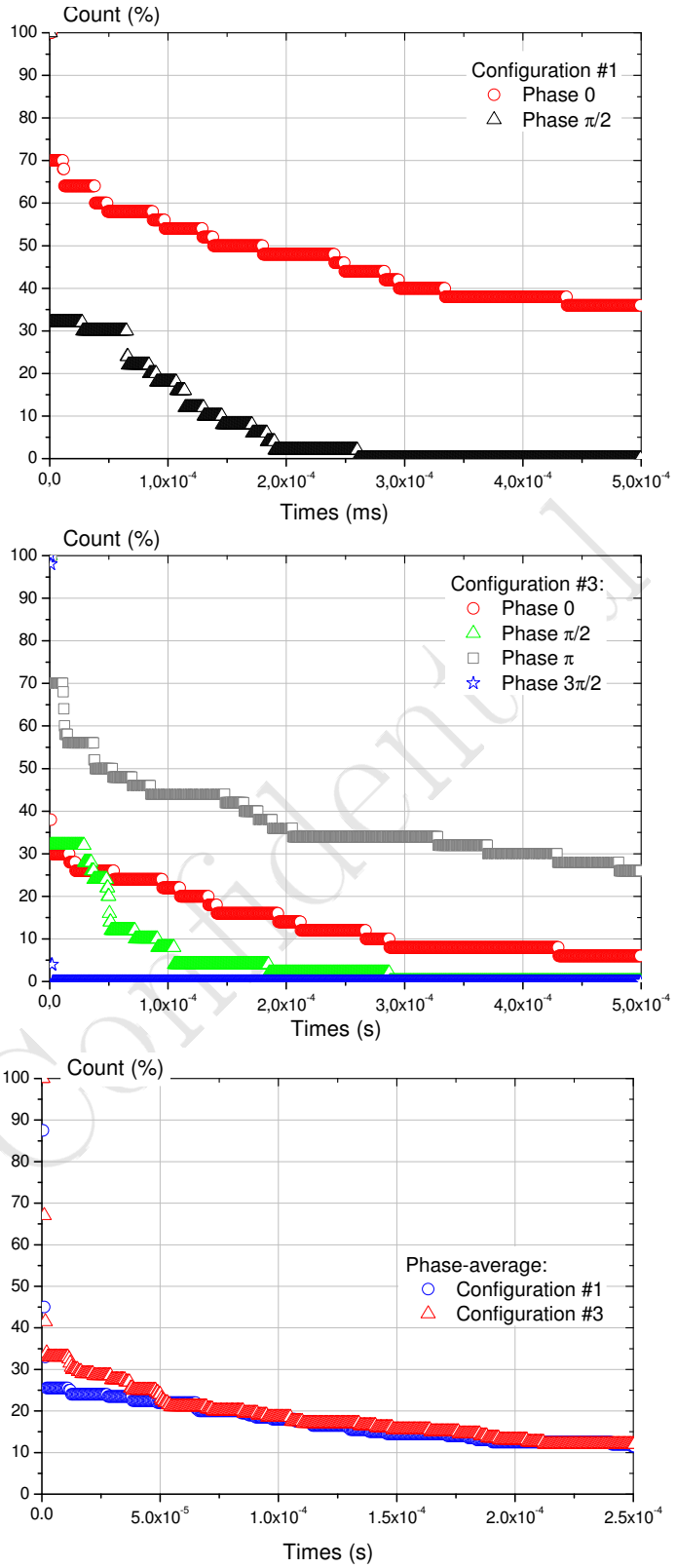

Confidential

Figure 7.1: Number of ions versus confinement time for two potential configurations. (Top) configuration #1, (middle) configuration #3, and (bottom) the average value for both configurations.

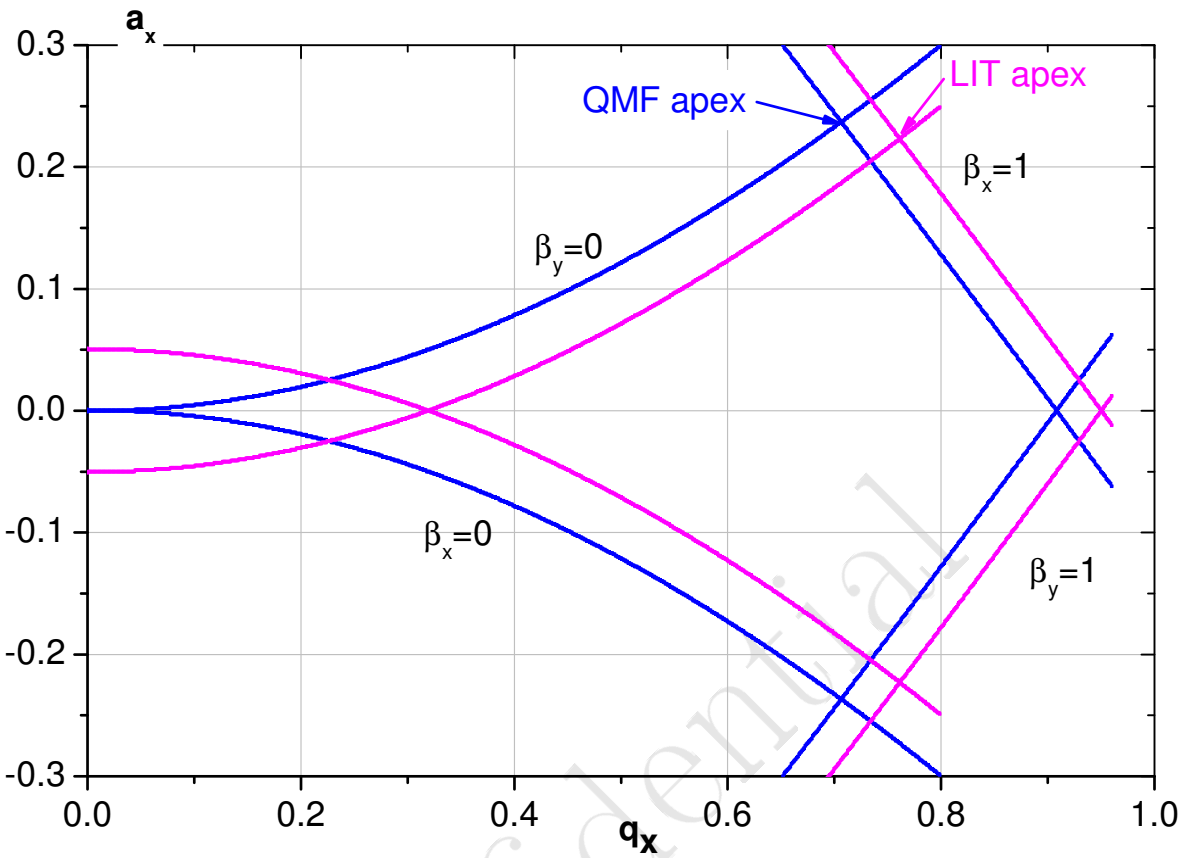

Figure 7.2: QMF and LIT main stability diagram.

Confidential

plane (a_x, q_x) is constructed taking into account: (1) the positive shift $\frac{4ZekU_e}{mz_0^2\Omega^2}$ of the 1D stability zone for both radial directions, and then (2) the symmetry around the q_x axis between the radial directions, as with the mass filter. Figure (7.2) gives the comparison between the QMF and LIT stability diagram in the (a_x, q_x) plane. For the LIT, a same diagram is plotted in the (U_0, V_0) plane for each ion characterized by its m/z ratio. The area of the LIT stability diagram is slightly reduced. The LIT apex location is shifted down and to the right due to the quadrupolar term of the DC potential. The dimensions of the used LIT (z_0>r_0) do not introduce a significant shift of the stability diagram by the quadrupole term.

7.3 Axial DC potential at $r = 0$

The potential induced by the two end-cap electrodes must be developed taking into account higher order terms. For instance, this potential at $r = 0$ m, $\phi_e(0, 0, z) = \phi_e(z)$, can be approximated by the following polynomial development:

$$\phi_{\mathrm{e}}(\mathrm{z}) = \sum_{p=0}^{+\infty} a_{2p} z^{2p} \tag{7.1}$$

As the radial plane is assumed to be a symmetry plane for the device, the polynomial development is limited to the even order terms.

The potential $\phi_e(z)$ can be computed by means of CPO and using a configuration of potentials applied to the mass filter electrodes leading to $\phi_{QMF}(0,0,z) = 0$. The potential $\phi_e(z)$ is plotted for LIT-8, LIT-20, LIT-30, LIT-40, LIT-50 and LIT-60, with z_0 = 4x10^{-3} , 10x10^{-3} , 15x10^{-3} , 20x10^{-3} , 25x10^{-3} and 30x10^{-3} m, respectively, in figure 7.3.

For instance, for LIT-8, using a polynomial mean square interpolation, $\phi_e(z)$ can be approximated by a 6th order polynomial development with $a_0 = 9.997$, $a_2 = 1.215$, $a_4 = 0.00646$ and $a_6 = -0.00028$, the other being neglected (see second curve of figure 7.3). The shortest LIT approaches an harmonic trap, however the potential in the centre of the trap is the highest: a_0 =10.00, 0.444, 0.0382, 0.0217, 0.0058 and 0.0037 V for LIT-8, LIT-20, LIT-30, LIT-40, LIT-50 and LIT-60, respectively.

7.4 Axial and radial motion frequencies

To have a more accurate description of the potential, the expression must be developed taking into account (1) high orders in the axial direction and in the radial plan and (2) coupling terms between the directions. That renders the motion spectra complex.

To plot spectra, the confinement of a single ion has been simulated by CPO for LIT-50 with the following operating conditions: $x(0)$ = 0.1, $y(0)$ = 0.1 and $z(0)$ = 2x10^{-2} m; $v_x(0) = v_y(0) = v_z(0) = 0$ m/s; m/z: 300; $\Omega/2\pi$ = 1 MHz; and r_0 = 4x10^{-3} m. The confinement duration has been chosen in order to have a suitable peak width. The ion trajectory is multiplied by an apodisation function to reduce the frequency peak "wiggles" induced by finite-time observation of the temporal signal. Zero-filling are added to the ion trajectory prior to Fourier transformation to reduce the computed frequency steps.

The axial- and radial-motion spectra are plotted in figure 7.4 and the peaks are identified in table 7.1.

In the axial direction, only the odd order frequencies of the axial motion are observed coming from the even order terms of the potential (equation 7.1). The coupling between the radial and the axial direction, for instance at $\omega_x - \omega_z$ have not a significant magnitude due to the low value of ratio between the maximal radial and axial motion extension used.

In the radial direction, the peaks ω_x, $\Omega - \omega_x$, $\Omega + \omega_x$, ... are identified and also the coupling peaks between the radial and axial directions $\omega_x \pm 2n\omega_z$. Only the frequency $2n\omega_z$ is observed as the axial period corresponds to a round trip in the trap.

With non-linearities, the frequencies depend on a_{2p} factor of the potential development and on

Confidential

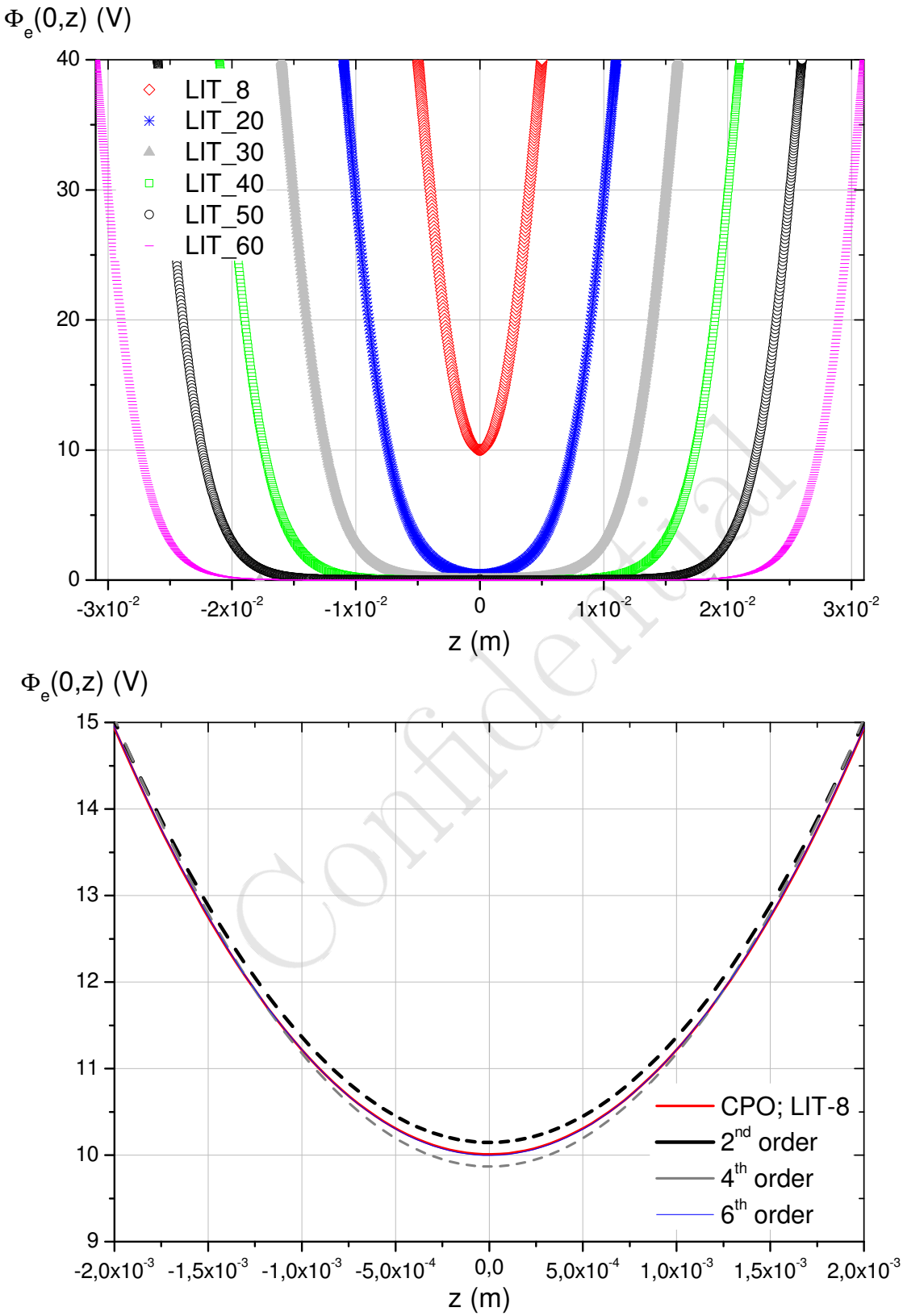

Confidential

Figure 7.3: Top: $\phi_e(z)$ computed by CPO for LIT-8, LIT-20, LIT-30, LIT-40 and LIT-50 and $r_0 = 4\text{x}10^{-3}$ m. Bottom: $\phi_e(z)$ for LIT-8 for 2^{rd}, 4^{th} and 6^{th} orders of the polynomial approximation.

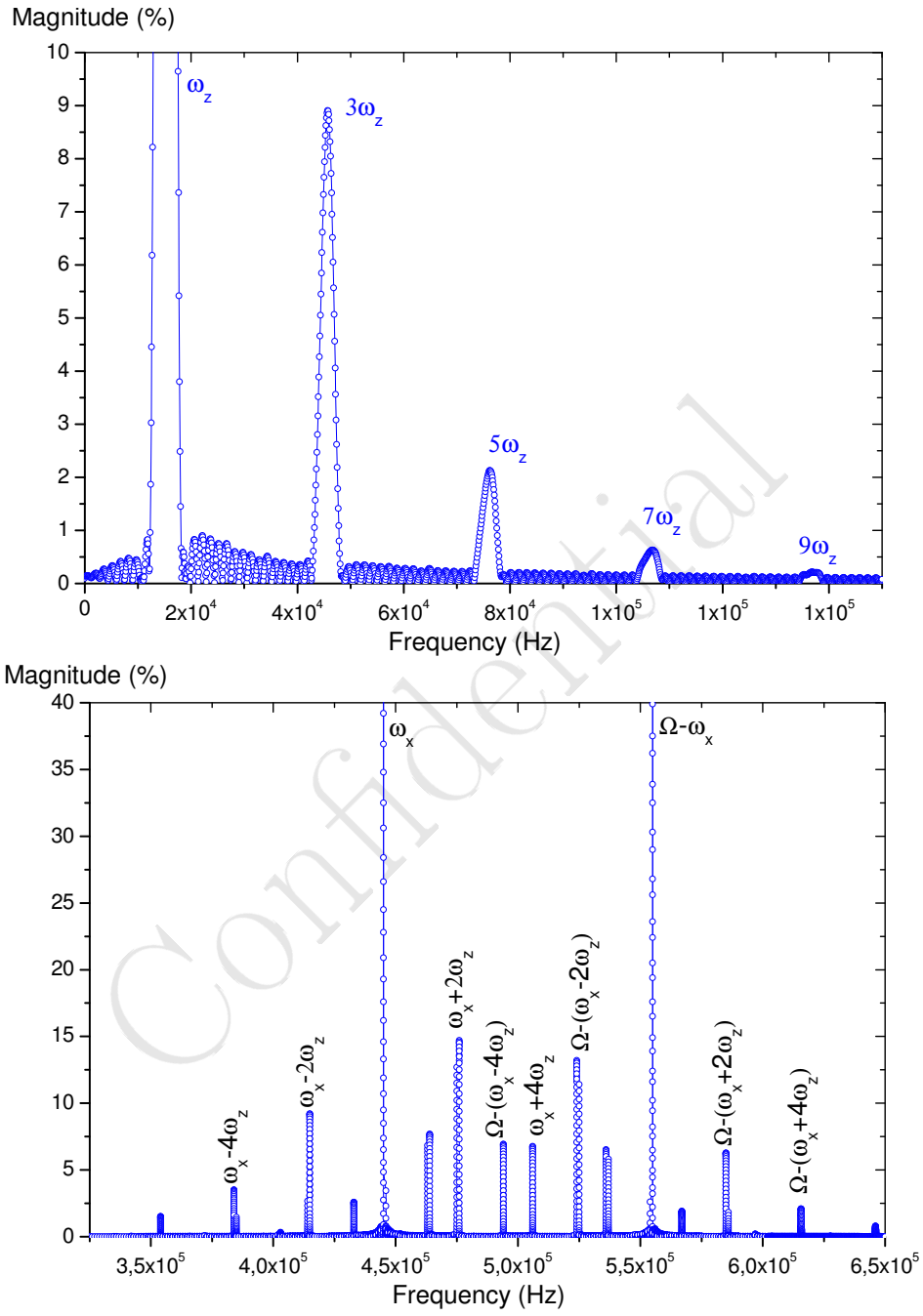

Confidential

Figure 7.4: Axial (top) and radial (bottom) trajectory spectra of LIT-50. The operating conditions are: $x(0) = 0.1$, $y(0) = 0.1$ and $z(0) = 2\text{x}10^{-2}$ m; $v_x(0) = v_y(0) = v_z(0) = 0$ m/s; m/z: 300; $\Omega/2\pi =$ 1 MHz and $r_0 = 4\text{x}10^{-3}$ m.

Peak	Frequency (Hz)	Magnitude (%)
ω_z	$15.3\text{x}10^{-3}$	100
$3\omega_z$	$45.9\text{x}10^{-3}$	9
$5\omega_z$	$76.5\text{x}10^{-3}$	2.2
$7\omega_z$	$107.1\text{x}10^{-3}$	0.7
$9\omega_z$	$137.7\text{x}10^{-3}$	0.2
$\omega_x - 4\omega_z$	$383.8\text{x}10^{-3}$	3.06
$\omega_x - 2\omega_z$	$414.4\text{x}10^{-3}$	8.79
ω_x	$445\text{x}10^{-3}$	100
$\omega_x + 2\omega_z$	$475.6\text{x}10^{-3}$	14.3
$\omega_x + 4\omega_z$	$506.2\text{x}10^{-3}$	6.69
$\Omega - (\omega_x - 4\omega_z)$	$493.8\text{x}10^{-3}$	6.9
$\Omega - (\omega_x - 2\omega_z)$	$524.4\text{x}10^{-3}$	6.25
$\Omega - \omega_x$	$555\text{x}10^{-3}$	76.3
$\Omega - (\omega_x + 2\omega_z)$	$585.6\text{x}10^{-3}$	13.1
$\Omega - (\omega_x + 4\omega_z)$	$616.2\text{x}10^{-3}$	7.25

Table 7.1: Identification of some measured peaks in figure 7.4 according to their magnitude and frequency.

the maximal extension of the confined ion. The axial period of LIT-50 is computed for different values of $z(0)$, corresponding to the maximal axial extension of the ion as $v_z(0) = 0$ (see figure 7.5). The value of the period depends strongly on $z(0)$, in contrast to the case for a quadrupole mass filter. In addition the initial phase of the RF confinement potential slightly modifies the value of the period, as well as the radial extension.

7.5 Non-linearity influence on LIT stability diagram in (U_0, V_0) plane

In a pure quadrupole device, the stability diagram comes from the stable solutions of Mathieu equations in each direction. For a given LIT (depending on its geometric aspect and applied potentials) with strong non-linearities, the term "stability diagram" must address the confinement of a single ion (that means that the ion remains inside the LIT) for given values of initial positions and velocities and a given confinement time t_{conf}. As a consequence many stability diagrams can be defined.

In this section, the operating conditions are:

- the confinement time, $t_{conf} = 10^{-3}$ s.
- the initial radial positions $x(0) = y(0) = 10^{-4}$ m for $r_0 = 4\text{x}10^{-3}$ m.
- the initial velocities $v_x(0) = v_y(0) = v_z(0) = 0$.
- the initial axial positions $z(0)$ is varied. The initial position $z(0)$ can also be considered as the maximal extension z_{max}, as $v_x(0) = 0$ and if it is assumed that there are no couplings between the axial and radial directions.

Confidential

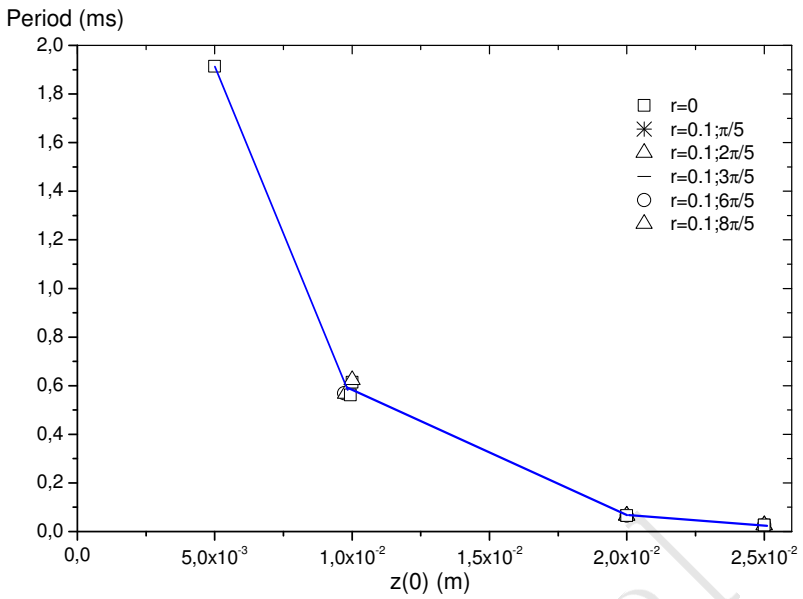

Figure 7.5: Axial period of LIT-50 *versus* $z(0)$ position: in axial direction with $x(0) = y(0) = 0$ m, and in radial and axial direction with $x(0) = y(0) = 10^{-4}$ m, at different phases.

7.5.1 Maximal value

First, the maximal value $V_{0,max}^{LIT}$ at $U_0 = 0$ of LIT stability diagram is calculated by means of CPO trajectory computation by varying V_0 with steps of 0.1 V around $V_{0,max}^{QMF}$ the theoretical maximal value for the quadrupole mass filter. The highest value of V_0 at which the ion is confined during at least 1 ms is $V_{0,max}^{LIT}$. This value is plotted versus $z(0)$ in figure 7.6 for m/z: 50, 100 and 300 and LIT-50.

$V_{0,max}^{LIT}$ is lower than $V_{0,max}^{QMF}$ and it diminishes with the increasing of $z(0)$ for the three mass-to-charge ratios. The location of the maximal value of the stability diagram is shifted to the left towards lower values leading to an area reduction of the stability diagram.

7.5.2 Apex value

The SIM operating mode requires to know accurately the value of potentials $U_{0,apex}^{LIT}$ and $V_{0,apex}^{LIT}$ to be applied to the electrodes to operate the LIT at the apex of the stability diagram.V_0 is chosen equal to $V_{0,apex}^{QMF}$ and U_0 is varied with steps of 0.1 V around $U_{0,apex}^{QMF}$, the theoretical apex value for the quadrupole mass filter. The highest value of U_0 at which the ion is confined during at least 1 ms is $U_{0,apex}^{LIT}$. This value is plotted versus $z(0)$ in figure 7.7 for m/z: 50, 100, 200 and 300 and LIT-50.

$U_{0,apex}^{LIT}$ is measured lower than $U_{0,apex}^{QMF}$ and depends on $z(0)$. $U_{0,apex}^{LIT}$ remains constant at U_0' within 0.3 V from $z(0) = 0$ until $15\text{x}10^{-3}$ m, then a significant decrease is observed with the increasing of $z(0)$ for the four mass-over-charge ratios, about 10 V at $z(0) = 23\text{x}10^{-3}$ m. From $z(0) = 0$ to $15\text{x}10^{-3}$ m, only the quadrupolar term a_2 is significant as there is no dependency with $z(0)$. Non-linearity higher orders become not neglectable with the increase of $z(0)$ as their influence

Confidential

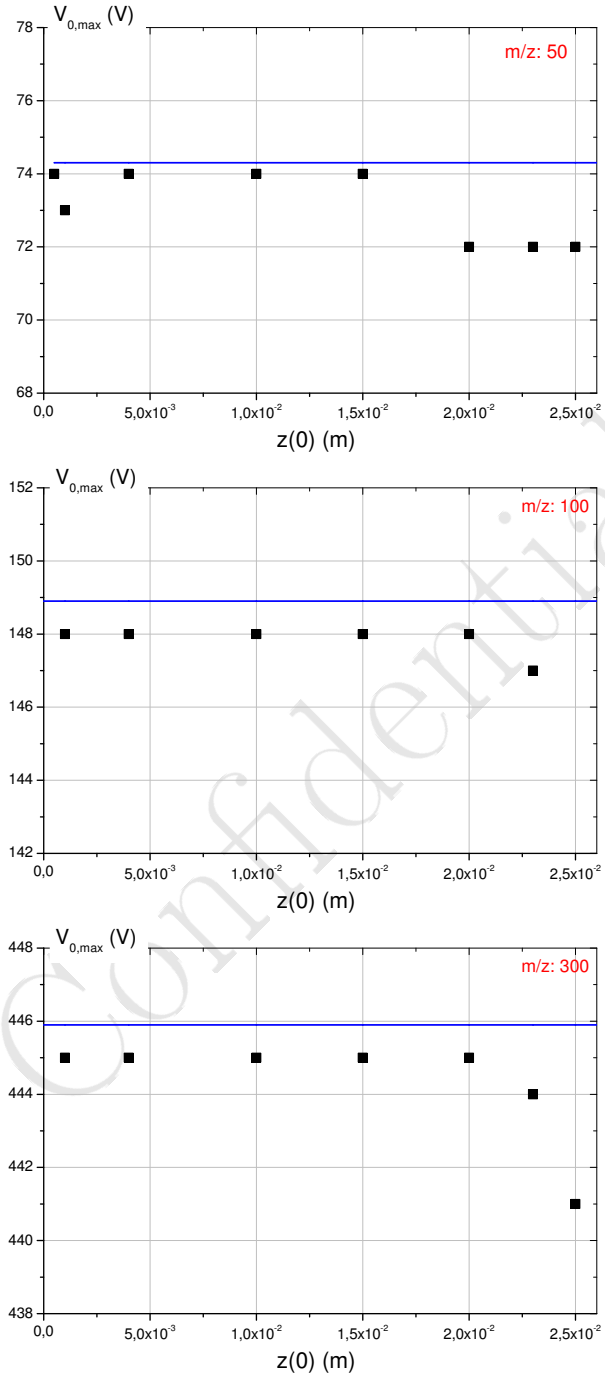

Figure 7.6: (Square): $V_{0,max}^{LIT}$ versus $z(0)$ for the LIT-50 at different m/z: 50, 100 and 300. (Line): $V_{0,max}^{QMF}$, the theoretical maximal value for the quadrupole mass filter.

Confidential

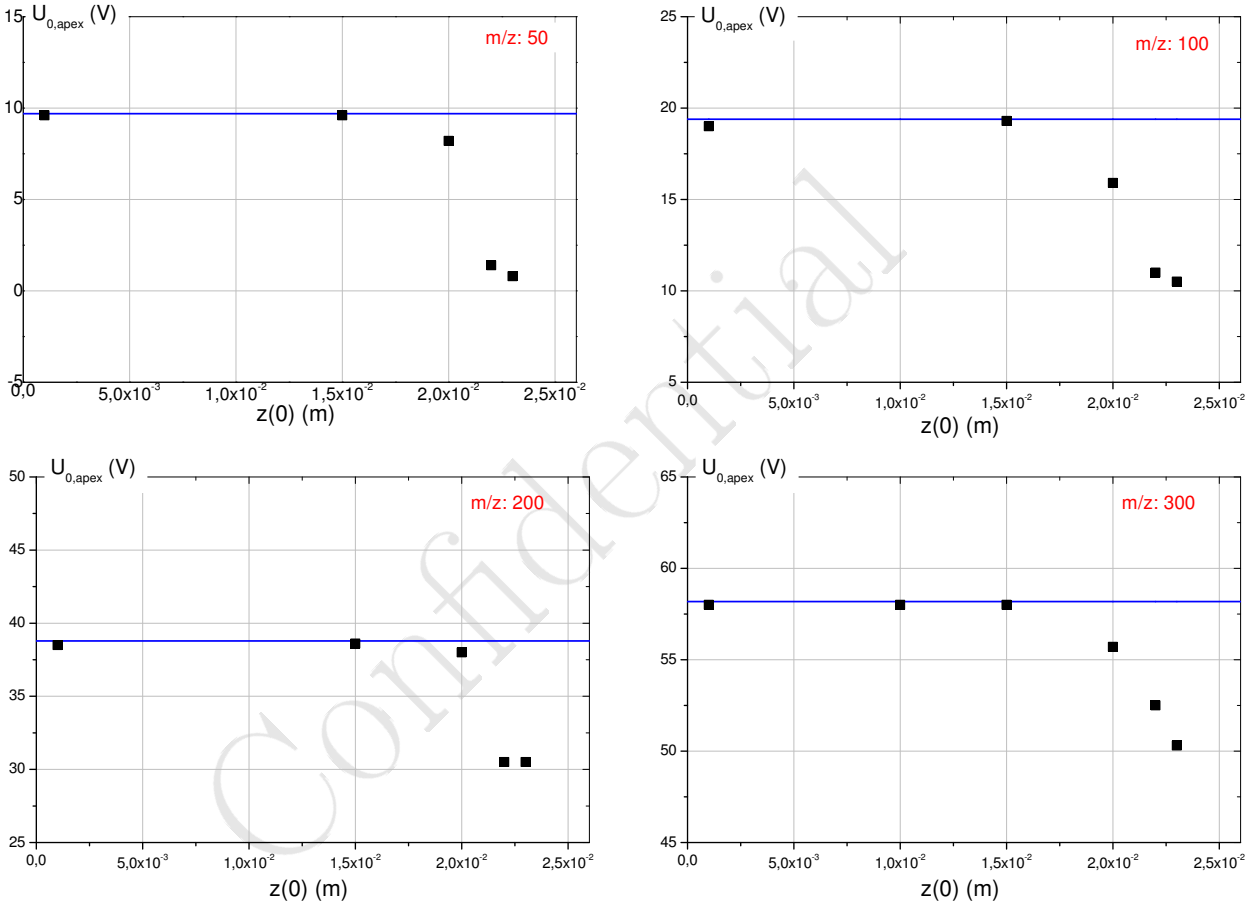

Confidential

Figure 7.7: (Square): $U_{0,apex}^{LIT}$ versus $z(0)$ for the LIT-50 at different m/z: 50, 100, 200 and 300. (Line): $U_{0,apex}^{QMF}$, the theoretical maximal value for the quadrupole mass filter.

depends on it.

The location of the apex value of the stability diagram is shifted down towards lower values with the increase of $z(0)$ leading to an area reduction of the stability diagram. If it is chosen $U_{0,apex}^{LIT} = U_0^{'}$, it can be considered that only the ions having a maximal extension lower than $z_{max,conf} = 15\text{x}10^{-3}$ m are confined, the others are lost. In order to increase the number of confined ions, it is necessary to reduce ion trajectory extension to use $U_{0,apex}^{QMF}$ or $U_{0,apex}^{LIT}$ could be chosen lower than $U_0^{'}$, however the selectivity (or resolution) will be reduced.

In addition, according to results not shown in a figure, the shorter the length of the LIT z_0, the larger the shift down , the larger $z_{max,conf}$.

7.6 Collisional cooling

The value $U_0^{'}$ is computed and the corresponding average maximal extension $z_{max,conf}$ (to have the ion confined) is determined for other LIT lengths LIT-40, LIT-50 and LIT-60. The normalised value $z_{max,conf}/z_0$ (in %) *versus* z_0 is plotted in figure 7.8. For instance, with LIT-50, if it is chosen $U_{0,apex}^{LIT} = U_0^{'}$, the confined ion cloud is limited at about 60 % of the trap. The more the length of LIT, the more the relative size of the confined ion cloud.

Furthermore, let us calculate the maximal extension of the ion cloud at injection $z_{max,inj}$. Its value can be approximated from the potential $\phi_e(z)$ given by CPO simulations (see figure 7.3) . If we only take into account the potential in the centre of the trap, and consider a symmetric configuration of RF potentials applied to the rods leading to zero at the centre of the trap, the extension of the injected ions will not exceed $z_{max,inj}$ such as: $\phi_e(z_{max,inj}) = V_s$, where V_s (in eV) is the initial kinetic energy of mono-charged ions in the source. In figure 7.8 (top) the potential $\phi_e(0,z)$ is plotted *versus* the axial position of LIT-50. The maximal axial extension at injection for an ion source at 3 eV is $z_{max,inj} = 20\text{x}10^{-3}$m. If the ion is located at QMF,apex, the maximal axial extension of the confined ions is $z_{max,inj} = 15\text{x}10^{-3}$m. It is necessary to cool the ion to reduce trajectory extension under $15\text{x}10^{-3}$m. At 3 eV, the cooling time is estimated at 0.5 ms.

In figure 7.8 (bottom), $z_{max,inj}/z_0$ is plotted *versus* the five trap lengths for two ion source energies 3 and 5 eV (typical values).

For instance with LIT-50, the injected ion cloud occupies about 80 % of the trap. If the operating values are such as $U_{0,apex}^{LIT} = U_0^{'}$ and $V_0 = V_{0,apex}^{QMF}$, ions will be lost as $z_{max,inj} > z_{max,conf}$.

In order to increase the number of confined ions, the initial axial extension should be reduced. For instance, in 3D ion trap, an helium buffer gas is used to cool the ions to the centre of the trap in order to greatly increase mass resolution and sensitivity in scanning operating mode. This cooling process can reduce the kinetic energy of confined ions to the minimal value of $1/2kT$ (equal to about

Confidential

0.013 eV at room temperature) [109, 110, 111, 112].

Assuming a cooling buffer gas in the LIT that reduces ion kinetic energy to kT, $3kT$ and $10kT$, and let us consider only the axial direction. Figure 7.8 gives the localisation around the trap centre for five trap lengths (LIT-8, LIT-20, LIT-30, LIT-40, LIT-50 and LIT-60) of a cloud of confined ion subjected to cooling collisions. The corresponding maximal axial extension $z_{max,nkT}$ is calculated from the potential previously computed and given in figure7.3, such as: $\phi_e(z_{max,nkT}) = \phi_e(0)+nkT$. To have a normalised value, $z_{max,nkT}/z_0$ is plotted *versus* z_0.

The more the LIT length, the more the relative size of the ion cloud. The cooling efficiency is then higher in short LITs. As a consequence, due to the relative spatial extension of the cooled-ion cloud, space charge effect is lower in large LITs. However, due to larger extensions in long LITs, the ion cloud is more subject to non-linearities at both LIT ends. For instance with LIT-50, the cooling effect will reduce at about 50 % the confined ion cloud, while at injection the ion cloud occupies about 80 % of the LIT.

If the LIT is operated at apex, such as $U^{LIT}_{0,apex} = U'_0$ and $V_0 = V^{QMF}_{0,apex}$, the maximal extension for the ion to be confined is given by $z_{max,conf}$. The determination of this value has been described in the previous section; it has been found $z_{max,conf} = 15\text{x}10^{-3}$ m for LIT-50. Many other simulations have been performed to compute this value for LIT-40 and LIT-60 (Figure 7.8). Without buffer gas cooling, an ion loss accurs as $z_{max,inj} > z_{max,conf}$. With cooling, a maximal number of ions can be confined.

This approach concerns only the axial direction. Non linearity effects due to couplings between axial and radial directions can induce an axial motion heating. However using a cooling gas, the radial trajectory extensions will also be diminished leading to more reduced energy exchange between the directions as it depends on maximal trajectory extension.

Confidential

7.7 Further studies and proposals

It is evident that the ion cloud must be thermalised toward the centre of the trap by helium buffer gas cooling. If the entrance air flow is pulsed, the cooling gas should be pulsed too.

Further studies have been performed by University of Liverpool using a pre-prototype mass spectrometer including an EI open source and a LIT. The efficiency of helium has been proved in experiment with confined xenon ions.

Figure 7.9 shows variation of relative intensity of trapped Xe ions within LIT without buffer gas (top) and with increase of He buffer gas pressure (bottom). In buffer gas tests, partial pressure for Xe is set to previously found optimal value (*i.e.* $4\text{x}10^{-3}$ Pa) and helium buffer gas was further loaded in pressure steps up to $6.67\text{x}10^{-2}$ Pa. As an increase of the signal intensity is observed until $9.33\text{x}10^{-3}$ Pa, 80% improvement in sensitivity is obtained with a pressure of $8\text{x}10^{-3}$ of additional buffer gas.

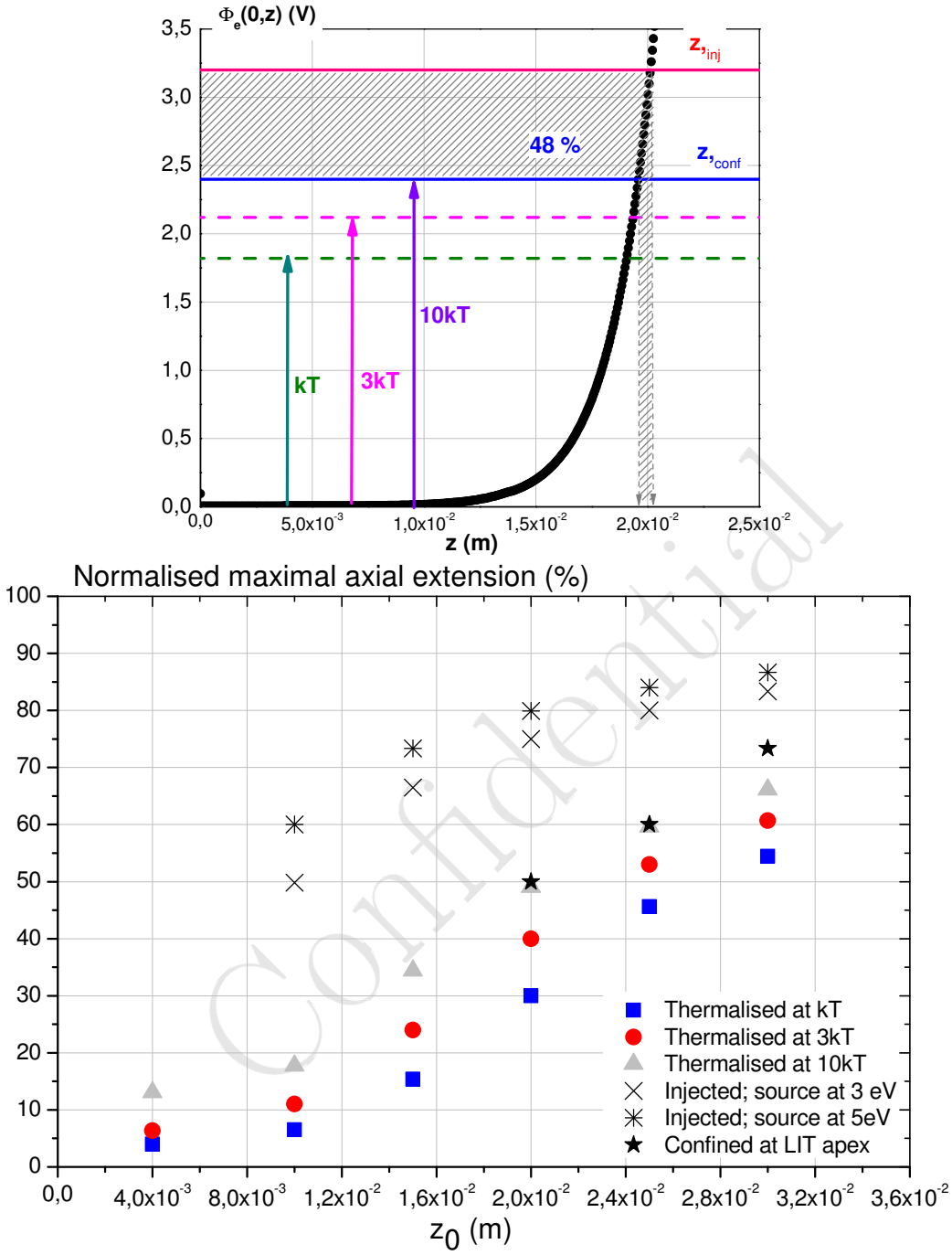

Confidential

Figure 7.8: (Top) Potential curve $\phi_e(0,z)$ (●) to axial position z_0 of LIT-50, with according $z_0 = 25\text{x}10^{-3}$m and $r_0 = 4\text{x}10^{-3}$m, $z_{max,inj}$ is the maximal axial extension at injection for an ion source at 3 (×). $z_{max,nkT}$ is the maximal axial extension for an ion thermalised at nkT with $n = 1$, 3 and 10. $z_{max,conf}$ maximal axial extension of the confined ions when $U^{LIT}_{0,apex} = U'_0$ (LIT operated at apex). (Bottom) Expected maximal axial extensions of the ion cloud versus LIT lengths (LIT-8, LIT-20, LIT-30, LIT-40, LIT-50 and LIT-60) with $r_0 = 4\text{x}10^{-3}$m. $z_{max,inj}$ at 3 (×) and 5 (+) eV. $z_{max,nkT}$ at nkT with $n = 1$ (□) , 3 (○) and 10 (△) . (★) $z_{max,conf}$.

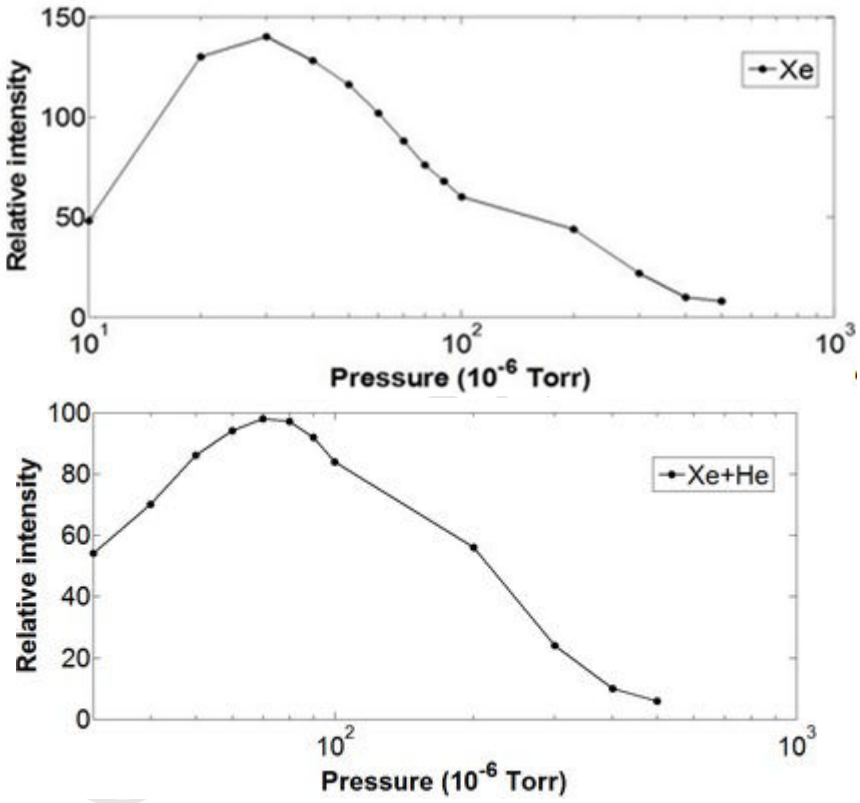

Figure 7.9: Signal intensity variation for Xe ions trapped within Liverpool's LIT without buffer gas (top) and with increase of He buffer gas pressure (bottom). (From unpublished works with courtesy of University of Liverpool).

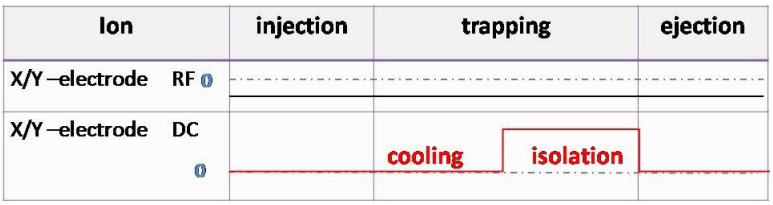

Figure 7.10: Adaptation of the Single Ion Monitoring sequence to increase sensitivity and resolution with DC confinement potential switched to zero during injection and ion cooling.

Beyond that, sensitivity will be also increased, and resolution too, using a new SIM sequence with LIT operated in RF only mode during injection. It requires to set to zero the DC confinement potential during injection. This new SIM sequence including the ion cooling stage during trapping is described in figure 7.10. The DC confinement potential must also be turned to zero during ion cooling stage. However, the ions having the largest trajectory extensions can be lost at 0 V for masses lower than m/z: 50 (see figure 7.7). A DC negative value should be applied for lower masses.

Confidential

Confidential

Conclusion

The work described in this dissertation address a mass spectrometer pre-prototype that is at University of Liverpool. An electron source has been proposed as well as improvements to LIT operating mode for mass analysis, taking into account the portability of the device.

The Glow Discharge Electron Source (or GDES) cell is an interesting source of electrons for handled mass spectrometry as it can operate at low vacuum values ($1.333.10^{-1}$ Pa, typ.) and low power consumption (0.3 W at 420 V, typ.) with stability, reproducibility and long lifetime. The kinetic energy of the electron beam at the anode aperture of the GDES cell has been experimentally measured: it ranges over a narrow range 0-20 eV. These works has been published in "Plasma Sources Science and Technology" [113].

The coupling of that source of electrons with an open EI source is easy to implement: only the filament support has to be removed. The electrons of the beam are focussed toward the ion cage by means of an appropriate potential value applied to the repeller. The anode has to be polarised according to the potential value applied to the ion cage in order to define the mean kinetic energy of electrons for ionisation in the ion cage. The other supplies and applied potential values are the same than those used with an EI source with filament.

The electron beam intensity of GDES is low: it has been measured less than 10^{-6} A. However, according to the shape of the electron-impact ionisation cross-section curve of the targeted compounds, with such a narrow kinetic energy range and the possibility to set the mean value of electron kinetic energy at the maximum of the cross-section curve, the cloud of electrons has optimal ionisation efficiency. Experimental results given by the coupling have confirmed that. Furthermore, the fragmentation pattern of the molecules depends on the electron kinetic energy at impact. The fragmentation paths of the molecule are then well controlled and reproducible with such a narrow energy range.

The spectra obtained with GDES/EI coupling will be of a great concern as they allow us to identify the created ions and provide the EI fragmentation pattern information, which depends on the initial electron kinetic energy. That will be done with the delivery of a flange-mounted prototype including an open ions source, a LIT and an electron multiplier. An invention disclosure report is being written on GDES/EI coupling.

Confidential

The improvement of LIT operating mode aims the sensitivity and resolution. Ion injection and confinement simulation studies led us to propose an adaptation of the operating mode of the LIT.

The LIT must be operated in an RF only mode during the injection and cooling stages. That involves an additional functionality to ECU: the switching of the DC confinement potential applied to the rods. A helium buffer gas cooling is necessary to reduce ion motion in both radial and axial directions. As a consequence, the effects of the direction couplings due to non-linearities are diminished. And the lowering of the axial trajectory extension allows us to gain an increase of both sensitivity and resolution with LIT operated in Selective Ion Monitoring mode. However, the use of the helium can be an issue for the chosen pumping system. The benefit of helium buffer gas has been confirmed with experimental results obtained at University of Liverpool.

Other parameters must be tested in simulation, such as the DC confinement potential applied to the end-cap electrodes and other dimension ratios of the LIT to reduce the non-linearity effects. And comparative (experimental/simulation) studies can be performed with delivery of the mass spectrometer prototype.

Furthermore, the effects of collisions with the residual gas (mainly N_2 in portable device at low vacuum) and a buffer gas are studied by the laboratory. A numerical tool based on the temporal invariance method is being developed to study the statistical ion states (distribution functions of positions and velocities) at equilibrium state[112]. It has been tested for 3D quadrupole ion traps. It is now being extended to be employed for collision studies in 2D linear ion traps.

Modifications have been taken into account in the first mass spectrometer prototype with a demonstration in May 2015. Others will be integrated in forthcoming releases of the device.

Confidential

Publication

Confidential

Confidential

IOP Publishing Plasma Sources Science and Technology
Plasma Sources Sci. Technol. **24** (2015) 015001 (8pp) doi:10.1088/0963-0252/24/1/015001

A dc glow discharge as a source of electrons for a portable mass spectrometer: characterization of the electron current intensity and electron kinetic energy distribution

A Chalkha[1], C Despenes[1,2], A Janulyte[1], Y Zerega[1], J Andre[1], B Brkic[3] and S Taylor[3]

[1] Aix-Marseille Université, LISA EA 4672, Centre de Saint Jérôme, Avenue Escadrille-Normandie-Niemen, 13397 Marseille Cedex 20, France
[2] Protisvalor Méditerranée, 8, rue Sainte Barbe, 13001 Marseille, France
[3] Department of Electrical Engineering and Electronics, University of Liverpool, Brownlow Hill, Liverpool L69 3GJ, UK

E-mail: aurika.janulyte@univ-amu.fr (A Janulyte)

Received 10 April 2014, revised 3 September 2014
Accepted for publication 17 October 2014
Published 17 November 2014

Abstract

A dc glow discharge cell with planar electrodes operating at about 1 Torr has been characterized with an inlet flow from ambient air. It will be used as a source of electrons to further ionize molecules by electron impact in a portable mass spectrometer.

The Paschen curve has been measured for six values of the pressure around the minimum of the curve. The voltage-current characteristic, observed until 7 mA for different values of the pressure, increases with current in the normal glow regime. The temporal evolution of the discharge current has been recorded over long periods greater than one day for different insulator materials. The best stability has been obtained with Macor and Nylon. The available electron current for ionization has been measured at about 0.6 μA and the electron kinetic energy distribution has been found to be between 0 and a few tens of eV.

Keywords: dc glow discharge; electron source; atmospheric air characteristic; portable mass-spectrometry

1. Introduction

Low power and reduced gas load, small size, lightness, long lifetime and ease of care are the main requirements for a portable mass spectrometer ion source. The operating pressure (up to 10^{-3} Torr) in the vacuum chamber may prevent the use of a thermo ionic filament. A dc glow discharge electron source cell (GDES) with a cold cathode can be used as a low power source of electrons, with reduced out-gassing phenomena compared to a heated filament ion source [1–6].

Dc glow discharges can occur with several shapes, sizes and relative locations of the anode and cathode electrodes: e.g. two simple parallel plane electrodes, a plane anode-cylindrical hollow cathode, a hollow cathode with holes, a hollow anode [7], etc. Hollow anodes have been employed in mass spectrometers as an electron source [8]. Glow discharge electron impact (GDEI) with parallel plane electrodes was first proposed by Handberg in a PhD thesis [9] and then by Gao *et al* in a 2007 paper [10]. It was used as an electron source for loading electrons into 2D or 3D ion traps where the sample is introduced and ionized (internal ionization mode) by electron impact. GDEI has been coupled to cylindrical ion trap (CIT) and rectilinear ion trap mass analysers [11, 12]. GDEI/CIT coupling has also been employed in a field-portable mass spectrometer system, ChemSense 600 from Icx Technologies [13–15].

Confidential

 © 2015 IOP Publishing Ltd Printed in the UK

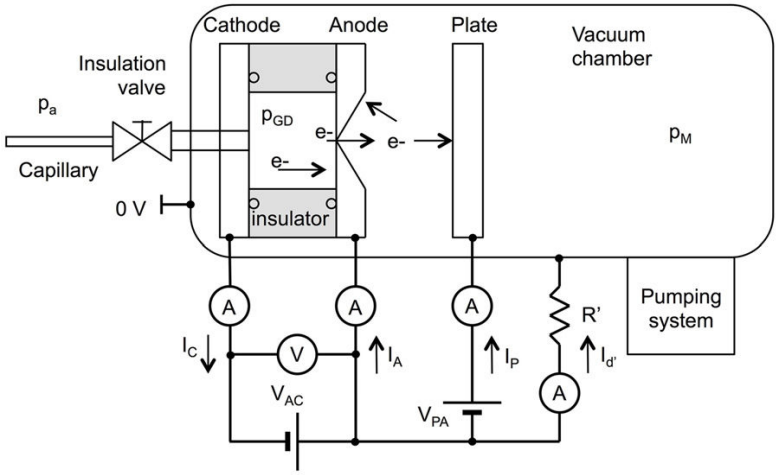

Figure 1. Experimental set-up for testing GDES cell.

In this work, a dc glow discharge cell with planar electrodes as the electron source, similar to those proposed by Gao *et al* [10], is tested with an inlet flow from atmospheric air and using different materials and diameters of the cylindrical ring insulator. The current intensity and kinetic energy distribution of emitted electrons at the anode orifice are estimated for a further use to ionize molecules. These parameters are of interest as they influence both the quantity of the created ions and the fragmentation pattern of molecules.

2. Description and modelling of the device

2.1. Device description

The GDES is placed in a vacuum chamber (figure 1). The cell consists of a parallel planar stainless steel cathode and anode separated and fixed by a ring insulator. The inner diameters of the cylindrical ring insulator used are $\phi_r = 10$, 15 and 20 mm. The distance between the anode and cathode is $d_{ac} = 6.6$ mm. Four insulator materials are tested: Macor, Nylon, Teflon and Pyrex. Two Viton® O-ring seals are used to maintain a higher pressure in the GDES cell than in the vacuum chamber.

2.2. Fluidic system

The gas inlet flow from the ambient room passes through a capillary and enters the GDES cell by a centred cathode aperture. The gas effuses from a centred hole (0.3 mm in diameter) in the anode towards the vacuum chamber. A combination of dry-scroll and turbomolecular pumps ($250\,l\,s^{-1}$) is used to evacuate the gas from the vacuum chamber.

The throughput of the capillary Q_1 can be estimated from the Hagen–Poiseuille equation by [16, 17]:

$$Q_1 = C_1(p_a - p_{GD}) = \frac{\pi\phi_1^4}{128\eta l_1}\frac{p_a + p_{GD}}{2}(p_a - p_{GD}), \quad (1)$$

where C_1 is the conductance of the capillary; $\eta = 1.85 \times 10^{-5}$; Pa × s is the air dynamic viscosity at 25 °C; $\phi_1 = 0.063$ mm is the internal diameter; l_1 is the length of the capillary; p_{GD} is the pressure in the GDES cell; and p_a is the atmospheric pressure.

The pressure inside the GDES cell is low enough to have a molecular flow at the anode orifice, considered as a thin plate orifice. The conductance of the anode orifice C_A is then expressed by [18, 19]:

$$C_A = \frac{\bar{v}}{4}\frac{\pi\phi_A^2}{4}, \quad (2)$$

where $\phi_A = 0.3$ mm is the diameter of the anode orifice and $\bar{v} = 463\,m\,s^{-1}$ is the mean velocity of air particles.

The mass flow balance equations at steady state are expressed by:

$$C_1(p_a - p_{GD}) = C_A(p_{GD} - p_M) = S_p p_M, \quad (3)$$

where p_M is the pressure in the vacuum chamber and S_p is the pumping speed. It can be assumed that $p_a \gg p_{GD} \gg p_M$, as the pressure drops induced by the capillary and anode aperture are important. Hence, the gas throughput balance equation can be written as:

$$C_1 p_a \approx C_A p_{GD}. \quad (4)$$

The pressure inside the GDES cell according to capillary length can then be estimated by:

$$p_{GD}(\text{Torr}) \approx \frac{\phi_1^4 p_a^2}{16\eta\bar{v}\phi_A^2 l_1} \approx \frac{0.098}{l_1}. \quad (5)$$

The pressure varies in inverse proportion to the capillary length. Capillary lengths are chosen to operate the discharge in the vicinity of Paschen's minimum, located at 1 Torr × cm for enclosed air [1].

2.3. Electric system

The dc potential V_{ac} applied between the anode and cathode sustains the discharge (figure 1). The power supply operates

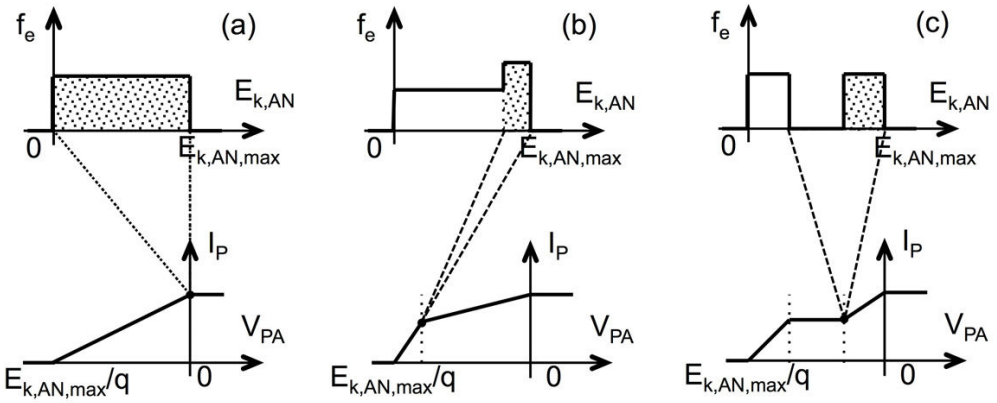

Figure 2. Top: electron kinetic energy distribution and (bottom) plate current obtained versus potential applied between the plate and anode for (*a*) a uniform distribution, (*b*) two adjacent uniform distributions with more electrons at higher energies and (*c*) two separate uniform distributions.

as a voltage source with active current limiting capability. The discharge current (between the anode and cathode) is denoted as I_d. The resistor R' limits the current of undesired discharges between the cathode and the walls of the vacuum chamber, if any.

Some electrons created by the discharge pass through the anode aperture. The electron beam current I_P is measured by means of a collection plate located in front of the anode aperture 2 cm away. Initially it is assumed that the only source of electrons (without creation of secondary electrons) between the anode and plate is the electrons exiting the anode orifice. This electron current is denoted as I_b. A part of these electrons reaches the plate inducing the current $I_{b,P}$, while the other part goes back towards the (not insulated) external side of the anode inducing the current $I_{b,A}$, such that $I_b = I_{b,A} + I_{b,P}$ is constant. The values of $I_{b,P}$ and $I_{b,A}$ depend on the potential applied between the plate and anode, and on the kinetic energy of the electrons at the anode orifice. The cathode current is the total current. The balance equations of the currents in the system are given by:

$$\begin{aligned} I_C &= I_d + I'_d \\ I_A &= I_d + I_{b,A}(V_{PA}) - I_{b,P}(V_{PA}) \\ I_P &= I_{b,P}(V_{PA}) - I_{b,A}(V_{PA}). \end{aligned} \tag{6}$$

2.4. Principle of determination of electron kinetic energy

If the sole source of electrons is the anode orifice, the estimation of the available electron current intensity at the anode aperture and the distribution of the kinetic energy of electrons can be deduced from the measure of the plate current versus potential applied between the plate and anode. The distribution of kinetic energies for electrons at the anode aperture is denoted as $f_e(E_{k,AN})$. The measured current I_P is in proportion to the integral value of the kinetic energy distribution for values of $E_{k,AN}$ ranging between qV_{PA} and $E_{k,AN,max}$:

$$I_P(V_{PA}) \propto \int_{qV_{PA}}^{E_{k,P,max}} f_e(E_{k,AN})\,dE_{k,AN}, \tag{7}$$

where $q = -1$ is the charge of the electron so that qV_{PA} has the dimension of energy in eV and $E_{k,AN,max}$ is the maximum value of the kinetic energy distribution.

If it is assumed that the distribution $f_e(E_{k,AN})$ is uniform, and the plate current is zero for lower negative values of V_{PA}, then it increases linearly from $V_{PA} = E_{k,AN,max}/q$ up to 0 V. For the positive values of V_{PA}, I_P is constant (see curve (a) of figure 2). Two adjacent uniform distributions with more electrons at low or high energies give a dual-slope increase (see curve (b) of figure 2). Two separated uniform distributions lead to a plateau between two linear increases (curve (c) of figure 2).

3. Experimental results and discussion

3.1. GDES cell preparation

The formation of a deposit at the anode has been observed even when operating the GDES cell over several hours in typical conditions for a future use when coupled with a mass spectrometer. This deposit has been measured as electrically resistive. The examination of the anode deposit by scanning electron microscopy combined with energy dispersive x-ray spectroscopy has given the elementary compounds Fe, Cr and Ni, sputtered from a stainless steel cathode, in addition to (1) Fluor (45%), from Teflon and O (8%), from air, when using the Teflon insulator, or (2) O (20%), from Nylon and air when using the Nylon insulator.

For this reason, the anode and cathode are cleaned with a little dilute hydrochloric acid. Then all the parts of the GDES cell are cleaned with ethanol and rinsed with acetone. Finally they are dried at 100 °C over 4 h at atmospheric pressure prior to assembly.

3.2. Paschen curve

The breakdown occurs when the voltage across the electrodes suddenly drops, followed by an increase in the discharge current. The experimental Paschen curve is obtained by plotting the breakdown voltage V_b versus pressure–distance product $p_{GD} \times d_{ac}$ for different values of the pressure in the

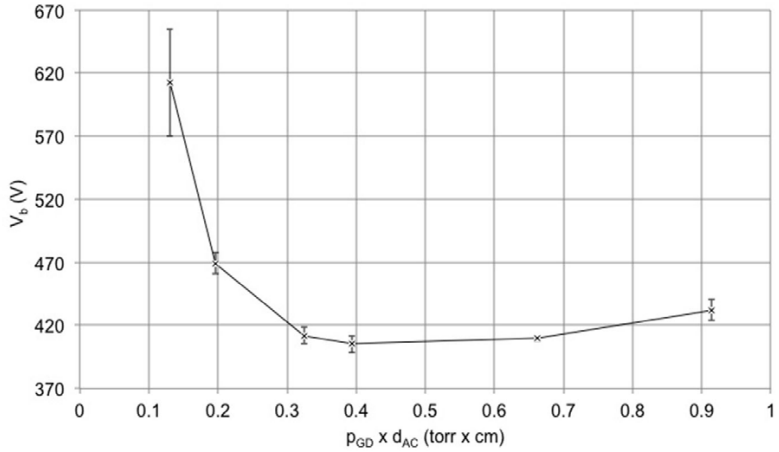

Figure 3. Paschen curve for a Nylon insulator of 10 mm diameter with ambient air flow inlet. From left to right, the capillary lengths are: 50, 33, 20, 16.5, 9.8 and 7.1 cm. The pressure values are calculated from equation (4). The error bar is ±3 standard deviations around the mean value calculated from 10 measured values.

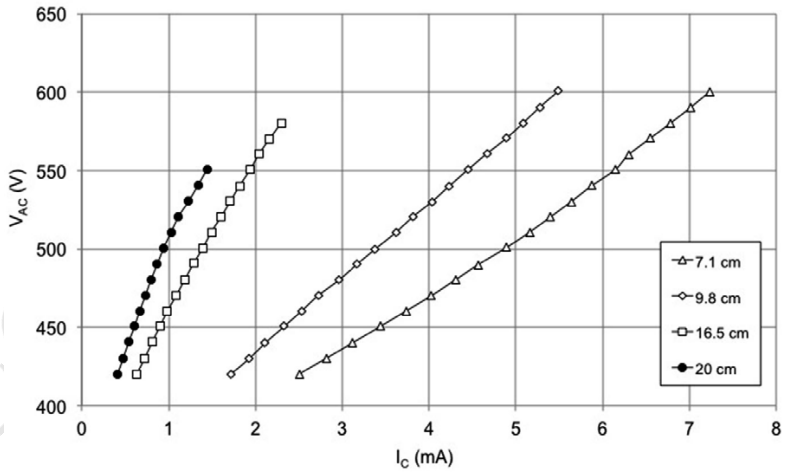

Figure 4. Voltage/current characteristic for a Nylon insulator 10 mm in diameter with ambient air flow inlet. From left to right, the capillary lengths are: (bullet) 20, (square) 16.5, (diamond) 9.8 and (triangle) 7.1 cm.

GDES by means of six capillary lengths: $l_1 = 50, 33, 20, 16.5,$ 9.8 and 7.1 cm (figure 3). Each point of the curve is the mean value of 10 successive measurements. And the error bar is ±3 standard deviations. The other insulator materials and inner diameters lead to similar breakdown voltage values.

In order to have the lowest voltage values, we chose to operate at the Paschen minimum, i.e. for capillary length equal to 16.5 cm.

3.3. Voltage/current characteristic

Three main parameters characterize the discharge: voltage, current and pressure [20]. Additional parameters can influence the discharge: an existing gas flow [21], the temperature of the source and the nature of the gas and electrodes. Also wall losses for constricted discharge can change the voltage–current characteristic [22]. The voltage–current characteristic is established to check the regimes of the discharge due to the use of inlet gas flow of air, a multi-compound gas having different discharge characteristics if they are used separately.

After breakdown, one can observe in the glow discharge regime that both the discharge current and discharge potential increase (figure 4). Voltage slightly increases with current for the highest pressures ($l_1 = 7.1$ and 9.8 cm). For the lowest values of the pressure, the potential increases with current as in an abnormal glow discharge regime. Several papers describe this behaviour for a normal glow discharge regime [23, 24]. There are benefits to having greater slopes, as a small variation of the voltage will induce a small variation of the current for stability. The capillary length $l_1 = 16.5$ cm is suitable to attain a stationary current with lower values to reduce electrical consumption.

3.4. Temporal evolution of the discharge current

The evolution of the cathode current is measured over a period of 4–5 h for the three inner diameters and the four insulator

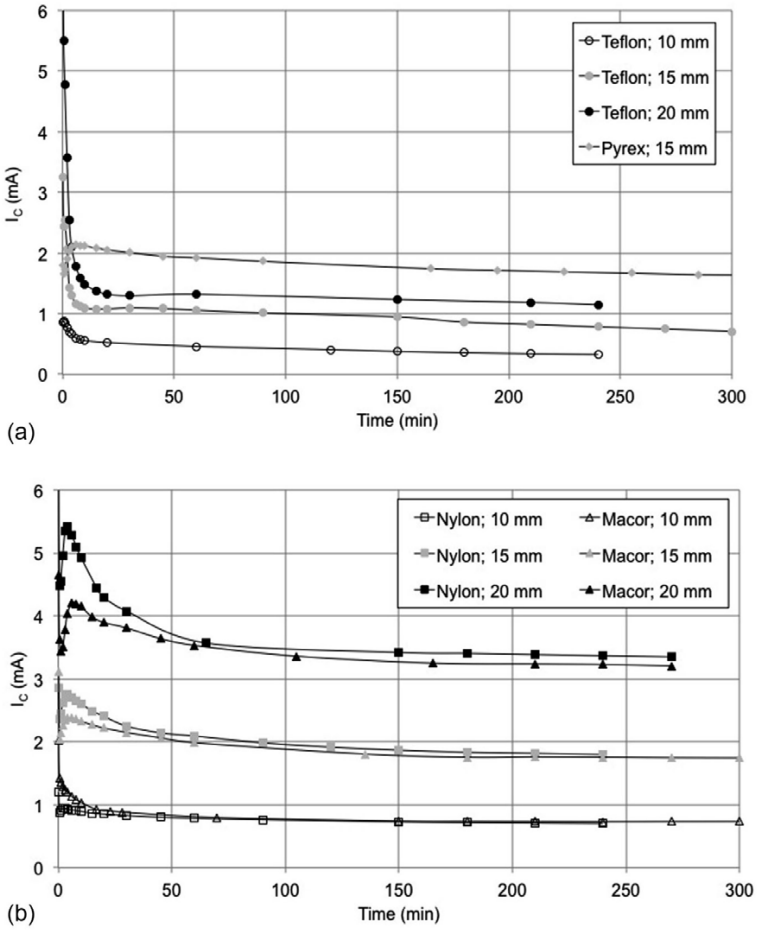

Figure 5. Cathode current versus time for four insulator materials, (triangle) Macor, (square) Nylon, (circle) Teflon and (diamond) Pyrex; and for three inner diameters of the ring insulator, ϕ_r = (white) 10, (grey) 15 and (black) 20 mm. The other operating conditions are: $V_{ac} = 420$ V, $l_1 = 16.5$ cm.

materials (figure 5). The same cathode current value evolutions are observed for the Macor and Nylon for the three diameters. Obviously, with larger diameters, the discharge occupies a larger volume and the cathode current is higher. A steady discharge (cathode) current is obtained after 1–2 h running with the cells in Macor and Nylon.

For the three diameters of Teflon insulator, the cathode current values are lower than those obtained with Nylon and Macor. However, the cathode current always decreases during time and discharge instabilities are observed after a run of about 10 h. Also, for the Pyrex insulator the cathode current never attains a plateau. The best stable glow discharge regime and the lowest power consumption are achieved for a Macor or Nylon insulator 10 mm in diameter.

Previous experimental results have been recorded with the current delivered by the discharge sustaining power supply limited at 10 mA. Here, this current is limited at 0.7 mA, a value just lower than the asymptotic value obtained in figure 5 for a Macor or Nylon insulator 10 mm in diameter. The discharge starts when the power supply is turned on and the discharge current is stationary 2 min after running and remains constant over a long period of several hours.

3.5. Electron kinetic energy distribution

The potential is not linearly distributed inside the GDES cell. Due to the small cathode–anode distance, typically merely the cathode fall, negative glow plasma and anode sheath regions exist [4, 25]. The cold cathode discharge works in the abnormal regime confirmed by the shape of the current voltage characteristics of figure 4. The cathode fall region is close to the cathode with the largest potential difference, while the negative glow plasma region takes up the largest part of the cell with a quasi-constant positive potential. In the cathode fall region, the electrons are violently accelerated by the strong electric field into the plasma where they lose kinetic energy through inelastic collisions with neutrals and ions. The anode sheath region has a short distance where the potential plasma returns to zero, the potential typically applied to the anode. The electrons are repelled in this region. However, the voltage drop in the anode sheath is small, so electrons with enough energy can cross the sheath, losing kinetic energy, and then a part of them passes through the anode aperture, so that in the negative glow plasma there is a complicated electron energy distribution function [26].

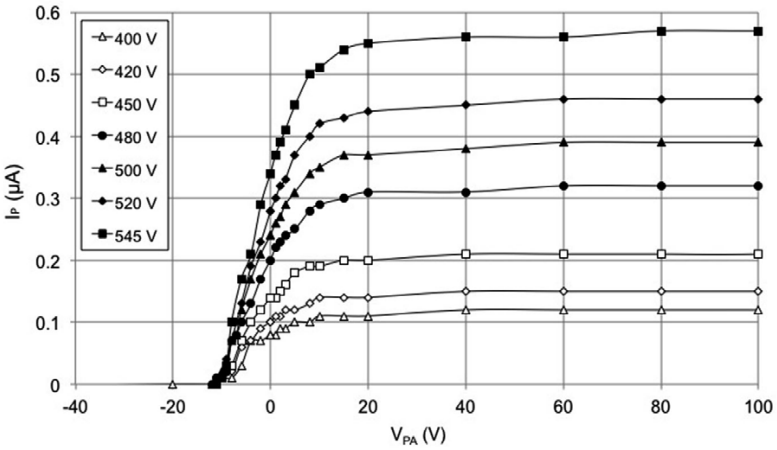

Figure 6. Plate current versus potential applied between the plate and anode for $V_{ac} = 400$ (triangle), 420 (diamond), 450 (square), 480 (bullet), 500 (black triangle), 520 (black diamond) and 535 V (black square). The operating conditions are: nylon ring insulator, $l_1 = 16.5$ cm and $\phi_r = 10$ mm.

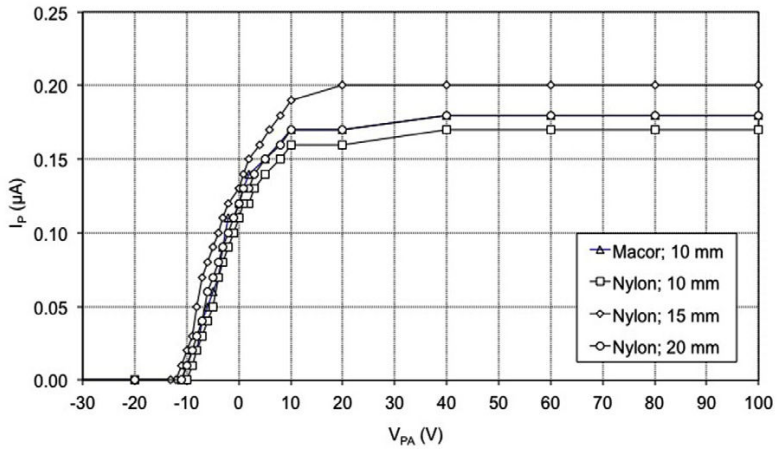

Figure 7. Plate current versus potential applied between the plate and anode for Macor with $\phi_r = 10$ mm (triangle), Nylon with $\phi_r = 10$ mm (square), Nylon with $\phi_r = 15$ mm (diamond) and Nylon with $\phi_r = 20$ mm (circle). The operating conditions are: $V_{ac} = 420$ V, $l_1 = 16.5$ cm and $I_C = 0.7$ mA.

The variation of the plate current versus the potential applied between the plate and anode is plotted in figure 6 for different values of the dc potential V_{ac} applied between the anode and cathode to sustain the discharge. As the shape of the curves shows an increase of the plate current for positive values of the potential applied between the plate and anode, another source of electrons exists between the anode aperture and the plate. That is confirmed by the difference of increase between I_C and I_P measured currents for the same range of V_{ac}. For an increase of V_{ac} from 400 to 545 V, I_C increases by 3.1 times while I_P increases by 4.75 times. Due to gas effusion at the anode aperture, the local pressure is higher enough to take into account an additional source of secondary electrons outside the cell close to the anode aperture, according to the kinetic energy of the primary electrons exiting from the anode aperture.

In figure 6, for the negative values of V_{PA} up to about -10 V, no electron is detected by the plate. The primary electrons have kinetic energies lower than 10 eV and are collected by the outside conductive surface of the anode leading to $I_P = 0$. For positive values of the potential applied between the plate and anode, the plate current continues to grow in order to achieve a plateau from $V_{PA} = 20$–30 V up to 200 V, the maximal measured value (not shown in figure 6). This can be interpreted to mean that no secondary electrons can reach the anode over this potential value, leading us to assume that secondary electron kinetic energy is lower than 20–30 eV.

Moreover, the two insulator materials tested (Macor and Nylon) give the same results (figure 7). A cell with larger inner diameter does not significantly increase the plate current.

3.6. Electron current, power consumption and emission efficiency

The available current of electrons can be increased using higher discharge sustaining voltages (table 1 and figure 6). A positive potential difference between the positive-ion creation zone and anode greater than 20 V must exist when this cell will be used

Table 1. Power consumption and emission efficiency versus discharge sustaining voltage.

V_{ac} (V)	I_C (μA)	P_{ac} (W)	I_P (μA)	I_P/P_{ac} (μA W^{-1})
400	510	0.20	0.12	0.59
420	650	0.27	0.15	0.55
450	877	0.39	0.21	0.53
480	1140	0.55	0.32	0.58
500	1306	0.65	0.39	0.60
520	1478	0.77	0.46	0.60
545	1690	0.92	0.57	0.62

as an electron source coupled to a mass spectrometer with similar geometric and potential configurations. This is because the mean value of the kinetic energy of electrons reaching the plate must be at the optimum of the electron-impact ionization cross-section, typically equal to 70 eV.

As a result, the maximal electron current available can be read from the asymptotic value of the positive voltages in figure 6. A value of about 0.6 μA is attained with $V_{ac} = 545$ V. The power consumption is less than 1 W and the emission efficiency is 0.62 μA W^{-1}.

4. Conclusion

The GDES cell is an interesting source of electrons having low kinetic energies ranging over a few tens of eV. Macor and Nylon are recommended for the cylindrical ring insulator, while Teflon is not, as previously reported in reference [27]. The electron current can attain 0.6 μA at $V_{ac} = 545$ V with an efficiency of 0.6 μA W^{-1}. The stability of the discharge is quickly observed and remains constant over several hours by limiting the power supply current.

The coupling of this electron source with the mass spectrometer requires a specific electrostatic attractive and focusing device for the electrons. In the ion creation zone, the electrons must possess a kinetic energy distribution centred on 70 eV (depending on the targeted molecules), and a range of optimal values for the electron-impact ionization cross-section. With such a narrow range of kinetic energy at the anode aperture, it will then be easy to have all of the electrons available to ionize the molecules with an optimal cross-section value.

Acknowledgments

The research leading to these results has received funding from the European Community's Seventh Framework Programme managed by the Research Executive Agency (FP7/2007–2013) under grant agreement no 285045.

References

[1] Dugdale R A, Maskrey J T, Ford S D, Harmer P R and Lee R E 1969 Glow discharge beam techniques *J. Mater. Sci.* **4** 323–35

[2] Roth J R 1995 Electron sources and beams *Industrial Plasma Engineering: Principles* (Bristol: Institute of Physics Publishing) ch 5

Roth J R 1995 Ion sources and beams *Industrial Plasma Engineering: Principles* (Bristol: Institute of Physics Publishing) ch 6

Roth J R 1995 Dc electrical glow discharges in gases *Industrial Plasma Engineering: Principles* (Bristol: Institute of Physics Publishing) ch 9

[3] Braithwaite N St J 2000 Introduction to gas discharges *Plasma Sources Sci. Technol.* **9** 517–27

[4] Bogaerts A, Neyts E, Gijbels R and van der Mullen J 2002 Gas discharge plasmas and their applications *Spectrochim. Acta* B **57** 609–658

[5] Rocca J J, Meyer J D, Farrell M R and Collins G J 1984 Glow-discharge-created electron beams: Cathode materials, electron gun designs, and technological applications *J. Appl. Phys.* **56** 790–7

[6] Oks E M and Schanin P M 1999 Development of plasma cathode electron guns *Phys. Plasmas* **6** 1649–54

[7] Miljevic V 1984 Hollow anode ion–electron source *Rev. Sci. Instrum.* **55** 931–3

[8] Song K, Cha H, Park H and Chun Lee S 2001 Design and construction of glow discharge-ion trap mass spectrometer (GD-ITMS) and its application for the analysis of volatile organic samples *Microchem. J.* **70** 285–291

[9] Handberg E S 2006 Atmospheric sampling glow discharge ionization (ASGDI) using a quarter-sized cylindrical ion trap mass spectrometer (CIT-MS) for explosives detection in air *PhD Thesis* Purdue University. See chapter 2: Glow discharge electron impact p 35

[10] Gao L, Song Q, Noll R J, Duncan J, Cooks R G and Ouyang Z 2007 Glow discharge electron impact ionization source for miniature mass spectrometers *J. Mass Spectrom.* **42** 675–80

[11] Gao L, Sugiarto A, Harper J D, Duncan J S, Milks R S, Kline-Schoder B, Cooks R G and Ouyang Z 2007 Mini 11 handheld mass spectrometer with glow discharge ion source and atmospheric pressure interface *6th Harsh-Environment Mass Spectrometry Workshop (Cocoa Beach, FL, 17–20 September 2007)*

[12] Gao L, Sugiarto A, Harper J D, Cooks R G and Ouyang Z 2008 Design and characterization of a multisource hand-held tandem mass spectrometer *Anal. Chem.* **80** 7198–205

[13] Wells J M, Fico M, Rardin B and Barket Jr D J 2009 Autonomous light-weight integrated direct sampling mass spectrometer for TIC and CWA detection *7th Workshop on Harsh-Environment Mass Spectrometry (Santa Barbara, CA, 21–24 September 2009)*

[14] Smith J N, Keil A, Likens J, Noll R J and Cooks R G 2010 Facility monitoring of toxic industrial compounds in air using an automated, fieldable, miniature mass spectrometer *Analyst* **135** 994–1003

[15] Smith J N, Noll R J and Cooks R G 2011 Facility monitoring of chemical warfare agent simulants in air using an automated, field-deployable, miniature mass spectrometer *Rapid Commun. Mass Spectrom.* **25** 1437–44

[16] O'Hanlon F J 2004 Gas flow *A User's Guide to Vacuum Technology* 3rd edn (NJ: Wiley) ch 3, pp 25–56

[17] Andres R P 2011 Rational inlet design for a portable atmospheric pressure ionization-mass spectrometer (API-MS) *Int. J. Mass Spectrom.* **300** 194–7

[18] Umrath W 1998 *Fundamentals of Vacuum Technology* (Cologne: LEYBOLD's Vacuum Technology Training Center)

[19] Bomelburg J H 1977 Estimation of gas leak rates through very small orifices and channels *Technical Report (Battelle, Pacific Northwest Laboratories, Richland, Washington)*

[20] Hoffmann V, Efimova V V, Voronov M V, Smid P, Steers E B M and Eckert J 2008 Measurement of voltage

Confidential

and current in continuous and pulsed rf and dc glow discharges *J. Phys.: Conf. Ser.* **133** 012017

[21] Bogaerts A, Okhrimovskyy A and Gijbels R 2002 Calculation of the gas flow and its effect on the plasma characteristics for a modified Grimm-type glow discharge cell *J. Anal. At. Spectrom.* **17** 1076–82

[22] Donkó Z, Bánó G, Szalai L, Kutasi K, Rózsa K, Pinheiro M and Pinhäo N 1999 Investigations on the effect of constriction in the cathode region of argon glow discharges *J. Phys. D: Appl. Phys.* **32** 2416–25

[23] Lisovskiy V and Yakovin S 2000 Experimental study of a low-pressure glow discharge in air in large-diameter discharge tubes: I. Conditions for the normal regime of a glow discharge *Plasma Phys. Rep.* **26** 1066–75

[24] Chiad B T, Al-Zubaydi T L, Khalaf M K and Khudiar A I 2009 Construction and characterisation of a low pressure plasma reactor using dc glow discharge *J. Optoelectron. Biomed. Mater.* **1** 255–62

[25] Delcroix J L 1959 *Introduction à la Théorie des Gaz Ionisés* (*Monographies*) (Paris: Dunod)

[26] Kolobov V I and Tsendin L D 1992 Analytic model of the cathode region of a short glow discharge in light gases *Phys. Rev.* A **46** 7837–52

[27] Pavlik J, Novak S, Kukal J and Macak J 1999 Influence of discharge tube wall materials on plasma parameters *14th Int. Symp. on Plasma Chemistry, Symp. Proc. (Prague, Czech Republic, Institute of Plasma Physics Academy of Sciences of the Czech Republic)* vol I, ed M Hrabovsky *et al* pp 813–18

Confidential

Bibliography

[1] C. L. Rhykerd, D. W. Hannum, D. W. Murray and J. E. Parmeter. Guide for the Selection of Commercial Explosives Detection Systems for Law Enforcement Applications (NIJ Guide 100-99). Technical report, National Institute of Justice (US) (1999)

[2] J. E. Parmeter, D. W. Murray and D. W. Hannum. Guide for the Selection of Drug Detectors for Law Enforcement Applications (NIJ Guide 601-00). Technical report, National Institute of Justice (US) (2000)

[3] N. Barlow. Mars: An Introduction to its Interior, Surface and Atmosphere, (Cambridge University Press, 2008)

[4] L. Rothschild and A. Lister. Evolution on Planet Earth: Impact of the Physical Environment, (Elsevier Science, 2003)

[5] N. R. C. Committee on Assessment of Security Technologies for Transportation. Opportunities to Improve Airport Passenger Screening with Mass Spectrometry, (The National Academies Press, 2004)

[6] R. G. Cooks, Z. Ouyang, Z. Takats and J. M. Wiseman. Ambient Mass Spectrometry. *Science* 311 (2006) 1566–1570

[7] L. Gao, Q. Song, G. E. Patterson, R. G. Cooks and Z. Ouyang. Handheld Rectilinear Ion Trap Mass Spectrometer. *Analytical Chemistry* 78 (2006) 5994–6002

[8] L. Gao, A. Sugiarto, J. D. Harper, R. G. Cooks and Z. Ouyang. Design and Characterization of a Multisource Hand-Held Tandem Mass Spectrometer. *Analytical Chemistry* 80 (2008) 7198–7205

[9] J. Watson and O. Sparkman. Introduction to Mass Spectrometry: Instrumentation, Applications, and Strategies for Data Interpretation, (Wiley, 2013)

[10] M.-Z. Huang, C.-H. Yuan, S.-C. Cheng, Y.-T. Cho and J. Shiea. Ambient Ionization Mass Spectrometry. *Annual Review of Analytical Chemistry* 3 (2010) 43–65

Confidential

[11] H. Chen, J. Zheng, X. Zhang, M. Luo, Z. Wang and X. Qiao. Surface desorption atmospheric pressure chemical ionization mass spectrometry for direct ambient sample analysis without toxic chemical contamination. *J. Mass Spectrom.* 42 (2007) 1045–1056

[12] F. P. M. Jjunju, S. Maher, A. Li, M. J. Lynch, B. Smith, S. U. Syed, R. M. A. Heeren, S. Taylor and R. G. Cooks. Handheld Portable DAPCI Ion Source for in-situ Analysis of Nitroaromatic Explosives. *submitted*

[13] J. P. Williams, V. J. Patel, R. Holland and J. H. Scrivens. The use of recently described ionisation techniques for the rapid analysis of some common drugs and samples of biological origin. *Rapid Communications in Mass Spectrometry* 20 (2006) 1447–1456

[14] L. Gao, R. G. Cooks and Z. Ouyang. Breaking the Pumping Speed Barrier in Mass Spectrometry: Discontinuous Atmospheric Pressure Interface. *Analytical Chemistry* 80 (2008) 4026–4032

[15] Z. Ouyang, R. J. Noll and R. G. Cooks. Handheld Miniature Ion Trap Mass Spectrometers. *Analytical Chemistry* 81 (2009) 2421–2425

[16] B. Brkic, S. Giannoukos, N. France, R. Murcott, F. Siviero and S. Taylor. Optimized DLP linear ion trap for a portable non-scanning mass spectrometer. *International Journal of Mass Spectrometry* 369 (2014) 30–35

[17] B. Brkic, S. Giannoukos, N. France, A. Janulyte, Y. Zerega and S. Taylor. Modeling of an ion source lens system for sensitivity enhancement in a non-scanning linear ion trap. *International Journal of Mass Spectrometry* 353 (2013) 36–41

[18] S. Giannoukos, B. Brkic and S. Taylor. Detection of human chemical signatures in homeland security applications. *IUPAC, Turkey.*

[19] S. Giannoukos, B. Brkic, S. Taylor and N. Frances. Monitoring of Human Chemical Signatures Using Membrane Inlet Mass Spectrometry. *Analytical Chemistry* 86 (2014) 1106–1114

[20] J. J. Thomson. Cathode Rays. *Philosophical Magazine Series 5* 44 (1897) 293–316

[21] J. J. Thomson. Rays of positive electricity and their application to chemical analyses, (Longmans, Green and Co. Ltd., London, 1913)

[22] M. Faraday, M. James and F. James. The Correspondence of Michael Faraday, Volume 1: 1811-1831, (IET, 1991)

[23] W. Brock. William Crookes (1832-1919) and the Commercialization of Science. Science, technology, and culture, 1700-1945, (Ashgate, 2008)

Confidential

[24] F. Paschen. Ueber die zum Funkenübergang in Luft, Wasserstoff und Kohlensäure bei verschiedenen Drucken erforderliche Potentialdifferenz. *Annalen der Physik* 273 (1889) 69–96

[25] J. Townsend. Electricity in gases, (Clarendon Press, Oxford, 1915)

[26] I. Langmuir and H. Jones. Collisions Between Electrons and Gas Molecules. *Phys. Rev.* 31 (1928) 357–404

[27] N. S. J. Braithwaite. Introduction to gas discharges. *Plasma Sources Science and Technology* 9 (2000) 517–527

[28] J. R. Roth. Industrial Plasma Engineering: Principles, chapter 4: Characteristics of plasma, (Institute of Physics Publishing, 1995)

[29] J. R. Roth. Industrial Plasma Engineering: Principles, chapter 9: DC Electrical Glow Discharges in Gases, (Institute of Physics Publishing, 1995)

[30] D. Staack, B. Farouk, A. Gutsol and A. Fridman. Characterization of a dc atmospheric pressure normal glow discharge. *Plasma Sources Science & Technology* 14 (2005) 700–711

[31] A. Howatson. An Introduction to Gas Discharges, (Pergamon Press, 1976)

[32] J.-L. Delcroix and A. Bers. Physique des plasmas, volume 1, (InterEditions / CNRS Editions, 1994)

[33] J.-L. Delcroix and A. Bers. Physique des plasmas, volume 2, (InterEditions / CNRS Editions, 1994)

[34] Y. Raizer, V. Kisin and J. Allen. Gas Discharge Physics, (Springer Berlin Heidelberg, 2011)

[35] A. Bogaerts, E. Neyts, R. Gijbels and J. van der Mullen. Gas discharge plasmas and their applications. *Spectrochimica Acta Part B: Atomic Spectroscopy* 57 (2002) 609–658

[36] B. Chapman. Glow Discharge Processes: Sputtering and Plasma Etching, (Wiley, 1980)

[37] Y. R. Raizer. Gas Discharge Physics, (Springer-Verlag Berlin Heidelberg, 1991)

[38] A. Bogaerts. The glow discharge: an exciting plasma. *Journal of Analytical Atomic Spectrometry* 14 (1999) 1375–1384

[39] R. A. Dugdale, J. T. Maskrey, S. D. Ford, P. R. Harmer and R. E. Lee. Glow discharge beam techniques. *Journal of Materials Science* 4 (1969) 323–335

[40] J. J. Rocca, J. D. Meyer, M. R. Farrell and G. J. Collins. Glow-discharge-created electron beams: Cathode materials, electron gun designs, and technological applications. *Journal of Applied Physics* 56 (1984) 790–797

Confidential

[41] J. R. Roth. Industrial Plasma Engineering: Principles, chapter 5: Electron Sources and Beams, (Institute of Physics Publishing, 1995)

[42] J. R. Roth. Industrial Plasma Engineering: Principles, chapter 6: Ion Sources and Beams, (Institute of Physics Publishing, 1995)

[43] E. M. Oks and P. M. Schanin. Development of plasma cathode electron guns. *Physics of Plasmas* 6 (1999) 1649–1654

[44] S. T. Pai and X. M. Guo. Analytic approach to glow discharge theory: Result and analysis. *Journal of Applied Physics* 71 (1992) 5826–5833

[45] V. Miljevic. Hollow anode ion-electron source. *Review of Scientific Instruments* 55 (1984) 931–933

[46] K. Song, H. Cha, H. Park and S. Chun Lee. Design and construction of glow discharge-ion trap mass spectrometer (GD-ITMS) and its application for the analysis of volatile organic samples. *Microchemical Journal* 70 (2001) 285–291

[47] E. S. Handberg. Atmospheric Sampling Glow Discharge Ionization (ASGDI) Using a Quarter-sized Cylindrical Ion Trap Mass Spectrometer (CIT-MS) for Explosives Detection in Air. Ph.D. thesis, Purdue University (2006)

[48] L. Gao, Q. Song, R. J. Noll, J. Duncan, R. G. Cooks and Z. Ouyang. Glow discharge electron impact ionization source for miniature mass spectrometers. *Journal of Mass Spectrometry* 42 (2007) 675–680

[49] L. Gao, A. Sugiarto, J. Harper, J. S. Duncan, R. S. Milks, B. Kline-Schoder, R. G. Cooks and Z. Ouyang. Mini 11 Handheld Mass Spectrometer with Glow Discharge Ion Source and Atmospheric Pressure Interface, (6th Harsh-Environment Mass Spectrometry Workshop, Cocoa Beach, Florida, 2007)

[50] J. M. Wells, M. Fico, B. Rardin and D. J. J. Barket. Autonomous Light-Weight Integrated Direct Sampling Mass Spectrometer for TIC and CWA Detection, (7th Workshop on Harsh Environment Mass Spectrometry, Santa Barbara, California, 2009)

[51] J. N. Smith, A. Keil, J. Likens, R. J. Noll and R. G. Cooks. Facility monitoring of toxic industrial compounds in air using an automated, fieldable, miniature mass spectrometer. *The Analyst* 135 (2010) 994–1003

[52] J. N. Smith, R. J. Noll and R. G. Cooks. Facility monitoring of chemical warfare agent simulants in air using an automated, field-deployable, miniature mass spectrometer. *Rapid Communications in Mass Spectrometry* 25 (2011) 1437–1444

Confidential

[53] W. Umrath. Fundamental of Vacuum Technology. Technical report, LEYBOLDs Vacuum Technology Training Center, Cologne (1998)

[54] J. F. O'Hanlon. Chapter 3: Gas Flow. In A User's Guide to Vacuum Technology, 25–56, (John Wiley & Sons, Inc., 2004)

[55] R. P. Andres. Rational inlet design for a portable atmospheric pressure ionization-mass spectrometer (API-MS). *International Journal of Mass Spectrometry* 300 (2011) 194–197

[56] H. J. Bomelburg. Estimation of Gas Leak Rates Through Very Small Orifices and Channels. Technical report, BATTELLE, Pacific Northwest Laboratories, Richland, Washington 99352 (1977)

[57] B. T. Chiad, T. L. Al-Zubaydi, M. K. Khalaf and A. I. Khudiar. Construction and characterisation of a low pressure plasma reactor using DC glow discharge. *Journal of Optoelectronics and Biomedical Materials* 1 (2009) 255–262

[58] V. Hoffmann, V. V. Efimova, M. V. Voronov, P. Smid, E. B. M. Steers and P. Ecsmid. Measurement of voltage and current in continuous and pulsed rf and dc glow discharges. *Journal of Physics: Conference Series* 133 (2008) 012.017–1–12

[59] A. Bogaerts, A. Okhrimovskyy and R. Gijbels. Calculation of the gas flow and its effect on the plasma characteristics for a modified Grimm-type glow discharge cell. *Journal of Analytical Atomic Spectrometry* 17 (2002) 1076–1082

[60] Z. Donkó, G. Bánó, L. Szalai, K. Kutasi, K. Rózsa, M. Pinheiro and N. Pinhão. Investigations on the effect of constriction in the cathode region of argon glow discharges. *Journal of Physics D: Applied Physics* 32 (1999) 2416–2425

[61] V. Lisovskiy and S. Yakovin. Experimental study of a low-pressure glow discharge in air in large-diameter discharge tubes: I. conditions for the normal regime of a glow discharge. *Plasma Physics Reports* 26 (2000) 1066–1075

[62] J.-L. Delcroix. Introduction à la théorie des gaz ionisés, volume Monographies, (Dunod, Paris, 1959)

[63] V. I. Kolobov and L. D. Tsendin. Analytic Model of the Cathode Region of A Short Glow-discharge In Light Gases. *Physical Review A* 46 (1992) 7837–7852

[64] J. Pavlik, S. Novak and J. Kukal, J.and Macak. Influence of Discharge Tube Wall Materials on Plasma Parameters. 14th International Symposium on Plasma Chemistry, Symposium Proceedings (1999)

Confidential

[65] H. C. Straub, P. Renault, B. G. Lindsay, K. A. Smith and R. F. Stebbings. Absolute partial cross sections for electron-impact ionization of H2, N2, and O2 from threshold to 1000 eV. *Physical Review A* 54 (1996) 2146–2153

[66] P. L. Bartlett and A. T. Stelbovics. Calculation of electron-impact total-ionization cross sections. *Physical Review A* 66 (2002) 012.707–1–10

[67] F. H. Read and N. J. Bowring. The CPO programs and the BEM for charged particle optics. *Nuclear Instruments and Methods in Physics Research Section A: Accelerators, Spectrometers, Detectors and Associated Equipment* 645 (2011) 273–277

[68] F. H. Read, A. Adams and J. R. Soto-Montiel. Electrostatic cylinder lenses. I. Two element lenses. *Journal of Physics E: Scientific Instruments* 4 (1971) 625–663

[69] B. Brkic, S. Taylor, J. F. Ralph and N. France. High-fidelity simulations of ion trajectories in miniature ion traps using the boundary-element method. *Physical Review A* 73 (2006) 012.326–1–012.326–6

[70] W. Paul and M. Raether. Das elektrische Massenfilter. *Zeitschrift für Physik* 140 (1955) 262–273

[71] P. Dawson. A detailed study of the quadrupole mass filter. *International Journal of Mass Spectrometry and Ion Physics* 14 (1974) 317–337

[72] P. H. Dawson. Quadrupole mass analyzers: Performance, design and some recent applications. *Mass Spectrometry Reviews* 5 (1986) 1–37

[73] J. H. Batey. Quadrupole Gas Analysers. *Vacuum* 37 (1987) 659–668

[74] W. Paul. Electromagnetic traps for charged and neutral particles. *Reviews of Modern Physics* 62 (1990) 531–540

[75] P. H. Dawson. Quadrupole Mass Spectrometry and Its Applications, (American Inst. of Physics, 1997)

[76] R. E. March and J. F. Todd. Quadrupole Ion Trap Mass Spectrometry, (John Wiley & Sons, 2005)

[77] R. E. March. Quadrupole ion traps. *Mass Spectrometry Reviews* 28 (2009) 961–989

[78] D. J. Douglas. Linear quadrupoles in mass spectrometry. *Mass Spectrometry Reviews* 28 (2009) 937–960

[79] J. R. Gibson and S. Taylor. Prediction of quadrupole mass filter performance for hyperbolic and circular cross section electrodes. *Rapid Communications in Mass Spectrometry* 14 (2000) 1669–1673

Confidential

[80] M. Sudakov and D. J. Douglas. Linear quadrupoles with added octopole fields. *Rapid Communications in Mass Spectrometry* 17 (2003) 2290–2294

[81] N. Konenkov, F. Londry, C. Ding and D. Douglas. Linear Quadrupoles with Added Hexapole Fields. *Journal of the American Society for Mass Spectrometry* 17 (2006) 1063–1073

[82] N. V. Konenkov, M. Sudakov and D. J. Douglas. Matrix methods for the calculation of stability diagrams in quadrupole mass spectrometry. *Journal of the American Society for Mass Spectrometry* 13 (2002) 597–613

[83] S. Hiroki, T. Abe and Y. Murakami. Development of a quadrupole mass spectrometer using the second stable zone in Mathieu's stability diagram. *Review of Scientific Instruments* 62 (1991) 2121–2124

[84] S. Hiroki, T. Abe and Y. Murakami. Detection of a 104 helium peak in a deuterium atmosphere using a modified high-resolution quadrupole mass spectrometer. *Review of Scientific Instruments* 65 (1994) 1912–1917

[85] Z. Du, D. J. Douglas and N. Konenkov. Elemental analysis with quadrupole mass filters operated in higher stability regions. *Journal of Analytical Atomic Spectrometry* 14 (1999) 1111–1119

[86] J. Sreekumar, T. J. Hogan, S. Taylor, P. Turner and C. Knott. A Quadrupole Mass Spectrometer for Resolution of Low Mass Isotopes. *Journal of the American Society for Mass Spectrometry* 21 (2010) 1364–1370

[87] S. Syed, T. Hogan, J. Gibson and S. Taylor. Factors Influencing the QMF Resolution for Operation in Stability Zones 1 and 3. *Journal of The American Society for Mass Spectrometry* 23 (2012) 988–995

[88] S. Syed, T. Hogan, M. Antony Joseph, S. Maher and S. Taylor. Quadrupole Mass Filter: Design and Performance for Operation in Stability Zone 3. *Journal of The American Society for Mass Spectrometry* 24 (2013) 1493–1500

[89] P. E. Miller and M. B. Denton. The quadrupole mass filter: Basic operating concepts. *Journal of Chemical Education* 63 (1986) 617–622

[90] J. W. Hager. A new linear ion trap mass spectrometer. *Rapid Communications in Mass Spectrometry* 16 (2002) 512–526

[91] J. C. Schwartz, M. W. Senko and J. E. P. Syka. A two-dimensional quadrupole ion trap mass spectrometer. *Journal of the American Society for Mass Spectrometry* 13 (2002) 659–669

Confidential

[92] M. W. Senko, J. C. Schwartz, A. E. Schoen and J. E. P. Syka. Fourier transform mass spectrometry in a linear quadrupole ion trap. 48th ASMS Conf Mass Spectrom Allied Topics, Long Beach, California. (2000)

[93] C. Senko, Michael (Sunnyvale. Linear quadrupole mass spectrometer (2002)

[94] J. W. Hager and J. C. Yves Le Blanc. Product ion scanning using a Q-q-Qlinear ion trap (Q TRAPTM) mass spectrometer. *Rapid Communications in Mass Spectrometry* 17 (2003) 1056–1064

[95] F. A. Londry and J. W. Hager. Mass selective axial ion ejection from a linear quadrupole ion trap. *Journal of the American Society for Mass Spectrometry* 14 (2003) 1130–1147

[96] H. Qiao, C. Gao, D. Mao, N. Konenkov and D. J. Douglas. Space Charge Effects with Mass Selective Axial Ejection from a Linear Quadrupole Ion Trap. *Rapid Communications in Mass Spectrometry* 25 (2011) 3509–3520

[97] A. Moradian and D. Douglas. Mass Selective Axial Ion Ejection from Linear Quadrupoles with Added Octopole Fields. *Journal of the American Society for Mass Spectrometry* 19 (2008) 270–280

[98] A. Michaud, A. Frank, C. Ding, X. Zhao and D. Douglas. Ion Excitation in a Linear Quadrupole Ion Trap with an Added Octopole Field. *Journal of the American Society for Mass Spectrometry* 16 (2005) 835–849

[99] D. J. Douglas and N. V. Konenkov. Mass selectivity of dipolar resonant excitation in a linear quadrupole ion trap. *Rapid Communications in Mass Spectrometry* 28 (2014) 430–438

[100] D. J. Douglas and N. V. Konenkov. Mass resolution of linear quadrupole ion traps with round rods. *Rapid Communications in Mass Spectrometry* 28 (2014) 2252–2258

[101] P. M. Remes, J. E. Syka, V. V. Kovtoun and J. C. Schwartz. Insight into the Resonance Ejection Process during Mass Analysis through Simulations for Improved Linear Quadrupole Ion Trap Mass Spectrometer Performance. *International Journal of Mass Spectrometry* 370 (2014) 44–57

[102] A. Drakoudis, M. Söllner and G. Werth. Instabilities of ion motion in a linear Paul trap. *International Journal of Mass Spectrometry* 252 (2006) 61–68

[103] D. Tabor, V. Rajagopal, Y.-W. Lin and B. Odom. Suitability of linear quadrupole ion traps for large Coulomb crystals. *Applied Physics B* 107 (2012) 1097–1104

[104] M. Drewsen and A. Brøner. Harmonic linear Paul trap: Stability diagram and effective potentials. *Physical Review A* 62 (2000) 045.401–

Confidential

[105] W. M. Brubaker and J. Tuul. Performance Studies of a Quadrupole Mass Filter. *Review of Scientific Instruments* 35 (1964) 1007–1010

[106] P. H. Dawson. The Acceptance of the Quadrupole Mass Filter. *International Journal of Mass Spectrometry and Ion Physics* 17 (1975) 423–445

[107] P. H. Dawson. Fringing Fields in the Quadrupole Mass Spectrometer. *International Journal of Mass Spectrometry and Ion Physics* 6 (1971) 33–44

[108] W. M. Brubaker. An Improved Quadrupole Mass Analyzer. In E. Kendrick, ed., Advances in Mass Spectrometry, volume 4, (The Institut of Petroleum, London, 1968) 293–299

[109] F. G. Major and H. G. Dehmelt. Exchange-Collision Technique for the rf Spectroscopy of Stored Ions. *Physical Review* 170 (1968) 91–107

[110] G. Stafford Jr., P. Kelley, J. Syka, W. Reynolds and J. Todd. Recent improvements in and analytical applications of advanced ion trap technology. *International Journal of Mass Spectrometry and Ion Processes* 60 (1984) 85–98

[111] J. André, F. Vedel and M. Vedel. Invariance temporelle et propriétés statistiques énergétiques et spatiales d'ions confinés dans une trappe quadrupolaire R.F. *Journal Physique Lettres* 40 (1979) 633–638

[112] J. André, A. Janulyte and Y. Zerega. An historical approach to the effects of elastic collisions in radiofrequency devices and recent developments. *International Journal of Mass Spectrometry* Available online 14 July 2014 (2014) –

[113] A. Chalkha, C. Despenes, A. Janulyte, Y. Zerega, J. Andre, B. Brkic and S. Taylor. A dc glow discharge as a source of electrons for a portable mass spectrometer: characterization of the electron current intensity and electron kinetic energy distribution. *Plasma Sources Science and Technology* 24 (2015) 015.001 (8pp)

Confidential